

(2)

AD-A253 024



DTIC
ELECTED
S JUL 20 1992
S 10

The Application of CFD to Rotary Wing Flow Problems

F. X. Caradonna

March 1992

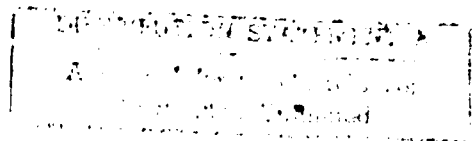


US Army
Aviation Systems Command
Moffett Field, CA 94035-1000



National Aeronautics and
Space Administration

92-18963



87

The Application of CFD to Rotary Wing Flow Problems

F. X. Caradonna, Aeroflightdynamics Directorate, U. S. Army Aviation Systems Command, Ames Research Center, Moffett Field, California

March 1992



US Army
Aviation Systems Command
Moffett Field, CA 94035-1000



National Aeronautics and
Space Administration

Ames Research Center
Moffett Field, California 94035-1000

THE APPLICATION OF CFD TO ROTARY WING FLOW PROBLEMS

F. X. Caradonna

Research Scientist

Aeroflightdynamics Directorate, U.S. Army Aviation Research and Technology Activity
Ames Research Center, Moffett Field, CA

Acceptance For	NTI	SR-61
DTIC Rep		
Unanon. need		
Justification		

Distribution	ability
1st	Special
Avail and	

DTIC QUALITY INSPECTED 2

I. INTRODUCTION

A-1

The performance of rotary-wing aircraft is limited by a host of aerodynamic problems. Foremost among these problems are transonic flow (which is the primary drag source on high-speed propellers and advancing helicopter rotor blades) and stall (on retreating helicopter blades); but there are many other flow problems—especially on helicopters, which operate under a wide variety of conditions and constraints. For example, a helicopter often operates under conditions of flow separation and in its own wake. Because of such flow complexity the aerodynamic design of helicopters is traditionally an empirical craft that often relies more on experience and test than on detailed analysis. This approach requires a high degree of design conservatism. In spite of a cautious design philosophy, rotorcraft development often encounters unexpected and sometimes dangerous aerodynamic problems. Such occurrences will persist as long as we require new designs but lack the ability to predict and control the details of rotorcraft flows.

The ability to design rotorcraft with confidence requires a new order of aerodynamic predictive technology that is both true to the basic flow physics and readily usable by industry. The burgeoning field of computational fluid dynamics (CFD) holds the promise of providing the necessary new tools. In the fixed-wing community, CFD has indeed revolutionized aerodynamics—even to the extent of permitting the freezing of important design features on the basis of computations alone. The rotorcraft community is currently far from this level of confidence, because the basic flow phenomena are more complex, diverse, and interdependent (i.e., many phenomena occur simultaneously and affect each other directly or indirectly through their effects on the flight state).

Some of the basic flow phenomena are illustrated in Fig. 1. The first area of aerodynamic concern on a helicopter is the design of the main rotor, to maximize hover and forward-flight performance and minimize vibratory loads and noise. These are conflicting requirements, which necessitate difficult design compromises. For example, the choice of rotor tip speed is a compromise between minimizing transonic flow effects on the advancing rotor and stall effects on the retreating side. However, this compromise is strongly affected by the choice of airfoils, planform, and twist, and the propulsive requirement. The determination of these features, in turn, depends on the fuselage drag and the rotor flow environment, which is strongly affected by the rotor motion (flapping and elastic deformation) and its wake structure. Therefore, a rotor analysis is a holistic process that involves the blade aerodynamics, dynamics, elastic properties, and fuselage effects. The analysis of various flow features are central to this process.

Rotor CFD applications have not yet reached the level of sophistication that characterizes fixed-wing computations, which include fairly extensive Reynolds-averaged, Navier-Stokes solutions. However, these computations, which must in general be steady because of machine limitations, suffice for most fixed-wing applications. Comparable viscous computations are prohibitively costly for helicopter rotor analyses, because these must usually be unsteady. Furthermore, there exist more immediate (and non-viscous-dominated) computational issues that remain to be solved. These include:

1. ROTOR WAKE PREDICTION. The prediction of the rotor wake structure (its geometry and circulation distribution) is one of the most important rotor flow issues.

For hover, the wake is the single most important flow issue, because it is the primary determinant of induced power. However, the ability of any code to predict this wake with sufficient accuracy is a subject of great debate. Certainly there exists no industry code which can reliably predict the detailed effect of blade geometry (planform, for instance) on the wake. This is because almost all current analyses are boundary-integral codes which represent the rotor as a lifting line and do not treat the 3-D, non-linear compressible blade flow.

For high-speed forward flight, the wake is somewhat less important, because it convects more rapidly away from the blade. However, the wake is still close enough that a detailed knowledge of its nature is required to predict vibratory loading. Also, it is generally conceded that we do not understand the structure of advancing rotor wakes (because of both experimental and computational difficulties) and we cannot reliably predict rotor vibrations. For lower advance ratios and for descent conditions, the rotor and wake closely or directly impinge on one another. No general analysis of this condition, called Blade/Vortex Interaction (BVI), exists.

2. COMPRESSIBLE AERODYNAMICS. At high advance ratios the predominant rotor drag source is due to transonic flow at the tips of the advancing blade. On a high-speed tilt-rotor this transonic flow could conceivably involve the entire rotor. The high drag results from the occurrence of supersonic flow and shocks. That such flows are intrinsically unsteady and strongly three-dimensional demonstrates a weakness of the present use of 2-D measured airfoil data to predict rotor loads and performance.

To date, the most conspicuous strides in rotor CFD have been in the development of methods to solve the compressible flow problem using potential techniques. Although some standardized codes have now been developed, numerous problems remain, including the development of suitable methods to treat the boundary layer and coupling methods to interface these solutions to a global rotor analysis.

3. INTERACTION PROBLEMS. Rotorcraft are unique in the large number of component and flow interactions that occur. The main rotor can interact closely with its own shed wake (a source of noise and vibration), whose location is affected by the fuselage flow field. The fuselage upwash also introduces rotor vibratory forces. In addition, the main rotor and tail rotor can interact in hover to reduce the main rotor efficiency.

Most of the above-mentioned problems do not involve strong viscous forces and can be treated by potential-based methods. Nevertheless, unsteadiness and structural and dynamic

coupling makes the helicopter problem a very large one. Moreover, the helicopter problem does involve very significant viscous complications which require resolution. These include

- 1. RETREATING BLADE DYNAMIC STALL.** Blade flapping and cyclic input (required to satisfy propulsive requirements) drive the retreating blade to very high lift coefficients. Vortex interactions on the retreating side also exacerbate the problem. When stall does occur, it happens after a dynamic delay and is far more violent (inducing very high drags, pitching moments, and flutter) than steady stall is. This defines a hard performance limit. The process is also strongly 3-D, but no method has yet been demonstrated which consistently predicts even 2-D unsteady stall behavior. Development of the necessary viscous flow methods is an important long-term goal. In the interim, however, empirical engineering stall methods will be required and it will be necessary to find ways to include these in our simpler (potential-based) CFD flow analyses.
- 2. FUSELAGE FLOWS.** At high speeds, the largest helicopter power sink is the parasite drag of the fuselage. Indeed, alleviating this drag (and hence the propulsive requirement) is a most potent way of minimizing the retreating blade stall on the rotor. The development of methods to predict the details of the fuselage flow therefore assumes great importance. Helicopter fuselages are often unavoidably bluff and this causes separated flows. To date, our ability to predict the drag of such bodies is limited and requires empirical input. This ability is another long-term flow-prediction goal and one that can benefit from fixed-wing aircraft experience.

Thus a wide variety of near- and long-term rotorcraft flow problems await resolution by CFD methods. There are also many CFD rotor applications in current use. This paper will introduce prospective users or developers to some of these methods and to the issues involved in their use.

This exposition will begin with a description of the various flow equations and the physical approximations they embody. The basic methods of solving these equations will be discussed. This discussion will be aimed at methods that can enter common engineering use, now or in the near future, and therefore, will be mainly confined to the various potential approximations. Many methods have already been developed to treat various aspects of rotor flows, and some of these are in wide use. The discussion of various potential methods will include the means to combine these different analyses to obtain appropriate hybrid codes. A novel approach to obtaining a unified solution (rather than a hybrid) will be discussed in the context of performing hover computations. Methods will also be discussed for coupling CFD analyses to comprehensive codes to obtain trim solutions. Comparisons will be made with data from various flight and special-purpose experiments to demonstrate the efficacy of the varying flow treatments. Finally, some advanced flow topics (including Navier-Stokes solutions) will be outlined, in order to demonstrate the future possibilities as newer CFD methods mature and become practical.

II. FLOW EQUATIONS

The complexity of rotor behavior has required the use of a hierarchy of flow models that are fast and pliable, and enable a comprehension of the entire system. The many limitations of these approximate models have driven the development of CFD for rotor applications. However, even the most elaborate and expensive of the CFD models involve approximations, which break down under limiting, but not unusual, conditions. An awareness of the limits and costs of the flow models is therefore useful. The following is accordingly concerned with those flow models (from most comprehensive to the simplest) on which the new rotor flow methods are based.

NAVIER-STOKES EQUATIONS

Many of the critical phenomena of concern involve dissipative processes (mainly viscous forces). These processes include boundary layers, separation, and vortex formation. There are other flow processes that require viscous dissipation but are effectively described by inviscid models. These processes include shocks and the airfoil Kutta condition. Viscous phenomena are so ubiquitous, however, that the need for a general viscous flow model will always be with us.

The Navier-Stokes equations are considered to be valid for modeling all continuum flow processes. For a perfect gas, these are

mass conservation:

$$\frac{\partial \rho}{\partial t} + \frac{\partial(\rho u_j)}{\partial x_j} = 0 \quad (1)$$

momentum conservation:

$$\frac{\partial(\rho u_i)}{\partial t} + \frac{\partial(\rho u_i u_j)}{\partial x_j} = -\frac{\partial p}{\partial x_i} + \frac{\partial \tau_{ij}}{\partial x_j} \quad (2)$$

energy conservation:

$$\frac{\partial(\rho h)}{\partial t} + \frac{\partial(\rho h u_j)}{\partial x_j} = \frac{\partial p}{\partial t} + u_j \frac{\partial p}{\partial x_j} + \tau_{ij} \frac{\partial u_i}{\partial x_j} - \frac{\partial q_j}{\partial x_j} \quad (3)$$

where ρ is the density, \mathbf{u} the velocity vector, p the pressure, h the specific enthalpy, τ_{ij} the stress tensor, and \mathbf{q} the heat flux vector. The thermodynamic quantities are related by the state equations

$$p = \rho R T \quad (4)$$

and

$$h = C_p T \quad (5)$$

where R is the gas constant and C_p is the specific heat at constant pressure. The only assumptions to this point are that the fluid is a continuum and a perfect gas. (The latter assumption would not hold under condensation or icing conditions.) The heat flux is given by

$$q_i = -k \frac{\partial T}{\partial x_i} \quad (6)$$

where k is the thermal conductivity. The relation between stress and rate of strain is given by

$$\tau_{ij} = \lambda \delta_{ij} \frac{\partial u_m}{\partial x_m} + \mu \left(\frac{\partial u_i}{\partial x_j} + \frac{\partial u_j}{\partial x_i} \right) \quad (7)$$

where δ_{ij} is the Kronecker delta, $\lambda = -2/3\mu$ the bulk viscosity (Stokes hypothesis), and μ the viscosity. This expression is based on the assumption that the fluid is isotropic (stress/rate-of-strain relation is not direction dependent) and Newtonian (stress/rate-of strain relation is linear). Although Eqs. (1-7) are believed to be correct, we cannot solve them without making major simplifications.

Many numerical solutions of the actual time-dependent Navier-Stokes equations have been obtained. However, these are usually only valid for laminar flows. For Reynolds numbers greater than about 1000, flow becomes turbulent and dissipation becomes dominated by mixing (rather than molecular) processes. The numerical resolution of the various characteristic mixing scale lengths requires an extremely dense grid if the above equations are to be used. At the present time such computations require tens to hundreds of hours on the fastest machines (e.g., the CRAY-2), for flows in regions which are too small to be of use to the aircraft engineer. Clearly, the importance of the Navier-Stokes equations is that they are required for the eventual understanding of turbulent processes, and they will motivate the development of supercomputers for many years to come. However, their engineering importance lies far in the future.

In order to derive a unified set of viscous equations with application potential, resort is made to Reynolds averaging. This has the effect of multiplying the number of dissipation terms and introducing new effective viscous and conductive terms that require an assumed mathematical model and defining relations. Most such mathematical models consist of a simple algebraic or mixing-length, effective-viscosity expression. Such models are probably of qualitative interest only for the modeling of separation effects. However, these are currently the most-used viscous models because they are the simplest. For modeling extensive separation, more complex models are required— $\kappa - \epsilon$ models, for instance. However, such viscous models require the addition of two or more convection equations to the total system and reduce the size of the problem that can be modeled with present resources. One frequently used simplification involves the elimination of the streamwise viscous stress terms. The resulting equations are referred to as the thin-layer Navier-Stokes (TNS) equations. The rationale for this simplification is that streamwise viscous stress terms are usually much smaller than the transverse stress terms. Furthermore, memory limitations usually do not permit sufficient grid points to resolve the streamwise viscous stress (for a 3-D problem). Therefore, for problems of real engineering interest, most unified viscous computations use the TNS equations with an algebraic viscous model. Furthermore, most of these computations are performed for steady flows.

EULER EQUATIONS

The above discussion should give some idea of the magnitude of the simplification which results when an inviscid, nonconducting flow model can be used. When a grid can be sized to resolve body geometry rather than viscous scales, the grid reduction can easily exceed a factor of ten. The resulting equations are

mass conservation:

$$\frac{\partial \rho}{\partial t} + \frac{\partial(\rho u_j)}{\partial x_j} = 0 \quad (8)$$

momentum conservation:

$$\frac{\partial(\rho u_i)}{\partial t} + \frac{\partial(\rho u_i u_j)}{\partial x_j} = -\frac{\partial p}{\partial x_i} \quad (9)$$

energy conservation:

$$\frac{\partial(\rho h)}{\partial t} + \frac{\partial(\rho h u_j)}{\partial x_j} = \frac{\partial p}{\partial t} + u_j \frac{\partial p}{\partial x_j} \quad (10)$$

Although the neglect of viscosity is a great simplification, it raises interesting problems for the modeling of those flow features that are apparently inviscid but require some viscosity for initial setup. For instance, an “exact” solution of the Euler equations requires a separate enforcement of the Kutta condition in order to avoid infinite pressures at the trailing edge. However, many difference solutions do not require an explicit Kutta condition specification because of artificial viscosity, which is a natural result of discretization errors. A hypothetical numerical method that had a very low or nonexistent discretization error would require an explicit enforcement of pressure continuity at the trailing edge. This, however, would be a very small price to pay for something which would provide great benefits. The greatest of these benefits would be the ability to convect vorticity without artificial dissipation. This ability is an important issue for rotorcraft, on which the blades often interact with vortices that are fairly old, but have not dissipated. By contrast, current numerical Euler methods dissipate vortices in a very short time (often in several chords of travel).

It is also worth noting that an “exact” inviscid solution, that is, one lacking dissipation, would require an imposition of jump conditions in order to predict flows with shocks. However, a difference solution, with proper numerical dissipation, mimics reality and permits a shock to arise naturally. This is usually referred to as “shock capturing.” It is this ability that was primarily responsible for the rapid growth of CFD in the 1970’s. The presence of artificial viscosity in inviscid methods is thus both a curse and a blessing.

POTENTIAL EQUATIONS

A considerable simplification of the inviscid flow equations is achieved by assuming irrotational flow. That is,

$$\boldsymbol{\omega} = \nabla \times \mathbf{u} = 0 \quad (11)$$

where $\boldsymbol{\omega}$ is the flow vorticity. Any vector field \mathbf{u} that is irrotational can be described as the gradient of a scalar potential field ϕ , or

$$\mathbf{u} = \nabla \phi \quad (12)$$

The subsequent replacement of three velocity components by one scalar potential is a very useful simplification. However, the greatest simplification is a considerable reduction in the number of equations to be solved. Consider Crocco’s equation,

$$T \nabla s + \mathbf{u} \times \boldsymbol{\omega} = \nabla h_0 + \frac{\partial \mathbf{u}}{\partial t} \quad (13)$$

where h_0 is the stagnation enthalpy. (This equation is derived from the second law of thermodynamics and conservation of mass and momentum.) If a flow is isentropic (a statement of energy conservation) and we introduce a velocity potential, Eq. (13) reduces to

$$\frac{\partial \phi}{\partial t} = -h_0 = -(h + \frac{1}{2}u_j u_j) \quad (14)$$

Introducing the isentropic relation

$$p = K p^\gamma \quad (15)$$

we obtain Bernoulli's equation,

$$\rho/\rho_\infty = \left\{ 1 - \frac{\gamma-1}{a_\infty^2} \left[\phi_t + \frac{1}{2}(\nabla\phi)^2 \right] \right\}^{\frac{1}{\gamma-1}} \quad (16)$$

which together with the continuity equation,

$$\frac{\partial \rho}{\partial t} + \nabla \cdot \rho \nabla \phi = 0 \quad (17)$$

forms a complete equation system. The greatest simplification of the potential assumption is that it permits the replacement of four differential equations (conservation of momentum and energy) with a single algebraic equation. Therefore, potential methods are a minimum of five times faster than equivalent Euler methods.

Equations (16) and (17) are actually not a complete system for lifting solutions, because the presence of circulation requires a branch cut so that the potential will remain a single valued function. That is, it is necessary to specify a jump in potential, $\Gamma \equiv \Delta\phi \equiv \phi_u - \phi_l$, whose magnitude is the total upstream flow circulation (both bound and free). For a flow with free circulation (vortex and circulation sheets), a Γ surface must coincide with the vortex sheets, which usually commence at trailing edges. An expression for the branch-cut distribution is obtained by enforcing the continuity of pressure along a stream surface shed from the trailing edge. Using Eqs. (16) and (15), we have

$$\Delta p = p_u - p_l = K \Delta \left[\phi_t + \frac{1}{2} \nabla \phi \cdot \nabla \phi \right] = 0$$

where K is a constant, or

$$\Gamma_t + \mathbf{V}_{\text{ave}} \cdot \nabla \Gamma = 0 \quad (18)$$

where $\mathbf{V}_{\text{ave}} = \frac{1}{2}(\mathbf{V}_u + \mathbf{V}_l)$ is the average velocity of the circulation sheet. Equation (18) expresses the Kutta condition and it completes the potential-flow formulation. This Kutta equation is a convection expression for the branch-cut surface. It describes the surface that shed circulation must follow in order that there are no forces in the flow field. Equations (18) and (16) are thus expressions of the conservation of momentum. Although the potential equations do conserve momentum in smooth flows, there is no strictly conservative statement of momentum conservation. The resulting jump relations permit momentum losses through shocks, and constitute a nonphysical drag mechanism in the isentropic potential model. (The

physical shock drag mechanism is a jump in entropy rather than a momentum across a shock.) This physical modeling error is usually small and easily corrected. Because Eqs. (16–18) strictly conserve mass, they are referred to as the “conservative full-potential equations.” With appropriate treatment of shocks and vorticity transport, these equations probably represent the optimum combination of accuracy and efficiency for inviscid transonic flow problems.

There are many other forms of the potential flow equations. Until recently, the more usual form of the potential equation was that obtained by the elimination of ρ from Eqs. (16) and (17). That is,

$$\nabla^2\phi - \frac{1}{a^2} \left[\frac{\partial^2\phi}{\partial t^2} + \frac{\partial}{\partial t}(V^2) + \mathbf{V} \cdot \nabla \left(\frac{V^2}{2} \right) \right] = 0 \quad (19)$$

where $\mathbf{V} = \nabla\phi$, and a is the local speed of sound obtained by Bernoulli’s equation and the isentropic relation $a^2 = K\rho^{\gamma-1}$. Equation (19) is readily solved and forms the basis of several widely used transonic flow codes. Unfortunately, Eq. (19) is a nonconservative equation; for transonic methods using “shock capturing,” it will not conserve mass. This is a problem of mathematical consistency for which there is no simple fix. Furthermore, there is no significant cost savings in using the nonconservative mass equation.

The above potential equations (both the conservative and nonconservative variants) are usually referred to as “full-potential equations” because no terms are neglected in their formulation. However, it is well known that many of the quadratic and higher order terms in Eq. (19) must be very small, especially for flow over slender bodies. But these cannot all be neglected for it is among these terms that the transonic nonlinearity is to be found. If we neglect all the higher-order terms, with the exception of the quadratic terms in the streamwise direction, we obtain the simplest approximate equations capable of predicting transonic flows. These are the transonic small-disturbance equations, of which there are many variants, all having the form

$$A\phi_{tt} + B\phi_{xt} = F_x + \phi_{zz} + C\phi_{yy} + \text{cross- and lower-order derivatives} \quad (20)$$

where the nonlinearity is contained in the streamwise flux F , which has the form $\alpha\phi_x + \beta\phi_x^2$. Equation (20) is not unique, and various modifications and additions have been made to improve its stability and accuracy. This class of equations is often referred to as the “TSD” (transonic small disturbance) equations. An interesting and useful feature of Eq. (20) is that it is in conservation form, which is a fortuitous outcome of the small-disturbance limiting process. The next level of simplification is to eliminate all higher-order terms in Eq. (19), which yields

$$\frac{1}{a_\infty^2} \phi_{tt} = \nabla^2\phi \quad (21)$$

where a_∞ is the undisturbed speed of sound. This is the linear compressible potential equation. A simple Galilean transformation of Eq. (21) yields the Prandtl–Glauert equation. A transformation to a rotating frame does not produce such a simple result. Equation (21) has been used to predict subcritical compressible rotor flows. Of course, this equation is also the basis of many acoustic rotor analyses.

The final simplification is to assume an infinite speed of sound to obtain Laplace’s equation,

$$\nabla^2\phi = 0 \quad (22)$$

which describes incompressible flow. To date, most rotorcraft computational development work has centered on solving Eq. (22). The reason for this preponderance of work is the importance of accurately predicting the wakes of helicopter rotors. Although helicopter rotors operate deep in the compressible flow regime, the evolution of their shed wakes is basically an incompressible problem. Another reason for the importance of the Laplace equation to rotorcraft is that it is solvable by boundary-integral methods and can permit very rapid solutions. This efficiency is vital for problems wherein the wake solution must be iterated with solutions for the blade near-field aerodynamics and motion.

III. SOME IMPLEMENTATIONS OF THE FLOW EQUATIONS

The various numerical methods and codes used to solve the above systems of equations constitute an enormous field that cannot be extensively treated in the scope of this paper. Rather, this paper will be restricted to those methods that are representative of present work or have high potential for engineering application.

As previously mentioned, rotorcraft CFD must follow a different path from its fixed-wing counterpart because of its unique set of problems. The most obvious difference between the two areas is the greater importance of potential flow methods for rotorcraft. One reason for this is the intrinsic importance of unsteady aerodynamics to rotorcraft. (Even in fixed-wing unsteady work, such as flutter prediction, one finds a predominance of potential methods.) Another reason is the intrinsic importance of wake problems to rotorcraft. The viscous problems encountered on rotorcraft are as important as (and more challenging than) those on fixed-wing aircraft. Nevertheless, unlike in the fixed-wing field, the nonviscous-dominated problems of rotorcraft are not yet solved, and these require much of our present effort.

A typical CFD review would be mainly concerned with differential methods of solution (i.e., finite-difference, finite-volume, and finite-element methods for solution of the partial-differential equations). However, the importance of the wake problem to rotorcraft and the difficulty in solving it with difference methods is such that boundary-integral methods must also be considered. Therefore, the present section is divided into a discussion of both differential and integral methods. Differential methods will be discussed in terms of their most common use, the solution of local blade aerodynamics. Integral methods will be discussed in terms of their most common application, the solution of complex configuration and wake aerodynamics.

BOUNDARY-INTTEGRAL METHODS

The prediction of wake behavior is one of the oldest and most important problems in rotor aerodynamics, and in many respects, it remains unsolved. Most rotor wake problems are incompressible. These problems are also inviscid, to the extent that wake regions are confined to thin layers that are convected by the global flow but are otherwise little affected by it, somewhat like a noninteracting boundary layer.

Traditionally, wakes and configurations have been treated by means of boundary-integral methods. The basis of these methods is the ability to superpose the various elemental solutions of the Laplace equation—the source, the doublet, and the vortex. The actual choice

of functions is arbitrary and their distribution is chosen so as to satisfy surface boundary conditions (no flow-through) and the Kutta condition.

In recent years, Morino [1] has generalized the above approaches and derived an integral flow representation that is valid everywhere (including the body interior).

The basis for this approach is the second Green's identity

$$\iiint_{\nu} (\phi \nabla^2 G - G \nabla^2 \phi) d\nu = \iint_S \left(\phi \frac{\partial G}{\partial n} - G \frac{\partial \phi}{\partial n} \right) dS \quad (23)$$

where G is the Green's function, satisfying

$$\nabla^2 G = \delta(\mathbf{x} - \mathbf{x}_*) \quad (24)$$

and is the familiar unit source potential

$$G = -\frac{1}{4\pi r} \quad (25)$$

where $r = |\mathbf{x} - \mathbf{x}_*|$. Green's identity can be written for any point in the flow field (including the body interior) as

$$E(\mathbf{x}_*) \phi(\mathbf{x}_*) = \oint \oint_{S_B} \left(\frac{\partial \phi}{\partial n} G - \phi \frac{\partial G}{\partial n} \right) dS - \iint_{S_W} \Gamma \frac{\partial G}{\partial n} dS \quad (26)$$

where

$$\begin{aligned} E(\mathbf{x}_*) &= 1, \text{ outside } S_B \\ &= \frac{1}{2}, \text{ on } S_B \\ &= 0 \text{ inside } S_B \end{aligned} \quad (27)$$

Note that the body is represented by a source and doublet distribution on its surface, and the wake is represented by a doublet layer. If \mathbf{x}_* is in the field (outside the body), Eq. (27) is an integral representation for ϕ in terms of the values of ϕ and $\partial\phi/\partial n$ on the surface of the body, S_B , and of Γ on the surface of the wake, S_W . If \mathbf{x}_* is on the surface S_B , Eq. (27) is a compatibility condition between the values of ϕ and $\partial\phi/\partial n$ on S_B , and of Γ on S_W . Note that $\partial\phi/\partial n$ on S_B is known from the surface boundary condition, and that Γ on S_W is known from the preceding time history. Therefore, Eq. (27) is an integral equation that may be used to directly evaluate ϕ on S_B .

Once ϕ on the body surface is known, Eq. (27) can be used to calculate ϕ , and hence to calculate the velocity and pressure anywhere in the field. In particular,

$$\mathbf{V} = \nabla_* \phi = \iint_{S_B} \left[\frac{\partial \phi}{\partial n} \nabla_* G - \phi \frac{\partial}{\partial n} (\nabla_* G) \right] dS - \iint \Gamma \frac{\partial}{\partial n} (\nabla_* G) dS \quad (28)$$

This equation permits us to calculate the velocity of the wake points and hence the geometry of the wake at a time t . Note from Eq. (18) that Γ follows these wake points. Also, since the

Kutta condition of pressure continuity implies that the trailing-edge circulation is shed into this wake at every time step, we have conditions that determine this quantity at the upstream edge of the wake.

The above equations are the basis for all boundary-integral methods. A variant of this formulation [2] results from expressing Eq. (27) at the inside and outside surfaces of the body and combining these to obtain

$$4\pi\phi_i = \int \int_{S_B} (\phi_o - \phi_i) \frac{\partial}{\partial n} \left(\frac{1}{r} \right) dS - 2\pi(\phi_o - \phi_i) + \iint_{S_B - P} \frac{1}{r} \left(\frac{\partial\phi_i}{\partial n} - \frac{\partial\phi_o}{\partial n} \right) dS + \iint_{S_W} \Gamma \frac{\partial}{\partial n} \left(\frac{1}{r} \right) dS \quad (29)$$

where $S_B - P$ indicates the exclusion of point P in the first integral. Equation 29 gives the total potential at an interior point i as the sum of perturbation potentials that result from normal doublet distributions of strength, $(\phi_o - \phi_i)$ on S_B and $(\phi_u - \phi_i)$ on S_W , and from a source distribution of strength, $(\partial\phi/\partial n)_o - (\partial\phi/\partial n)_i$ on S_B . In principle, an infinite number of combinations of doublet and source distributions will give the same external flow field, but different internal flow fields. To render a unique combination of singularities, we can specify one of the singularity distributions, or the internal flow. Two obvious choices of internal flows are stagnation and undisturbed flow.

The above formulations are solved by discretizing the body surface and wake into suitably conforming elements (or panels) and expressing the above equations as discrete summations. The resulting system of linear equations constitutes a large, full matrix which is readily solved by direct or iterative methods. These methods are usually referred to as "panel methods." Panel methods vary according to the type of elemental solutions used, the manner of distributing them, and the type of discretization. The most common methods in use are "low order" schemes, in which the singularity distribution is assumed to be constant on each panel. "High order" methods assume a variation of source or doublet strength over each panel. Some schemes entirely ignore thickness effects and represent wings or rotors as singularity planes with no source terms. These methods are referred to as "lifting surface methods." An even greater simplification involves the approximation of this surface as a single streamwise element—that is, by "lifting line methods." The above equations represent solutions in terms of source and doublet distributions. A lattice of line vortices can be shown to be equivalent to an array of constant-strength doublet panels defined on the same vortex lattice. In "vortex lattice methods," velocities are computed using the Biot-Savart law. The majority of rotor/wake analyses are lifting-line and vortex-lattice methods.

Most recent boundary-integral methods have involved the use of panel methods. The greatest impetus for these developments has been the need for modeling complex aircraft (usually fixed-wing) geometries. Perhaps the most widely used panel method codes, called "VSAERO" [3, 4] and "PANAIR" [5, 6], are based on source/doublet representations such as Eq. (29). VSAERO, in particular, has found wide use for rotorcraft component interaction problems, because it models separation effects and free-wake convection. Figure 2 shows typical VSAERO computations of a complex rotorcraft configuration [7]. The free convection of the wing and rotor wakes of a V-22 can be clearly seen. A comparison of PANAIR and

VSAERO for a V-22 in airplane mode is made in Ref. [8]. This latest generation of integral codes has been driven mainly by fixed-wing needs. Rotor hover problems, however, have not been extensively treated by panel methods.

Most panel method codes have been designed for fixed-wing applications and require only a specified wake geometry. However, for low-speed flight, the wake induction becomes increasingly important compared to free-stream convection. For hovering helicopters this wake induction is the dominant flow consideration, especially because the rotor remains close to its own wake. In fact, helicopter wake problems have mainly been treated by vortex lattice methods using a lifting-line representation of the blade.

The hover problem is very sensitive to the accuracy of the wake computation. This places a stringent requirement on the wake panel or element modeling density. In order to reduce the size of the wake grid, various efforts have been made to use higher-order geometry definitions and/or integration of the wake elements. The most current example of this is the curved vortex elements of Bliss [9, 10]. In this work every three wake points on a vortex line are used to define a locally parabolic-shaped element whose induced velocity is described by an analytic expression (Fig. 3). The accuracy of this element is such that far fewer points are required to resolve the wake than if a series of straight-line elements were used.

The physical accuracy of the hover wake model is also a critical item. One physical wake feature that is uniquely important to rotor hover wake modeling is the local self-induced velocity that results from wake curvature. A curved-line vortex segment contains a logarithmic singularity that does not occur in reality because real vortices have non-zero core radii. But the wake settling rates are a function of the core size. Although this is a logarithmic function (i.e., not strong) it is important for hover. It has been shown [11, 12] that the effect of this core size can be accounted for by incorporating an appropriate cutoff distance in the local Biot–Savart integration over the curved element (Fig. 4). Most wake analyses use straight-line vortex elements only. The contribution at any wake collocation point from its two adjacent vortex elements is therefore zero. This corresponds to a cutoff distance of one wake-element interval, and is too large. Such refinements are not required for computations for many advancing rotors or fixed-wings, because the free-stream convection overwhelms these effects.

Although free-wake computations for hovering rotors have been performed for many years, the most reliable computations have tended to be those that use empirical wake-geometry data [13, 14, 15]. These codes are also extremely fast, because they do not require inflow computations on the wake. Such codes can produce good thrust/power polars when a suitable wake data base is available (a good airfoil data base is also required). However, there is a fortuitous element in this approach, since these codes often do not predict the thrust-vs.-collective-pitch curves accurately. The earlier free-wake codes did not predict the wake geometry well and did not give good performance predictions. More recent free-wake codes are now beginning to produce good results, because of better numerical techniques that more accurately model the physics. The code EHPIC [16] is one that is producing good wake and performance predictions. It is a vortex-lattice, lifting-surface code that uses the self-induction model, curved wake elements, and a unique wake-relaxation scheme, which obviates many instabilities.

A recent paper by Felker et al. [17] gives good examples of current free-wake capabilities using the EHPIC code and data from many tested rotors. Figure 5 shows a fairly typical

comparison of measured and computed tip-vortex geometries and lift/power polars for an S-76 rotor. The comparison of tip-vortex axial settling rate shows some differences, but the distance of closest blade/vortex approach is close. Furthermore, the predicted and measured power are within 3% of each other. This example is shown here only because it involves both wake and performance data for a modern rotor. The level of agreement between data and computation is good. Another widely used code is HOVER [18], which also uses a lifting-surface, free-wake analysis. HOVER also employs a local wake curvature treatment.

Vortex-lattice codes are also widely used for forward-flight wake analyses. The Scully vortex-lattice model [19] is incorporated in the CAMRAD comprehensive rotor analysis code [20] and is probably the most widely used of such codes. The model uses a network of streamwise vortices (generated by the bound-circulation, spanwise gradient) and spanwise vortices (generated by the time rate of change of bound circulation). An alternate vortex-lattice model has also been developed that uses the Bliss-curved vortex elements (Fig. 6).

These advancing rotor applications tend to be used with lifting-line blade models. These blade models use measured airfoil data to obtain profile drag and pitching moments. However, this approach precludes the treatment of 3-D, unsteady transonic characteristics. It also requires empirical models for stall. More accurate treatment of the blades requires the use of differential CFD methods.

DIFFERENCE METHODS

The computation of the rotor-blade aerodynamics entails the treatment of various nonlinear effects, the most common of which is transonic flow. The simplest equations for treating transonic flows are the nonlinear potential equations. Because these equations are nonlinear, they cannot be superposed and it is necessary to discretize and solve them directly. We shall discuss this process only for potential methods. However, the basic process has much in common with that for the more complex flow approximations, such as Euler and Reynolds-averaged Navier-Stokes.

The first step for helicopter computations is to transform the equations to a translating and rotating coordinate system fixed to the blade,

$$\mathbf{r}' = \mathbf{U}_\infty t + \boldsymbol{\Omega} t \times \mathbf{r} \quad (30)$$

where $\mathbf{r}' = (x', y', z')$ and $\mathbf{r} = (x, y, z)$ are the inertial and body-fixed coordinates (Fig. 7), and \mathbf{U}_∞ and $\boldsymbol{\Omega}$ are the translational and angular velocities of the rotor. Under this transformation, the conservative potential equations, Eqs. (16) and (17), become

$$\rho_t + \nabla \cdot [\rho \mathbf{V}] = 0 \quad (31)$$

and

$$\rho/\rho_\infty = \left\{ 1 - \frac{\gamma-1}{a_\infty^2} \left[\phi_t + \frac{1}{2}(V^2 - V_\infty^2) \right] \right\}^{\frac{1}{\gamma-1}} \quad (32)$$

where

$$\mathbf{V} = \mathbf{V}_\infty + \nabla \phi \quad (33)$$

is the local velocity in the blade-fixed frame and $\mathbf{V}_\infty = \mathbf{U}_\infty + \boldsymbol{\Omega} \times \mathbf{r}$ is the local free-stream velocity seen by an observer in the rotating frame. Of course ϕ , being scalar, is unchanged by the coordinate transformation. But in the blade-fixed frame (Eq. (33)) it appears as a perturbation about the free-stream velocity, \mathbf{V}_∞ . Note that, since \mathbf{V}_∞ is rotational, we cannot combine it into (or define) a “full potential” in the normal fixed-wing sense.

Equations (16) and (17) are commonly written for a generalized, moving coordinate system ξ, η, ζ, t (fig. 8) as

$$\partial_t(\rho/J) + \partial_\xi(\rho U/J) + \partial_\eta(\rho V/J) + \partial_\zeta(\rho W/J) = 0 \quad (34)$$

where U , V , and W are contravariant velocity components, and J is the Jacobian of the coordinate transformation. Bernoulli’s equation is similarly expressed in general coordinates:

$$\rho/\rho_\infty = \left\{ 1 - \frac{\gamma - 1}{a_\infty^2} [\phi_t + (U + \xi_t)\phi_\xi + (V + \eta_t)\phi_\eta + (W + \zeta_t)\phi_\zeta] \right\}^{\frac{1}{\gamma-1}} \quad (35)$$

In this formulation, the blade motion is specified by the coordinate terms ξ_t, η_t, ζ_t . Equations (34) and (35) represent an excellent formulation of the potential problem because they are conservative, compact, and geometrically general.

By contrast, under a rotational and translational transformation, the nonconservative full-potential equation (Eq. (19)) becomes (in Cartesian coordinates for a rotor in pure edgewise motion)

$$\begin{aligned} \phi_{tt} + 2V_x\phi_{xt} + 2V_z\phi_{zt} &= (a^2 - V_x^2)\phi_{xx} + (a^2 - V_z^2)\phi_{zz} + (a^2 - V_y^2)\phi_{yy} \\ &\quad - 2V_xV_y\phi_{xy} - 2V_xV_z\phi_{xz} - 2V_yV_z\phi_{yz} \\ &\quad + (\Omega^2 x - 2\Omega U_\infty \cos \psi)\phi_x + (\Omega^2 z + 2\Omega U_\infty \sin \psi)\phi_z \end{aligned} \quad (36)$$

which cannot be put in conservation form. The small-disturbance equation retains the form shown in Eq. (20) under a rotational transformation.

The first differential CFD methods developed were mainly concerned with the small-disturbance equation and much rotor work is still done with these techniques. This work uses finite difference methods, in which the partial derivatives in the basic equations are directly approximated by differences in order to derive systems of linear equations. Other discretization methods have since been developed, notably finite-volume and finite-element methods. These methods also work well, the finite-element methods being the most recent. The following discussion will focus on the finite-difference approach.

In order to illustrate basic ideas and issues, we will consider a simple problem which is a paradigm for all finite-difference, potential methods. Consider a simple 2-D transonic small-disturbance equation (see Fig. 9)

$$\beta\phi_{xx} + \phi_{yy} = \phi_{xt} \quad (37)$$

in which

$$\beta = (1 - M_\infty^2) - (1 + \gamma)M_\infty^2\phi_x$$

This equation models low-frequency flows that result in large shock hysteresis. To complete this problem we require boundary conditions and the Kutta condition for pressure continuity. The latter is satisfied by convecting the trailing-edge circulation using

$$\Gamma_t + U_\infty \Gamma_x = 0 \quad (38)$$

The body no-flow-through condition is specified on a mean surface ($y = 0$) and therefore takes a transpiration form

$$\phi_{y_u} = U_\infty f'_u(x, t) \quad (39a)$$

on the upper side of the mean surface and

$$\phi_{y_l} = U_\infty f'_l(x, t) \quad (39b)$$

on the lower side of the mean surface, where the body geometry is given by $y = f_u(x)$, $f_l(x)$ for the upper and lower surfaces. Various far-field boundary conditions can be used. For an unsteady problem the best condition to use is a nonreflecting, first-order wave equation which permits no inward propagation from the far-field boundary. However, the specification of nonperturbed flow is very common and simple. Therefore we will specify that at the far-field boundary

$$\phi = U_\infty x \quad (40)$$

In order to solve this system of equations (Eqs. (37–40)) we construct a Cartesian grid and approximate the various partial derivatives by differences. The following difference approximations will now be applied to Eq. (37):

$$\begin{aligned} & \text{1st backward difference in } x, \phi_y \cong \nabla_x \phi \equiv (\phi_i - \phi_{i-1})/Dx \\ & \text{1st forward difference in } x, \phi_x \cong \Delta_y \phi \equiv (\phi_{i-1} - \phi_i)/Dx \\ & \text{2nd backward difference in } x, \phi_{xx} \cong \nabla_x \nabla_x \phi = (\phi_i - 2\phi_{i-1} + \phi_{i-2})/Dx^2 \\ & \text{2nd centered difference in } x, \phi_{xx} \cong \nabla_x \Delta_x \phi = (\phi_{i-1} - 2\phi_i + \phi_{i-1})/Dx^2 \end{aligned} \quad (41)$$

where Dx is a streamwise grid interval. These expressions are easily derived from Taylor series. Modifications of these difference approximations are required for points adjacent to the boundaries. For instance, for points adjacent to the mean airfoil surface the normal second derivatives are expressed as

$$\begin{aligned} \phi_{yy_J} &= (\Delta_y \phi_J - \phi_{y_u})/Dy \\ &= (\phi_{J+1} - \phi_J - Dy U_\infty f'_u(x))/Dy^2 \end{aligned} \quad (42a)$$

on the upper surface, and

$$\phi_{yy_J} = (Dy U_\infty f'_l(x) - \phi_J + \phi_{J-1})/Dy^2 \quad (42b)$$

on the lower surface. The bound and shed circulation of a lifting problem require branch cuts (potential jumps or discontinuities) in the wake. Adjacent to these branch cuts, the normal second derivatives are expressed as

$$\begin{aligned} \phi_{yy_J} &= (\Delta_y \phi_J - \nabla_y \phi_J)/Dy \\ &= (\phi_{J+1} - 2\phi_J + \phi_{J-1} - \Gamma)/Dy^2 \end{aligned} \quad (43a)$$

above the cut, and

$$\phi_{yy_J} = (\phi_{J+1} - 2\phi_J + \phi_{J-1} - \Gamma)/Dy^2 \quad (43b)$$

below the cut. These expressions for differencing across the cut are easily obtained by combining a Taylor expansion for ϕ with the known discontinuities in ϕ and $\partial\phi/\partial n$ (Γ and 0, respectively). The value of Γ_i is found by solving a discretized form of Eq. (38).

An instructive (but inadvisable, for stability reasons) discretized form of Eq. (38) is

$$\frac{\Gamma_i^{n+1} - \Gamma_i^n}{\Delta t} + U_\infty \frac{\Gamma_i^n - \Gamma_{i-1}^n}{\Delta x} = 0 \quad (44)$$

which is solved by a simple downstream marching process,

$$\Gamma_i^{n+1} = (1 - \alpha)\Gamma_i^n + \alpha\Gamma_{i-1}^n \quad (45)$$

where $\alpha = U_\infty \Delta t / \Delta x$. Equation (44) evaluates the spacial differences at the previous time step, n , and Γ^{n+1} is solved as a simple algebraic function of known quantities at the previous time step. Such a scheme is referred to as an “explicit” method. For $\alpha > 1$, it is unstable. Note that for $\alpha = 1$ we have $\Gamma_i^{n+1} = \Gamma_{i-1}^n$. This particular choice of grid amounts to physically convecting individual fluid particles from point to point, which is Lagrangian convection, and numerical dissipation does not occur. In general, however, grids cannot be so chosen and dissipation does occur. Such dissipation is unimportant for problems in which circulation merely convects away from the body, as in this example. However, this is an important matter for recirculant flows such as the hover problems mentioned in the previous section. There, the rotor boundary-integral methods treated the wake by Lagrangian convection. This type of convection is not done with current differential CFD methods (potential, Euler, etc.). An additional feature of potential-flow CFD is that the wake differencing (such as in Eq. (43), which is the universal approach) confines the wake to a grid plane. (We shall later show that this is not necessary.) By contrast, a conventional Euler solver, having no potential jump, convects vorticity freely and naturally; but it still does not solve the dissipation problem.

In our simple problem, we first consider a subsonic flow—that is, $\beta > 0$. A discretization of Eq. (37) that is suitable for subsonic flow is

$$\nabla_x \phi^{n+1} - h [\beta \nabla_x \phi^{n+1} + \nabla_y \Delta_y \phi^{n+1}] = \nabla_x \phi^n \quad (46)$$

where $h = Dt$. Note that the entire array of unknowns [ϕ^{n+1} must be found simultaneously in a large matrix inversion. Such a scheme is called “implicit” and has the advantage of having no linear stability restrictions (unlike the above explicit method). However, the price for this stability is the inversion. The left-hand side is nearly Laplacian, and can be inverted iteratively by various standard methods. Furthermore, since ϕ^{n+1} and ϕ^n are close, the iteration process must be very fast (requiring as little as one iteration for some methods). However, a faster and more usual approach involves an approximate factorization of the left-hand operator into a more easily inverted form. For Eq. (46) such a factorization is

$$(I - \beta h \Delta_x) (\nabla_x - h \nabla_y \Delta_y) \phi^{n+1} = \nabla_x \phi^n + \beta h^2 \Delta_x \nabla_y \Delta_y \phi^n \quad (47)$$

The new right-hand term is the factorization error, which is evaluated explicitly at the previous time step. Equation (47) is very easily solved as a two-step process:

$$(I - \beta h \Delta_x) \phi^* = \nabla_x \phi^n + \beta h^2 \Delta_x \nabla_y \Delta_y \phi^n \quad (48a)$$

$$(\nabla_x - h \nabla_y \Delta_y) \phi^{n+1} = \phi^* \quad (48b)$$

First the upper bidiagonal inversions (Eq. (48a)) are performed on each $y=\text{constant}$ grid line. Then the lower triangular matrix (Eq. (48b)) is solved on each $x=\text{constant}$ grid line. These are very simple and well-behaved processes. This often-used procedure is referred to as “approximate factorization” (AF). Many types of AF are possible, and it can be shown that the well-known ADI (alternating direction implicit) method is a form of AF. For supersonic flows (when $\beta < 0$) the difference equation (Eq. (46)) is unstable, and it becomes necessary to replace the streamwise term by a backward difference, such as $\phi_{xx} \cong \nabla_x \nabla_x \phi$. The first successful transonic potential codes employed a simple switch in the differencing process (based on the sign of β) to treat mixed supersonic–subsonic flows. Almost all subsequent transonic algorithms have employed some related forms of upwind biasing.

This discussion is meant only to expose the main issues and must leave out many important related issues. For instance, the above discussion uses a nonconservative equation for simplicity. However, the basic equations and their difference forms must remain in conservation form in order to properly capture shocks. The construction of good algorithms is a very extensive field, requiring much work on differencing, stability, accuracy (including conservation), inversion methods, boundary conditions and grid generation. A review of these is beyond the scope of this paper. However, this example has exposed some of the salient issues and terminology for these solution methods. With this background, we will now discuss some of the actual codes that have been developed.

Because Eqs. (20) (a TSD equation) and (36) (a nonconservative full-potential equation) have the same general form, they share the same general solution methods. Equation (20) is stably discretized using a “Murman mixed difference scheme” (i.e., the previously mentioned central/backward differences in the subsonic/supersonic flow regions [21]) in the streamwise direction. The counterpart to the Murman scheme for Eq. (36) is the “Jameson rotated method,” in which mixed differences in all directions are used [21]. Equation (20) has been implemented in the finite-difference rotor code (FDR) [22, 23] (which, in spite of the name, is conservative) which uses an ADI solution scheme. A refined version of this code called TSP [24] is the best-developed and most heavily used small-perturbation code for rotors. The nonconservative, full-potential equation (Eq. (36)) has been implemented in several rotor codes. The first such implementation is the steady code ROT22 [25]—a derivative of FLO22, which uses a successive-line over-relaxation (SLOR) inversion scheme. Another steady code for Eq. (36) is TFAR1 [26], which uses an approximate factorization solution method (rather than SLOR). The fully unsteady form of Eq. (36) is implemented in the code TFAR2 [27], a derivative of TFAR1.

The above codes are limited either by small-disturbance or conservation considerations. The implementation of a conservative full-potential method is complicated by the inability to either directly eliminate ρ (which destroys the conservation form) or to stably solve Eqs. (34) and (35) as a two-equation system. The spacial terms in Eq. (34) present no problem, as these are easily treated using central differences (stability being maintained by upstream biasing of

density, with density evaluated at the previous time step or iteration). The real problem is to express the term ρ_t in a form that does not depend on ρ at the new time step, $n + 1$. This can be achieved [28, 29] by expanding ρ^{n+1} as

$$\rho^{n+1} = \rho^n + \frac{\partial \rho}{\partial \phi} \Big|_n (\phi^{n+1} - \phi^n) \quad (49)$$

where $\partial \rho / \partial \phi$ is a differential operator obtained from Bernoulli's equation. When Eq. (49) is substituted into the discretized form of Eq. (34) there results an equation of the form

$$\begin{aligned} \nabla_t \nabla_t \phi^{n+1} + \phi_\xi^n \nabla_\xi \nabla_t \phi^{n+1} \\ + \nabla_\xi (\rho^n \Delta_\xi \phi^{n+1}) + \nabla_\eta (\rho^n \Delta_\eta \phi^{n+1}) + \nabla_\zeta (\phi^n \Delta_\zeta \phi^{n+1}) = C^n \end{aligned} \quad (50)$$

This equation can be considered to be a hybrid of Eqs. (34) and (36). The spacial flux operators correspond to those in the conservative full-potential equation, Eq. (34). However, the time derivatives have the same form as the nonconservative time terms of Eq. (36) do. The resulting conservation error is cancelled by the term C^n , which is a conservation correction term evaluated at time n . This formulation was first implemented in a fixed-wing code called TUNA [29]. A subsequent derivative of this code called FPR [30, 31] is tailored for rotor applications. These codes both use an approximate factorization inversion scheme. A similar rotor implementation called RFS2 [32] uses a strongly implicit procedure for matrix inversion.

All of the above-mentioned rotor codes (ROT22, FDR, TSD, TFAR1, TFAR2, FPR, RFS2) have been used in industry. ROT22 is among the most-used because its simplicity and robustness do not put great demands on the user. This code is probably best used for initial high-speed-configuration comparisons (those based on planform and profile, for instance). However, its shock errors (a result of being nonconservative) and its inability to handle unsteady effects limit its accuracy and load-prediction ability. In the U.S., FPR is probably the most available and highly developed, both from a technical and from a user viewpoint, and it has a sizable user community.

At this point it is useful to demonstrate some of the capabilities of differential CFD methods to predict the local blade flows on helicopter rotors. This will be done by comparison of computed flows with results from experiments that were designed for this purpose.

Surface pressure data from nonlifting rotors validate the basic ability of codes to predict transonic flows, free from the complications of wake effects. These tests are usually performed on advancing rotors in order to avoid the wake buildup that would occur on a nonlifting hover.

Probably the most extensive surface pressure model rotor data base has been acquired by ONERA [33, 34, 35]. This data includes nonlifting and lifting data for two- and three-bladed rotors with a variety of blade profiles and planforms. Figure 10 shows an early nonlifting computation of the pressure variation on two surface-pressure transducers performed with a 2-D small-disturbance code. Subsequent 3-D computations compare equally well with the data. However, the point of discussing an inboard 2-D computation is to show the importance of transonic unsteadiness without any mitigating 3-D influences. This unsteadiness is seen in the asymmetry of the pressure about the $\psi = 90^\circ$ azimuth. Computations for a higher speed case in which the steady and unsteady full-potential codes TFAR1 and TFAR2 [27]

were used are shown in Fig. 11. The inadequacy of steady computations is clearly shown in this comparison.

Figures 12 and 13 show a nonlifting computation and data comparison [36] that is unique in that it employs optical methods rather than the usual pressure instrumentation. Figure 12 shows a series of interferograms which are obtained from holograms produced for a range of rotor/laser-beam orientations. These interferograms can be used to reconstruct nearly the entire pressure field around the rotor. Figure 13 shows these reconstructed pressure fields at 0.08 chords above the rotor and at several radii. Also included in Fig. 13 are a comparison between small-disturbance computations and laser velocimetry results. Although several unexplained differences are seen, the overall comparison is quite good. Such comparisons have demonstrated the ability of CFD methods to predict pressure fields away from the surface of the rotor—an essential for high-speed acoustics.

Nonlifting experimental data have also been used to validate the ability of codes to predict high-speed-profile power and transonic-drag rise. Figure 14 shows a comparison of computed and measured torque for a nonlifting two-bladed rotor with a NACA0012 airfoil. The computation [37] was performed using both the standard FPR code and a variant with a nonisentropic correction. This computation also used a Nash-MacDonald boundary layer model. The torque was obtained by integrating the skin-friction and surface pressures. The transonic drag divergence is well predicted, whereas the purely isentropic computation overpredicts the torque at the highest tip Mach Numbers.

These and many other related validations have demonstrated that potential methods can predict those basic blade flows that are essentially inviscid. This means they can predict nearly all flows except those that involve retreating-blade stall. Much remains to be done on these problems, especially on applying boundary-layer corrections to improve drag- and pitching-moment calculations. Another concern is the manner of combining these near-blade computations with the wake-aerodynamic models to obtain a global rotor-flow analysis.

IV. THE COMPUTATION OF COMPLETE ROTOR FLOWS

The previous section summarized some of the last twenty years of CFD code development related to rotorcraft. There now exists an extensive arsenal of hard-won computational tools with which to attack rotor flow problems. However, rotor behavior involves so many interrelated phenomena that the effectiveness of any one analysis can be difficult to judge. The need for complete analyses is obvious and has been addressed elsewhere in the context of comprehensive code development. These comprehensive codes have used a variety of boundary-integral, analytical, and empirical aerodynamic methods. An important requirement for such methods is that they be fast enough to be an integral part of a total vehicle analysis. The following discussion addresses the capability of CFD for modeling the total rotor aerodynamics, and the methods for at least including CFD in a comprehensive rotor analysis. The first part of this discussion will involve the development of hybrid methods in which various wake and blade elements are assembled to produce a total aerodynamic analysis. An additional section will discuss some methods for a unified CFD analysis of blade-wake flow systems.

HYBRID METHODS

Figure 15 illustrates the basic computational problem for a hovering rotor. The behavior of a hovering rotor is governed by its system of shed vortices and vortex sheets and by the local blade flow. Superimposed on the blade (Fig. 15) is a representation of a typical grid used for computing local rotor flows. The grid extends about 3–10 chordlengths from the blade in all directions. The computation of the flow in this grid differs from that in the simple example in Section III in that many of the shed vortex and sheet elements pass through this grid and come physically close to the blade. These circulatory elements must be inserted into the near-field computation. After this is done, we still have an incomplete problem with this type of blade-oriented grid. Most of the rotor wake lies outside of such a local grid and must be accounted for.

The first treatment of hover problems with CFD methods involved the use of a small-disturbance potential equation. The representation of a system of tip vortices passing through the grid was made by specifying a system of additional constant-strength branch-cut sheets (see Fig. 16) using the same logic which is already required to specify the rotor trailing sheet. The edges of the sheets are chosen to coincide with tip-vortex locations. Note that in Fig. 16 the additional branch cuts are shown to be vertical. Actually the sheet orientation is irrelevant because it is only the edge of a constant-strength cut that represents the vortex. The use of branch cuts to specify shed vortices is especially easy for a Cartesian or “H-type” grid (which all small-disturbance methods use) because the tip vortices are nearly parallel to the grid lines. This approach cannot easily be used to specify an inboard vorticity sheet, however, because it would not usually coincide with a coordinate plane. Fortunately these sheets are weak compared to the tip vortices and can be excluded from the near-blade problem. But these sheets and all the wake elements not contained in the grid induce much of the inflow and need to be treated. In Ref. [38] a small-perturbation near-field computation was coupled to the boundary-integral code HOVER [18]. The coupling involved a modification of the HOVER inflow computation (the Biot–Savart integral) wherein all the wake elements contained in the grid were excised to produce a “partial inflow” which was then applied to the blade surface boundary condition as a “partial angle of attack.” This resulting blade-load distribution provides the wake-circulation distribution required by HOVER. HOVER also used an experimentally measured prescribed wake geometry as an input.

Clearly the main issue in hybrid methods is the manner of communicating the wake data to the CFD grid. For convenience, in future discussions we will refer to the present branch-cut approach as “gamma coupling.” The use of a surface partial inflow is referred to as “alpha coupling.” The above approach used both methods.

Although gamma coupling is simple when a vortex can be aligned with a grid line, it is not easily applied to arbitrary grid/vortex orientations. One possible approach would be to use adaptive grids; but there are simpler ways to treat the problem.

One alternate approach involves modifying the flow equations. We can represent the flow velocity as

$$\mathbf{V} = \mathbf{V}_\infty + \mathbf{Q} + \nabla\phi \quad (51)$$

where \mathbf{V}_∞ is the undisturbed free-stream velocity that results from translation and rotation, and \mathbf{Q} is an induced flow field. In this case \mathbf{Q} is the velocity induced by the additional wake

elements in the grid. Substituting Eq. (51) into the continuity equation (Eq. (1)) using an inertial frame for simplicity, we have

$$\rho_t + \nabla \cdot (\rho \nabla \phi) = -\nabla \cdot \rho \mathbf{Q} \quad (52)$$

It can be seen that the only effect on the mass equation is to add a known forcing function to the right-hand side. Note also that \mathbf{Q} can be a rotational field with no loss of validity of Eq. (52). However, the Bernoulli equation would no longer be valid in these rotational regions. But these regions tend to be thin and their primary importance is their circulation. Pressure or density variations in these regions have no global effect. This velocity decomposition approach was first used by Steinhoff [39, 40]. We will refer to the use of an induced velocity field to specify wake systems as “ \mathbf{Q} coupling.” Two different \mathbf{Q} -coupled hybrid hover analyses will now be described.

\mathbf{Q} coupling has been used to hybridize the FPR and HOVER codes. Because FPR uses a spanwise stacked “O grid,” the branch-cut mode of vortex representation is not feasible. However, the velocity decomposition approach (\mathbf{Q} coupling) has been successfully implemented [31]. In this analysis, the effect of the far wake was analyzed using a partial angle-of-attack approach (alpha coupling). The close tip-vortex elements (those passing through the grid) were approximated by infinite straight vortices, which then defined the \mathbf{Q} field. (Straight vortices are a reasonable approximation and obviate a Biot–Savart computation). Of course \mathbf{Q} coupling also implies its own surface inflow modification because changing the velocity field entails a corresponding change in the no-flow-through condition.

\mathbf{Q} coupling has also been employed by Egolf and Sparks [41] using the nonconservative code ROT22. This hover implementation differs from the previous analyses in that the effect of the total wake is specified on the entire outer computational boundary, which eliminates the need for a partial inflow on the rotor surface. This has the advantage that it obviates any need to modify the inflow prediction program. Another interesting feature of this work is that it employed an adaptive grid, which permitted the shed wake (from the trailing edge to the rear grid boundary) to convect freely. This work also uses a local line vortex representation to define a \mathbf{Q} field.

The above discussion presented a variety of finite-difference rotor computations including an extensive self-induced wake system. The described analyses are really “pre-engineering” pilot methods, intended to demonstrate the feasibility of combining difference methods with our present integral methods; and they require validation data which can provide both wake geometry (for inflow prediction) and high-speed blade surface pressures.

Toward this end, an extensively pressure instrumented model rotor was hover tested [42] by the (then) U.S. Army Aeromechanics Laboratory. Simultaneous measurements of the wake geometry (depicted in Fig. 17) provides the tip-vortex-location information that is needed for computational vortex-modeling studies. This data has been studied using the three previously mentioned hybrid analyses, i.e., the small-perturbation approach which combined gamma and alpha coupling [39], and conservative (FPR [31]) and nonconservative (ROT22 [41]) full-potential schemes using \mathbf{Q} coupling. These methods all assume that the vortex strength is equal to the maximum blade bound circulation. Figure 17 shows a comparison of all three approaches, with the data. Overall, there is a remarkable agreement between the three

approaches. In all three methods the predicted shock location is slightly aft of the measured location. This discrepancy is probably a result of the isentropic flow approximation [38]. The agreement between the conservative and nonconservative predicted shock location is somewhat surprising and can result from any number of computational details. The nonconservative approach almost always produces a weaker shock than its conservative counterpart does. The important point is that the basic soundness of the blade/wake aerodynamic matching process is shown. Accordingly, it appears that we should be able to effectively combine our finite-difference blade computations with existing boundary-integral codes. Such analyses could easily include fuselage-induced upwash effects. Of course, in order for the analysis to be meaningful, the difference portion will have to be able to predict drag.

The high speeds involved in the previous hover example are not operationally realistic, and transonic flow is not a major hover consideration, although it does occur. In forward flight, however, such tip speeds are common and the use of transonic flow models becomes important. In principle, the use of a near-field wake representation (one contained in the grid) combined with a far-field model should permit complete forward-flight analyses. However, the practical difficulties of such a computation are much greater than those for hover. The fact that the wake/blade orientation is time-varying appears to preclude the use of a branch-cut wake representation. Furthermore, the use of velocity decomposition (Q coupling) requires a Biot-Savart integral for every grid point (or for enough grid points that interpolation can be used) and for every time step—a rather expensive proposition with present techniques. Also the straight-vortex model used for hover is probably not a good model for curved vortices in forward flight. For these reasons a full forward-flight, velocity-coupled computation has not yet been performed, although it is obviously possible.

There are also physical reasons to defer the use of a specified complete wake model in the current CFD codes. First, the wake structure of even high-advance-ratio rotors is not well known. At high advance ratios, the wake can be weaker (especially on the advancing side) and farther removed from the blade. Furthermore, the wake-induced inflow can be a small percentage of the total inflow. It thus becomes reasonable to use a simpler wake model for many flight conditions.

At the present time, therefore, forward-flight hybrid computations have been performed only on the basis of partial-angle-of-attack or alpha coupling (see Fig. 18). That is, the wake elements that pass through the computational grid are not modeled by means of their spacial velocity fields. Instead, their inflow is accounted for only in the body boundary condition as a partial angle of attack. This angle of attack is still “partial” because any finite-difference computation includes a circulation sheet emanating from the trailing edge. The portion of the wake that corresponds to the grid branch-cut region must be excised from the Biot-Savart integration in the outer boundary-integral wake model. Failure to perform this modification would result in a double accounting for the shed wake circulation.

In computing these advancing blade/wake flows it is convenient to include all geometric (twist), blade motion (flapping and deformation), and inflow effects in this partial angle of attack. A fixed untwisted grid is commonly used and the partial angle of attack is specified by applying a flow-through (transpiration) boundary condition on the surface. The alternative (for a code with a body-conforming grid) would be to generate a new grid (at each time step) that included the partial angle as an effective twist. On this grid, a no-flow-through boundary

condition would then be used. This approach is much more difficult, however, and does not significantly increase accuracy.

Up to this point we have referred to hybridizing only in relation to different *aerodynamic* models. However, we can only confine our discussion to aerodynamics when we know the boundary conditions, and for an advancing rotor we do not know the blade motion beforehand. Instead, we typically know the primary (lift and propulsive) forces and must then perform an iterative aerodynamic/dynamic/elastic computation to find the control inputs (e.g., cyclic and collective) that produce these forces. This is referred to as the rotor trim problem. The end result of the trim process is a knowledge of the blade motion. A typical trim process will use 2-D airfoil table look-ups to provide the local blade aerodynamics around the entire azimuth. Such a process can require the computation of about 10 rotor revolutions to converge to a solution. This is a fast process with look-up tables, but it is clearly impractical to directly replace the look-up process by CFD solutions at each time step. The convergence of present trim procedures is such that CFD solutions cannot be placed in the trim loop.

A solution to this problem that still uses present tabular methods is to solve the local rotor problem outside of the trim loop. This difference solution is then used as a base about which to find corrections resulting from the trim process. Therefore the lift is computed as

$$C_L(\alpha) = C_{L_{CFD}}(\alpha_{old}) + \underbrace{C_{L_{Table}}(\alpha) - C_{L_{Table}}(\alpha_{old})}_{\text{Trim lift correction}} \quad (53)$$

where α and α_{old} are the angles of attack from the current and previous trim loops, respectively. The solution has converged when $\alpha \rightarrow \alpha_{old}$ and the lift correction vanishes. At this point the finite-difference computed lift is fully consistent with the rotor inflow and motion. This scheme appears at first to be a slight retreat from the goal of obviating table look-ups. However, the tables affect only the convergence rate, not the final answer.

This forward-flight matching process was first performed [43] using a small-disturbance code (FDR) and the comprehensive code CAMRAD. Currently, the same matching is regularly performed using the conservative full-potential code FPR. The matching of the CAMRAD and FPR codes is summarized in Fig. 19. The process is started by obtaining a trimmed nonuniform inflow solution (with a full vortex-lattice-modeled wake) with the lift obtained totally from airfoil tables. This is the normal operation of CAMRAD except that partial angles of attack are also computed. These partial angles provide the necessary boundary conditions to obtain an FPR solution for the lift distribution. The program then alternately computes new modified trim solutions and FPR solutions, until the lift correction vanishes. This is an efficient scheme since it does not do the most time-consuming tasks (influence coefficients and finite-difference computations) in the innermost trim loop. The convergence of this process is very fast. Stiff rectangular rotors frequently give good results in one iteration. Soft rotors with varying planforms have required about three iterations.

An example of such a computation is illustrated in Fig. 20, which shows a comparison with one of the ONERA three-bladed test cases. For this case, the tip rotational Mach number is 0.628 and the advance ratio (ratio of forward speed to rotational speed) is 0.387. The airfoils used were S-130XX (a variant of the NACA five-digit family). This computation was accomplished using the coupled FPR and CAMRAD codes [44]. Overall, the agreement of

the data and the computation is good. However, the computation somewhat overpredicts the upper pressures early in the first quadrant ($0^\circ < \psi < 90^\circ$) and the lower surfaces in the second quadrant. The shock location and strength seem to be well-predicted throughout the computation.

The previous cases involved stiff, articulated model rotors, in which the blade motion (except for rotation) was almost pure flapping with very little elastic torsion or bending. Full-scale rotors tend to be much softer than the above-mentioned model blades, and elastic deformations can be important. The first published computational/experimental data comparison for an actual flight vehicle involved an Aerospatiale SA349. A typical data/computation comparison [45], performed using CAMRAD/FPR, is shown in Fig. 21. Although this comparison of surface pressures is promising, the differences between the computed and measured lift actually constitute a significant load error. The resolutions of these problems will probably require improvements in our structural, wake, and coupling models. Nevertheless, the present coupling has effectively integrated 3-D, unsteady transonic flow analysis into the comprehensive rotor modeling process. These codes constitute a valuable analysis-and-advanced-design tool in the hands of a knowledgeable user.

One of the areas that requires further review is the basic notion of the partial angle-of-attack coupling. The idea of a chordwise constant inflow is only valid if all the wake elements causing that inflow are well-removed from the blade (i.e., by more than a chord). Recent studies of blade/vortex interactions (nearly direct impingement) have shown good correlations with BVI leading-edge pressure data merely by using a chordwise-varying inflow [46]. Other computations show significant differences between the use of a chordwise-varying inflow and a full Q-field representation of the vortex [47]. (See the related BVI discussion in Section V.) Perhaps the most significant element of these studies concerns the effects of unsteadiness. The present angle-of-attack (or chordwise-constant inflow) coupling lumps all unsteady effects (except for Mach-number variation) into a single surface inflow. No differentiation is made between inflow and flap/pitch variation. It is well known that the response to these two types of excitation is not the same. Recent computational correlation studies with in-flight data [48] indicate stronger discrepancies in the unsteady-flow model than previously expected. Of course, such discussions would be moot if we had a unified representation of the rotor/wake system.

UNIFIED FLOW METHODS

The rotor and its wake constitute a tightly knit system, and it is natural to solve it as a single problem. This has been done for years using boundary-integral methods. The need to include compressibility has driven efforts to do the same with differential methods, using a single grid that encompasses both the blade and the wake. This work has excluded conventional potential methods because of an assumed inability to convect the wake freely. Thus potential methods had been relegated to use as local-blade-flow solvers in hybrid analyses, and there have been various attempts to use conventional Euler solvers for unified CFD rotor modeling.

Euler solvers have not been discussed to this point. It suffices for present purposes to mention that many such solvers now exist. Most use the finite-volume approach and an explicit, centered-difference solution scheme, which employs user-specified dissipation terms to

ensure stability [49]. Although these methods require “tuning” of dissipation terms (required for stability), they are the most efficient Euler solvers. Another class of Euler solver uses implicit, upwind-differenced schemes that require no tuning and appear to be less dissipative. Several of these Euler methods have also been used in hybrid computations, in the manner described in the previous section [50].

The first unified blade/wake Euler computation of a hovering rotor was performed by Kroll [51] using a centered explicit solver. This computation modeled the hover experiment of Ref. [42] using an “O-O” grid fixed to a blade and large enough to encompass a considerable portion of the wake. A problem found with this computation was that the wake was dissipated to such an extent that the induced inflow was underpredicted. That dissipation was a problem was shown by performing a grid sensitivity study. With coarse grids the lift distribution was badly overpredicted, especially inboard, indicating an underprediction of inflow. Refining the grid reduced the lift, but not sufficiently to compare well with the experimental data (Fig. 22). A comparison of the computed pressure distributions with the data was very favorable at the tip, however. Similar efforts by Kramer et al. [52], and Chen and McCroskey [53] used an upwinded Euler scheme to make comparisons with the same hover data, with similar results (very good agreement with the outboard data, but a tendency to overpredict the lift inboard). Chen’s results showed only a slight grid-refinement sensitivity. This was probably a result of the far grid (away from the blade) being so stretched (to avoid excessive computing time) that the vortex was still unavoidably dissipated. This vortex dissipation can be seen in Fig. 23, which shows computed vorticity contours at various distances from the trailing edge. With present algorithms, the cost of such Euler computations is very high, and it is prohibitive with a grid which is dense enough to eliminate the dissipation. The use of unified rotor/wake computations thus seems remote, but new developments using potential methods as part of the solver could change this situation.

Steinhoff and Ramachandran [54, 55, 56] have recently re-examined the potential approach and arrived at a new method of specifying the shed circulation such that it becomes free to convect through the grid. The heart of their approach is the use of velocity decomposition (Eq. (51)) which was cited in connection with the earlier discussion of hybrid methods. The central idea of this work is that when a Q field is used to represent a wake, any form of velocity field Q can be used as long as $\nabla \times Q = \omega$, where ω is the vorticity distribution for the wake sheet. This new formulation thus entails spreading the circulation sheet to give it an ω distribution, and then finding an appropriate Q , which defines ω . This Q then defines a forcing function for the mass equation (Eq. (48)). This process has been previously described, but in this work a different form is chosen for Q . Using the Biot–Savart law would allow us to find Q as the velocity *induced* by ω . This is a field that fills all space and is therefore too costly to compute, since each field point would require an integration over the entire sheet. However, Q can also be defined as a velocity normal to the sheet that *defines* ω (see Fig. 24). Such a field is zero everywhere, except where ω is nonzero and therefore is computed at relatively few points. This representation seems unphysical at first, because such normal velocities do not exist in the wake. However, on finding ϕ (from the continuity equation) and adding all velocity components to get the total V , this normal velocity is cancelled by $\nabla\phi$, leaving the expected induced flow throughout the entire field. That this must happen becomes obvious when we recall that the Biot–Savart law is itself derived from the continuity equation (i.e.,

Laplace's equation). From this point of view we could think of this potential solver as a non-linear, Biot-Savart induced-flow solver. Moreover, this is the same solver that is solving for the local flow on the rotor. Subsequently, the symbol \mathbf{Q}^v will be used to denote this normal form of \mathbf{Q} .

To find the required strength of \mathbf{Q}^v we use Gauss's theorem to obtain a relation from the integral of \mathbf{Q}^v along a normal through each point on the sheet, thus

$$\Gamma = \iint \frac{\partial \mathbf{Q}^v}{\partial s} ds dn \quad (54)$$

The circulation, Γ , is known at the upstream edge of the sheet (blade trailing edge) from the lift distribution, which is computed as part of the entire calculation. Since Γ is constant along mean streamlines within the sheet, it can easily be computed on the entire sheet. This Γ distribution provides a scaling factor which gives the magnitude of \mathbf{Q}^v as soon as the width and functional form of \mathbf{Q}^v are determined. This width and functional form can be found by means of a viscous solution or by simply choosing computationally convenient forms. For the hover wake problem, the latter approach suffices. A particularly useful form for \mathbf{Q}^v involves a Clebsch-type [57] representation:

$$\mathbf{Q}^v = \Gamma^c \nabla \lambda \quad (55)$$

where Γ^c is a 3-D field which smoothly goes to the appropriate Γ on the sheet as \mathbf{r} approaches the sheet surface. In this representation, Γ is a local-sheet-strength function (which is actually smeared spacially to facilitate the treatment of highly curved sheet surfaces) and $\nabla \lambda$ is a spacial distribution function. The term λ is any convenient function whose gradient is nonzero within some specified small distance from the sheet. This specified smearing distance is chosen to be on the order of the local grid size.

The major computational work in this method is the solution of the continuity equation for the potential. To solve for ϕ , a finite-volume, conservative, full-potential solver is used that is semi-implicit (i.e., explicit in the radial direction only) and employs an AF scheme in each radial plane. A blade-fixed H grid is used to solve for the potential (see [55] for details). The resulting solution involves iteration between solving the mass equation and convecting the shed circulation. Since this is a Lagrangian convection process there is no possibility of vorticity dissipation. During the computation, a four-step procedure is repeatedly used: (1) the vortex-sheet position is integrated as a set of marker streamlines to follow the flow using interpolated values of V from the fixed grid; (2) \mathbf{Q}^v is computed at grid points near the sheet; (3) a potential ϕ is computed at all grid points by solving the compressible mass conservation equation; and (4) a new velocity V is computed at each grid point after adding \mathbf{Q}^v to the potential gradient and free-stream components of the velocity. At convergence the vortex sheet follows the flow. This procedure has been implemented in a code called HELIX-I.

This new solution procedure has been applied to a number of hovering rotor configurations. Comparisons have been made with experimental measurements of tip-vortex geometry, thrust, and power. In order to compute the latter it was necessary to use a simple integral boundary-layer code for skin friction and an energy-flux integral for induced power. Figure 25 shows the computed wake geometry for a 4-bladed, linearly twisted model rotor [13]. The wake is seen both by the wake marker loci (at a point 25° behind a blade) and the contours of

vorticity that these markers carry through the field. The tip vortices can be clearly seen. The axial and radial convection rates of these vortices are compared with experiment in Figs. 26 and 27 and the agreement is good. The experimental-to-computational comparison of the lift/power polars is shown in Fig. 28. The computations somewhat overpredict the power at higher lift, for reasons that are not yet clear. These are the first performance polars ever predicted by differential CFD methods. Figures 29 and 30 show a similar set of comparisons for a model Boeing 360 rotor, and the comparisons are favorable [58].

This is a new approach to flow computation, which combines the traditional CFD ability to treat supercritical flows with the Lagrangian convection typical of the integral codes. Furthermore, the approach greatly expands the capabilities of potential methods. The approach is extendable to forward flight and should be able to handle any of the previously mentioned advancing-rotor problems, but development work is required. It is significant that this class of methods is the first in which differential CFD is used to produce hover results of engineering interest.

V. ADVANCED ROTOR FLOW TOPICS

The previous section dealt with integrating the local blade analysis with the wake. With the success of this integration in view, we now review some previously excluded flow topics that need to be included in the total rotorcraft model in order to convert CFD into a truly complete analysis.

DYNAMIC STALL AND OTHER SEPARATED FLOWS

Retreating blade dynamic stall is one of the most dangerous rotor flow conditions. It is also one of the oldest aerodynamic problems involving major computational effort.

The oldest line of computational stall modeling used boundary-element analyses to model the unsteady, separated flow on dynamically stalling airfoils [59, 60]. Such codes represent the profile given by a vortex lattice or panel model and permit a circulation sheet to peel from the blade surface, on cue from a boundary-layer analysis. The sheet organizes itself into something similar to a stall vortex, convects downstream, and produces loads that resemble measured values. The main problem is the accurate determination of the stall commencement point and time.

One of the first stall analyses in the modern CFD sense is that of Wu et al. [61, 62]. This approach is a combined integral-differential scheme in which the vorticity diffusion equation is solved by difference methods and is simultaneously coupled to a Biot-Savart integral for the induced velocity field. This approach can be especially efficient because the formulation only requires computation where vorticity is nonzero. Figure 31, which illustrates the result from such a computation, shows the streamlines and vorticity contours for a NACA0012 airfoil undergoing sinusoidal oscillations; $\alpha = 15^\circ + 10 \sin(\omega t)$, where reduced frequency $k = \omega c/2V = 0.15$. These computations clearly show the separation and downstream convection of the classical leading-edge stall vortex. Flow reattachment can be seen also. These events are reflected in the lift and moment plots of fig. 32. Unfortunately, the Biot-Savart integral limits this approach to incompressible flows. This is a serious limitation, even for the low Mach numbers which characterize retreating blade stall (Mach 0.3-0.5).

One of the first purely differential CFD stall analyses was that of Mehta [63], who performed laminar, incompressible computations that produced good qualitative comparisons with stall data (see Fig. 33).

Recently, a more general compressible Reynolds-averaged, Navier-Stokes CFD method has been developed by Sankar et al. [64]. This involves a centered, finite-difference, implicit scheme that treats the viscous terms explicitly. Like all centered schemes, the method uses specified artificial dissipation terms to assure stability (see [65]). Figure 34 from [66] shows a comparison of computed and measured lift and pitching moment for a sinusoidally oscillating, 2-D airfoil (Sikorski SSC-A09). For this case, $M_\infty = 0.2$, $Re = 2.0 \times 10^6$, and $k = \omega c/2V = 0.1$. The angle of attack varies between 0° and 20° . Generally good agreement is obtained for both lift and moment, but there are important differences. The computed stall commences sooner than the measured stall, which begins at the top of the stroke. The earlier computed stall can be seen in both the pitching-moment drop and in the oscillations in the lift. The peak loads are well predicted, especially the maximum nose-down moment. However, this is a deep-stall case (one dominated by a distinct vortex generated at the leading edge), and many methods that generate a leading-edge vortex (including a vortex-lattice method) will reproduce similar peak moments. The problem is to accurately predict the beginning of stall. This becomes especially important for light stalls, in which the well-organized vortex does not occur. Such stalls can generate the greatest negative pitch damping and, hence, stall flutter. All published computational-experimental comparisons (that this writer is aware of) treat only deep stall. A systematic comparison of loads and pitch damping for light stalls would be useful. This could be difficult because of the present state of turbulence modeling. The above computation used a Baldwin-Lomax (BL) algebraic turbulence model that is not intended for strongly separated flows. In [64] a κ - ϵ model was compared to a BL model for deep stall computations, and surprisingly little improvement was found. It seems, then, that the basic impediments to the solution of this problem are physical more than numerical. Even our ability to predict steady stall is not well demonstrated. The examples shown above are a major advance, but this advance is mainly a result of our improving computational capabilities.

Our computational ability to model unsteady stall does enable us to predict some major trends that are not always or entirely governed by the details of turbulence. For example, Figs. 35 and 36 show the computed and experimental lift history for an airfoil (SSC-A09) undergoing a constant rate pitch-up [66]. It can be seen in these cases that the effects of Mach number and pitch rate on stall initiation are well predicted, although the subsequent events are not. It might be useful to seek other effects whose trends can be predicted by present computational methods. For example, it is well known that most stall processes involve large 3-D effects. Furthermore, major claims have recently been made concerning the usefulness of nonrectangular planforms for the alleviation of stall effects on very-high-speed helicopters. An ability to demonstrate this usefulness, both computationally and experimentally, would be of major scientific and engineering importance. To date, only steady computations [67] have been made for such configurations. Figure 37 shows a numerical visualization of the computed flow on a nonrotating, nonrectangular blade using simulated particle trajectories. This TNS computation shows tip-vortex formation, inboard separation regions, and general qualitative agreement with observed flows (oil-flow visualizations).

Steady 3-D TNS computations such as the preceding can also be useful in their own right, especially for illuminating the details of tip-vortex formation. The tip vortex interacts with following rotor blades and is therefore an important element in the prediction of higher-harmonic loads and noise. Furthermore, it has been shown that the vortex formation process can have an important influence on the tip drag [68, 69]. This process has been studied numerically by Srinivasan et al. [70], again using the TNS equations with an algebraic turbulence model. The effects of different types of tip cutoffs on the vortex formation were studied and compared to experiment. Figure 38 shows a numerical flow-visualization comparison of the tip vortex formation for a rounded and a flat wingtip. It can be seen that the sharp edges of the squared tip induce an early lift-off of the tip vortex. Numerically generated patterns of surface particle flows have been compared to actual oil-flow visualizations, as shown in Fig. 39 for a rounded tip. Figure 40 shows a comparison of computed and experimental chordwise pressure distributions near a wingtip. The test data are for a flat tip only, whereas the computational results are for flat, round, and beveled tips. The flat-tip computations have all the qualitative features of the data and become quantitatively correct away from the tip. In spite of the differences seen in the tip pressures, the computational values for lift, drag, and pitching moment are very close to the measured quantities. Clearly, computational tools do exist for studying these effects, but the fine details of these flows can not yet be accurately predicted. This may be due to the well-known turbulence modeling deficiencies. The same problems that are seen in viscous tip computations will probably also occur in efforts to predict fuselage flows. These flows must be simulated to obtain downloads in hover, and drag in forward flight. That these problems are of great importance is illustrated by the major performance improvements that can result from drag-reduction programs. CFD, together with major improvements in our physical flow models, can be an important part of such design improvement work.

BLADE-VORTEX INTERACTIONS

Rotors encounter vortices under a wide variety of circumstances and the resulting interactions are a fundamental source of vibratory loading and noise. The problem that most simply embodies such interactions is that of a vortex convecting past a 2-D airfoil. The idea in solving such a problem is that the techniques developed should be directly transferable to 3-D problems.

Srinivasan et al. [70] have studied the 2-D blade/vortex interaction (BVI) using both small-disturbance and TNS flow models. Using the TNS equations, an attempt was also made to directly convect the vortex as part of the total flow field. This attempt suffered from the expected numerical diffusion. However, successful nondiffusing computations were then made using the Steinhoff velocity decomposition method. Figure 41 shows computed grids (these are adaptive), surface-pressure distributions, and Mach contours for such a computed close BVI. This is a high-Mach-number case in which the vortex passes through the supersonic region and momentarily bifurcates the shock. Favorable comparisons were also made with pressure data from a rotor BVI test. Probably the most innovative CFD treatment of the 2-D BVI problem is that of Rai [71] who developed a high-order, upwind TNS scheme whose dissipation is low enough to permit a full velocity field convection of the vortex. This is also the first method capable of predicting head-on BVIs. Figure 42 shows the grid that was used for these computations. It includes a high-density upstream grid region which minimizes the vortex dissipation prior to the BVI. Figure 43 shows the convection of the vortex before, during, and

after the BVI. The post-BVI vortex has a duplex structure, which has been seen in rotor BVI testing with smoke visualization. Figure 44 shows the corresponding pressure contours. These are especially significant because they reveal the initiation of an acoustic wave generated by the BVI. This method is clearly a valuable tool for the study of basic rotor acoustic signal generation, and has been used in the work of Baeder [72]. Figure 45 shows the generation and early development of a BVI-generated acoustic wave for a supercritical flow. Rai has also made comparisons with the rotor BVI surface-pressure data of [73]. Figures 46 and 47 include a schematic of this experiment and a comparison of the pressure data and computations, which shows good agreement. The computed results shown here agree very closely with the results of Srinivasan et al. [70]. The cost of this upwind scheme probably excludes it from consideration as a practical computation method, but it constitutes a standard against which other methods should be compared.

The first 3-D BVI computations were performed by Caradonna et al. [46], who used the FPR code with a velocity-decomposition model of the vortex flow field. Good agreement was obtained with the BVI pressure data of [74], for both parallel and oblique blade-vortex interaction angles. Figure 48 shows a typical comparison of computed and measured surface pressures for a transonic, oblique BVI. A surprising feature of this work is that good agreement was seen in surface-pressure comparisons even for head-on parallel BVIs. Because the present velocity decomposition requires a specified vortex structure, there is no mechanism allowing for the alteration of this structure. Furthermore, the Bernoulli equation is not valid within the vortex. Even so, good surface pressure agreement was obtained. This indicates the possibility that the detailed momentum equations may not have to be solved strictly within the vortex for some types of vortical interactions—a potentially significant possibility when these methods are combined with the potential, vorticity-convection methods, such as those described in Section IV. Another insight gained from this work involves the relative effectiveness of Q coupling and alpha coupling. Both Q-field and surface-inflow methods of vortex specification were tested. Although the surface inflow comparisons with data showed good agreement, the Q-field method was consistently better. The Q-field method was found to be superior for parallel and oblique interactions, and for subcritical and supercritical flows. The reason for this is probably that a surface-inflow method involves approximating the effect of the vortex as an effective body motion. It is well known from linear theory (for instance, comparing the Theodorsen and Sears functions) that the response of a wing to a plunge and a gust are initially quite different. The above comparison (between Q coupling and alpha coupling) is directly analogous. It appears, therefore, that we will have to find a convenient way to Q-couple our rotor blade computations.

The computational and experimental study of blade/vortex interactions will probably continue for some time, because it is providing insight into important physical problems and is a rich source of directions for computational modeling.

INGREDIENTS FOR PERFORMANCE PREDICTION

In order to reap the benefits of constructing a rotor/wake/fuselage CFD analysis, it is necessary to study the accuracy of drag prediction. With CFD, our first means of drag prediction is to directly integrate the surface-pressure distributions. Drag prediction is a very rigorous test of a numerical method because drag is almost always a small number, involving

cancellations of the forces from different parts of the blade. Conversely, lift is relatively easy to predict. The accurate prediction of drag requires careful attention both to numerical accuracy and to the physics. Numerical accuracy is usually a matter of assuring that the differencing of geometric and flow quantities are consistent with each other [75] and that “good” grids are used. Whereas consistency is something that is supposedly built into a code, grid construction is usually a matter for the user and tends to be an art. There are only a few grid-construction rules: (1) grids should be as orthogonal as possible, (2) rapid changes in grid size should be avoided, and (3) the ratio of cell lengths should be as close as possible to one. Although there are a number of grid generators, few (or none) are right for all situations, and user intervention is the norm. Such intervention is usually required because of geometric or grid-size limitations. The end result is often a less-than-ideal compromise, which can result in very slow convergence or, worse, inaccuracy. An acid test of a solution is its drag accuracy. Therefore it is often necessary to perform nonlifting, subcritical test computations, because these are the only cases for which we know the theoretical drag. Physical accuracy is a matter of having a proper viscous model. For most rotor flows, a noninteracting boundary-layer model is probably adequate. For supercritical flows, the shock entropy rise is a greater and more performance-limiting drag source. This is an important issue for potential methods, which use an isentropic flow model. It has been shown [76-78] that potential methods can be simply corrected to account for this entropy rise. One of the simplest such corrections has been applied to the FPR code by Bridgeman et al. [37]. This consists of applying the nonisentropic density expression

$$\rho = \rho_i e^{-\Delta S/R} \quad (56)$$

where ρ_i is the isentropic density given by Eq. (35) and ΔS is the shock-generated entropy computed by the Rankine–Hugoniot relations. It can be shown that it suffices to use this expression only at shock points. Equation (56) is strictly valid only for steady flows, but it has produced good results for both steady and unsteady solutions. In general, it requires an unusually strong shock (for rotors) for these corrections to be necessary. Such flows often involve shock-induced separation and probably require at least a TNS flow model. Although the use of a strongly interacting boundary layer is also possible these methods tend not to be very robust for strong shocks. Of course, all these analyses encounter the turbulence modeling problem. Our reliance on testing will not soon disappear for flows with strong shocks, but we now have the computational tools and the option to design configurations that avoid such situations.

Figure 14 showed a comparison of the computed and measured torque for a nonlifting rotor. This FPR computation employed a 2-D, noninteracting integral boundary-layer model (Nash–MacDonald). Subsequent computations [79, 80] have also used the 3-D finite-difference boundary-layer code BL3D [81]. For this simple rectangular rotor, drag results are very similar for the two boundary-layer models, the integral method predicting somewhat lower values. However, beyond drag divergence the difference is inconsequential because most of the drag is due to inviscid effects. In order to further test our drag prediction ability, nonlifting comparisons have also been performed for nonrectangular rotors. Figure 49 shows a sketch of the tested rotor and two pressure distributions plotted as functions of chord and profile height (as required for drag integration). It can be seen in Fig. 50 that the computed inviscid, spanwise drag distributions for rectangular and swept planforms are very different. For the

rectangular case the drag is very close to zero except near the tip. Much of this small drag is numerical. However, the inviscid drag for even a nonlifting rotor is nonzero due to acoustic radiation. Figure 51 shows a comparison of computed and measured torque for the swept rotor, using the integral and finite-difference boundary-layer models. It appears that fairly simple boundary-layer corrections will be applicable for a wide range of conditions. The ability to directly integrate surface pressure to obtain drag indicates that we should also be able to find induced drag by similar means. However, this depends on our ability to accurately predict the wake.

VI. CONCLUDING REMARKS

Rotorcraft aerodynamics is especially rich in unsolved problems, and for this reason the need for interdependent computational and experimental studies is great. Rotor CFD is unique in that its developers have frequently been experimentalists as well. This has maintained a needed balance between our ability to compute and our ability to see the whole problem. Considerable progress has been made and we can begin to think of rotor CFD as a viable engineering tool as well as a means for basic studies.

3-D unsteady, nonlinear potential methods are becoming fast enough to enable their use in parametric design studies. At present, combined CAMRAD/FPR analyses for a complete trimmed rotor solution can be performed in about an hour on a CRAY Y-MP (or ten minutes, with multiple processors). These computational speeds indicate that in the near future many of our large CFD problems will no longer require a supercomputer. It is also becoming clear that potential-based methods are more capable than we had previously supposed. The ability to convect circulation is routine for integral methods, but only recently have we discovered how to do the same with differential methods. With the HELIX-I code it is possible to compute an entire hover performance polar (about five full 3-D, supercritical flow computations, including boundary-layer and free-wake) in about six hours. Steady, viscous airfoil computations (for example, with ARC2D) for flows with no major separation can be done in minutes. These could greatly augment our still much-used airfoil data base.

It is clear, then, that the differential CFD rotor analyses are poised to enter the engineering workplace. Integral methods already constitute a mainstay. Although much development is still required, the major need now is for skillful users who can apply these tools to their own individual problems. Ultimately, it is these users who will integrate CFD into the entire engineering process and provide a new measure of confidence in design and analysis.

It should be recognized that the above classes of analyses do not include several major limiting phenomena (especially dynamic stall), which will continue to require empirical treatment because of computational time constraints and our limited physical understanding. Such empirical treatment should be included, however, into our developing CFD, engineering-level analyses. Moreover, it is probable that in the near future CFD will be reliable enough to provide a new source of empirical information with which to supplement physical measurements. We can expect to be able to visualize effects and test ideas in ways that are not possible with physical testing. It is likely that properly constructed flow models containing corrections from physical testing will be able to fill in unavoidable gaps in our experimental data base, both for

basic studies and for specific configuration testing. For these kinds of applications, computational cost is not an issue. For rotorcraft, testing and computation will become increasingly and truly interdependent, and the extent of this integration should be an important measure of their effectiveness.

Finally, we should recognize that although rotorcraft are probably the most complex of aircraft, the rotorcraft engineering community is very small compared to the fixed-wing community. Likewise, rotorcraft CFD resources can never achieve fixed-wing proportions and must be used wisely. Therefore we must glean the fixed-wing work for many of our basic methods. This approach has its limits, though, because rotor needs are unique and cannot be met without much original thinking. This is a fertile field with much yet to accomplish.

REFERENCES

1. L. Morino and K. Tseng, "A General Theory of Unsteady Compressible Potential Flows with Applications to Airplanes and Rotors," to appear in *Developments in Boundary Integral Methods Volume 6: Nonlinear Problems of Fluid Dynamics*, ed. by P.K. Banerjee and L. Morino, Elsevier Applied Science Publishers, Barking, UK.
2. B. Maskew, "Prediction of Subsonic Aerodynamic Characteristics: A Case for Low-Order Panel Methods," *Journal of Aircraft*, Vol. 19, No. 2, pp. 157-163, Feb. 1982.
3. B. Maskew, "Program VSAERO, A Computer Program for Calculating the Nonlinear Aerodynamic Characteristics of Arbitrary Configurations, User's Manual," NASA CR-166476, Nov. 1982.
4. B. Maskew, "VSAERO Theory Document," *NASA CR-4023*, Nov. 1986.
5. F. Johnson, "A General Panel Method for the Analysis and Design of Arbitrary Configurations in Incompressible Flow," *NASA CR-3079*.
6. K. Sidwell, P. Baruah, and J. Bussoletti, "PAN AIR — A Computer Program for Predicting Subsonic or Supersonic Linear Potential Flows About Arbitrary Configurations Using a Higher Order Panel Method," *Vol. II — Users's Manual, NASA CR-3252*, May 1980.
7. D.R. Clark and M.A. McVeigh, "Analysis of the Wake Dynamics of a Typical Tilt-Rotor Configuration in Transition Flight," Paper No. 28, *Eleventh European Rotorcraft Forum*, London, Sept. 10-13, 1985.
8. G.J. Carlin, W.E. Staedeli and R.M. Hodges, "Analysis of V-22 Tilt-Rotor Aircraft Using Panel Methods," presented at the *42nd Annual Forum of the American Helicopter Society*, Washington, DC, June 1986.
9. D.B. Bliss, M.E. Teske, and T.R. Quackenbush, "Free Wake Calculations Using Curved Vortex Elements," Proceedings of the *First International Conference on Rotorcraft Basic Research*, Research Triangle Park, NC, Feb. 1985.

10. D.B. Bliss, M.E. Teske, and T.R. Quackenbush, "A New Methodology for Free Wake Analyses Using Curved Vortex Elements," *NASA CR-3958*, Dec. 1987.
11. S.E. Widnall, D.B. Bliss, and A. Zalay, "Theoretical and Experimental Study of the Stability of a Vortex Pair," *Aircraft Wake Turbulence and Its Detection*, ed. by J. Olsen, A. Goldberg, and M. Rogers, Plenum Press, New York, 1971, pp. 305-338.
12. D.W. Moore, and P.G. Saffman, "The Motion of a Vortex Filament with Axial Flow," *Philosophical Transactions of the Royal Society of London*, Vol. 272, July 1972, pp. 403-429.
13. A.J. Landgrebe, "An Analytical and Experimental Investigation of Helicopter Rotor Hover Performance and Wake Geometry Characteristics," *USAAMRDL TR 71-24*, June 1971.
14. J.D. Kocurek and J.L. Tangler, "A Prescribed Wake Lifting Surface Hover Performance Analysis," presented at the *32nd Annual Forum of the American Helicopter Society*, Washington, DC, May 1976.
15. J.D. Kocurek, L.F. Berkowitz, and F.D. Harris, "Hover Performance Methodology at Bell Helicopter Textron," presented at the *36th Annual Forum of the American Helicopter Society*, Washington, DC, May 1980.
16. T.R. Quackenbush, D.B. Bliss, D.A. Wachspress, and C.C. Ong, "Free Wake Analysis of Hover Performance Using a New Influence Coefficient Method," *NASA CR-4150*, 1988.
17. F.F. Felker, T.R. Quackenbush, D.R. Bliss, and J.S. Light, "Comparisons of Predicted and Measured Rotor Performance in Hover Using a New Free Wake Analysis," presented at the *44th Annual Forum of the American Helicopter Society*, Washington, DC, June 16-18, 1988.
18. J.M. Summa, "A Lifting-Surface Method for Hover/Climb Airloads," presented at the *35th Annual Forum of the American Helicopter Society*, Washington, DC, May 1979.
19. M.P. Scully, "Computation of Helicopter Rotor Wake Geometry and Its Influence on Rotor Harmonic Airloads," *Massachusetts Institute of Technology, ASRL TR 178-1*, March 1975.
20. W. Johnson, "A Comprehensive Analytical Model of Rotorcraft Aerodynamics and Dynamics. Part 1, Analysis Development," *NASA TM-81182*, 1980.
21. D.A. Anderson, J.C. Tannehill, and R.H. Pletcher, *Computational Fluid Mechanics and Heat Transfer*, Hemisphere Publishing Corp., New York, 1984.
22. J.J. Chattot, "Calculation of Three-Dimensional Unsteady Transonic Flows Past Helicopter Blades." *NASA Technical Paper 1721*, Oct. 1980.

23. C. Tung, F.X. Caradonna, D.A. Boxwell, and W.R. Johnson, "The Prediction of Transonic Flows on Advancing Rotors," *AHS 40th Annual Forum*, May 1984.
24. A. Desopper, "Study of the Transonic Flow on a Rotor Blade with Different Tip Shapes," presented at the *Tenth European Rotorcraft Forum*, The Hague, Netherlands, Aug. 28-31, 1984.
25. R. Arieli, and M.E. Tauber, "Computation of Subsonic and Transonic Flow about Lifting Rotor Blades," *AIAA Paper 79-1667*, Aug. 1979.
26. I.C. Chang, "Transonic Flow Analysis for Rotors. Part I; Three Dimensional Quasi-Steady Full Potential Calculation," *NASA TP-2375*, 1984.
27. I.C. Chang, "Transonic Flow Analysis for Rotors. Part II; Three Dimensional, Unsteady, Full Potential Calculation," *NASA TP-2375*, Jan. 1985.
28. J.L. Steger and F.X. Caradonna, "A Conservative Implicit Finite Difference Algorithm for the Unsteady Transonic Full Potential Equation," *AIAA-80-1768*, presented at the *AIAA 13th Fluid and Plasma Dynamics Conference*, Snowmass, CO, July 14-16, 1980.
29. J.O. Bridgeman, J.L. Steger, F.X. Caradonna, "A Conservative Finite Difference Algorithm for the Unsteady Transonic Potential Equation in Generalized Coordinates," *AIAA 9th Atmospheric Flight Mechanics Conference*, San Diego, CA, Aug. 9-11, 1982.
30. R.C. Strawn and F.X. Caradonna, "Numerical Modeling of Rotor Flows with a Conservative Form of the Full Potential Equations," *AIAA 24th Aerospace Sciences Meeting*, Reno, NV, Jan. 6-9, 1986.
31. R.C. Strawn and C. Tung, "The Prediction of Transonic Loading on Advancing Helicopter Rotors," *AGARD/FDP Symposium on Application of Computational Fluid Dynamics in Aeronautics*, Aix-en-Provence, France, April 7-10, 1986.
32. L.N. Sankar and D.S. Prichard, "Solution of Transonic Flow Past Rotor Blades Using the Conservative Full Potential Equation," *AIAA Paper 85-0120*, Jan. 1985.
33. F.X. Caradonna and J.J. Philippe, "The Flow over a Helicopter Blade Tip in the Transonic Regime," *Vertica*, Vol. 2, 1978, pp. 43-60.
34. J.J. Philippe and J.J. Chattot, "Experimental and Theoretical Studies on Helicopter Blade Tips at ONERA," presented at the *Sixth European Rotorcraft and Powered Lift Aircraft Forum*, Bristol, U.K., Paper No. 46, Sept. 1980, pp. 16-19.
35. B. Monnerie and J.J. Philippe, "Aerodynamic Problems of Helicopter Blade Tips," *Vertica*, Vol. 2, pp. 217-231.

36. Y. Yu, J.K. Kittleson and F. Becker, "Reconstruction of a Three-Dimensional Transonic Rotor Flow Field From Holographic Interferogram Data," *41st American Helicopter Society Forum*, Fort Worth, TX, May 1985.
37. J.O. Bridgeman, R.C. Strawn, and F.X. Caradonna, "An Entropy and Viscosity Corrected Potential Method for Rotor Performance Prediction," *Proceedings of the 42nd Annual Forum of the American Helicopter Society*, Washington, D.C., June 16-18, 1988.
38. F.X. Caradonna, A. Desopper, and C. Tung, "Finite Difference Modeling of Rotor Flows Including Wake Effects," *Journal of the American Helicopter Society*, Vol. 29, No. 2, April 1984.
39. J.S. Steinhoff, K. Ramachandran, and K. Suryanarayana, "The Treatment of Convected Vortices in Compressible Potential Flow," *AGARD Symposium on Aerodynamics of Vortical Type Flows in Three Dimensions*, Rotterdam, Netherlands, April 1983.
40. J.S. Steinhoff, and K. Suryanarayana, "The Treatment of Vortex Sheets in Compressible Potential Flow," *Proceedings of AIAA Symposium on Computational Fluid Dynamics*, Danvers, MA, July 1983, pp. 1-8.
41. T.A. Egolf and S.P. Sparks, "Hovering Rotor Airload Prediction Using a Full Potential Flow Analysis with Realistic Wake Geometry," *41st American Helicopter Society Forum*, Ft. Worth, TX, May 1985.
42. F.X. Caradonna and C. Tung, "Experimental and Analytic Studies of a Model Helicopter Rotor in Hover," *NASA TM-81232*, Sept. 1981.
43. C. Tung, F.X. Caradonna, D.A. Boxwell, and W.R. Johnson, "The Prediction of Transonic Flows on Advancing Rotors," *AHS 40th Annual Forum*, May 1984.
44. F.X. Caradonna and C. Tung, "A Review of Current Finite Difference Rotor Flow Methods," *Proceedings of the 42nd Annual Forum of the American Helicopter Society*, June 2-4, 1986, Washington, DC, pp. 967-983.
45. R.C. Strawn and C. Tung, "Prediction of Unsteady Transonic Rotor Loads With a Full-Potential Rotor Code," *Proceedings of the 43rd Annual Forum of the American Helicopter Society*, St. Louis, MO, May 18-20, 1987.
46. A.A. Hassan and B.D. Charles, "Simulation of Realistic Rotor Blade-Vortex Interactions Using a Finite-Difference Technique," AIAA-89-1847, presented at the *AIAA 20th Fluid Dynamics, Plasma Dynamics, and Lasers Conference*, Buffalo, NY, June 12-14, 1989.
47. F.X. Caradonna, R.C. Strawn, and J.O. Bridgeman, "An Experimental and Computational Study of Rotor-Vortex Interactions," Paper No. 18, *Proceedings of the Fourteenth European Rotorcraft Forum*, Milano, Italy, Sept. 20-23, 1988.

48. R.C. Strawn, A. Desopper, J. Miller, and A. Jones, "Correlation of PUMA Airloads-Comparison of CFD Prediction Methods," Paper No. 14, *Fifteenth European Rotorcraft Forum*, Amsterdam, Sept. 12-15, 1989.
49. A. Jameson, W. Schmidt, and E. Turkel, "Numerical Solutions of the Euler Equations by Finite Volume Methods Using Runge-Kutta Time-Stepping Schemes," *AIAA Paper 81-1259*, 1981.
50. R.K. Agarwal, and J.E. Deese, "An Euler Solver for Calculating the Flow Field of a Helicopter Rotor in Hover and Forward Flight," *AIAA Paper 87-1427*, June 1987.
51. N. Kroll, "Computation of the Flow Fields of Propellers and Hovering Rotors Using Euler Equations," Paper No. 28, *Twelfth European Rotorcraft Forum*, Garmisch-Partenkirchen, Germany, Sept. 22-25, 1986.
52. E. Kramer, J. Hertel, and S. Wagner, "Computation of Subsonic and Transonic Helicopter Rotor Flow Using Euler Equations," Paper No. 14, *Thirteenth European Rotorcraft Forum*, Arles, France, Sept. 8-11, 1987.
53. C.L. Chen and W.J. McCroskey, "Numerical Simulation of Helicopter Multi-Bladed Rotor Flow," AIAA-88-0046, *AIAA 26th Aerospace Sciences Meeting*, Reno, NV, Jan. 11-14, 1988.
54. J.S. Steinhoff, and K. Ramachandran, "A Vortex Embedding Method for Free Wake Analysis of Helicopter Rotor Blades in Hover," Paper No. 2-11, *Thirteenth European Rotorcraft Forum*, Arles, France, Sept. 1987.
55. K. Ramachandran, "Free Wake Analysis of Helicopter Rotor Blades in Hover Using a Finite Volume Technique," Ph.D. Thesis, University of Tennessee, Knoxville, Dec. 1987.
56. K. Ramachandran, C. Tung, and F.X. Caradonna, "The Free-Wake Prediction of Rotor Hover Performance Using a Vortex Embedding Method," AIAA 89-0638, *AIAA 27th Aerospace Sciences Meeting*, Reno, NV, Jan. 9-12, 1989.
57. H. Lamb, *Hydrodynamics*, Dover Publications.
58. L. Dadone, F.X. Caradonna, K. Ramachandran, M. Silva, and D. Poling, "The Prediction of Loads on the Boeing Helicopters Model 360 Rotor," presented at the *45th Annual Forum of the American Helicopter Society*, Boston, MA, May 22-24, 1989.
59. N.D. Ham, "Aerodynamic Loading on a Two-Dimensional Airfoil During Dynamic Stall," *AIAA Journal*, Vol. 6, Oct. 1968, pp. 1927-1934.
60. B. Maskew, and F. Dvorak, "Prediction of Dynamic Stall Characteristics Using Advanced Non-linear Panel Methods," presented at the *AFOSR/FJSRL/Univ. of Colorado Workshop on Unsteady Separated Flow*, U.S. Air Force Academy, Colorado Springs, CO, Aug. 1983.

61. J.C. Wu and J.F. Thompson, "Numerical Solutions of Time-Dependent Incompressible Navier-Stokes Equations Using An Integro-Differential Formulation," *Computers and Fluids*, Vol. 1, 1973, pp. 197-215.
62. J.C. Wu, "Zonal Solution of Unsteady Viscous Flow Problems." *AIAA Paper 84-1637*, 1984.
63. U.B. Mehta, "Dynamic Stall of an Oscillating Airfoil," Paper No. 23, *AGARD Conference Proceedings*, CP-227, Symposium on Unsteady Aerodynamics, Ottawa, ON, Canada.
64. N.L. Sankar and W. Tang, "Numerical Solution of Unsteady Viscous Flow Past Rotor Sections," *AIAA Paper 85-0129*, Jan. 1985.
65. J.A. Ekaterinaris, "Compressible Studies on Dynamic Stall," *AIAA Paper 89-0024*, *AIAA 27th Aerospace Sciences Meeting*, Jan. 9-12, 1989.
66. L.W. Carr, M.F. Platzer, M.S. Chandrasekhara, and J. Ekaterinaris, "Experimental and Computational Studies of Dynamic Stall," *AIAA 27th Aerospace Sciences Meeting*, Reno, NV, Jan. 9-12, 1989.
67. E.P.N. Duque, "A Numerical Analysis of the British Experimental Rotor Program Blade," *Proceedings of the 45th Annual Forum of the American Helicopter Society*, Boston, MA, May 22-24, 1989, pp. 523-532.
68. W.A. Spivey and G.G. Morehouse, "New Insights into the Design of Swept-Tip Rotor Blades," *26th Annual Forum of the American Helicopter Society*, Washington, DC, June, 1970.
69. W.A. Spivey, "A Study to Investigate the Aerodynamics of Rotor Blade Tip Shapes," *Bell Helicopter Company Rept. 299-099-468*, Jan. 1970.
70. G.R. Srinivasan, W.J. McCroskey, J.D. Baeder, and T.A. Edwards, "Numerical Simulation of Tip Vortices of Wings in Subsonic and Transonic Flows," Vol. 26, No. 10, Oct. 1988, pp. 1153-1162.
71. M.M. Rai, "Navier-Stokes Simulations of Blade-Vortex Interaction Using High-Order Accurate Upwind Schemes," *AIAA-87-0543*, *AIAA 25th Aerospace Sciences Meeting*, Reno, NV, Jan. 12-15, 1987.
72. J.D. Baeder, "Computation of Non-linear Acoustics in Two-Dimensional Blade-Vortex Interactions," Paper No. 1-1, *Thirteenth European Rotorcraft Forum*, Arles, France, Sept. 8-11, 1987.
73. F.X. Caradonna, G.H. Laub, and C. Tung, "An Experimental Investigation of the Parallel Blade-Vortex Interaction," *Proceedings of the 10th European Rotorcraft Forum*, The Hague, Netherlands, Aug. 1984 (See also NASA TM-86005, Nov. 1984).

74. F.X. Caradonna, J.L. Lautenschlager, and M.J. Silva, "An Experimental Study of Rotor-Vortex Interactions," *AIAA Paper 88-0045*, Reno, NV, Jan. 1988.
75. J. Flores, T.L. Holst, D. Kwak, and D. Batiste, "A New Consistent Spatial Differencing Scheme for the Transonic Full-Potential Equation," *AIAA Journal*, Vol. 22, No. 8, Aug. 1984, pp. 1027-1034.
76. M.J. Siclari, and A. Rubel, "Entropy Corrections to Supersonic Conical Nonlinear Potential Flows," AIAA Paper No. 84-1683, presented at the *AIAA 17th Fluid Dynamics, Plasma Dynamics, and Lasers Conference*, Snowmass, CO, June 25-27, 1984.
77. D.F. Fuglsang, and M.H. Williams, "Non-Isentropic Unsteady Small Disturbance Theory," AIAA Paper No. 85-0600, presented at the *AIAA/ASME/ASCE/AHS 26th Structures, Structural Dynamics, and Materials Conference*, Orlando, FL, April 15-17, 1985.
78. W. Whitlow, "Application of a Nonisentropic Full Potential Method to AGARD Standard Airfoils," AIAA Paper No. 88-0710, presented at the *AIAA 26th Aerospace Sciences Meeting*, Reno, NV, Jan. 11-14, 1988.
79. J.O. Bridgeman, R.C. Strawn, F.X. Caradonna, and C.S. Chen, "Advanced Rotor Computations Using a Corrected Potential Method," presented at the *45th Annual Forum of the American Helicopter Society*, Boston, MA, May 22-24, 1989.
80. C.S. Chen, and J.O. Bridgeman, "Three-Dimensional Viscous Rotor Flow Calculations Using Boundary-layer Equations with Realistic Wake Influence," Paper No. 13, *Fifteenth European Rotorcraft Forum*, Amsterdam, Netherlands, Sept. 12-15, 1989.
81. W.R. VanDalsem, and J.L. Steger, "The Efficient Simulation of Separated Three-Dimensional Viscous Flows Using the Boundary Layer Equations," AIAA-85-4064, *AIAA 3rd Applied Aerodynamics Conference*, Colorado Springs, Co., Oct. 14-16, 1985.

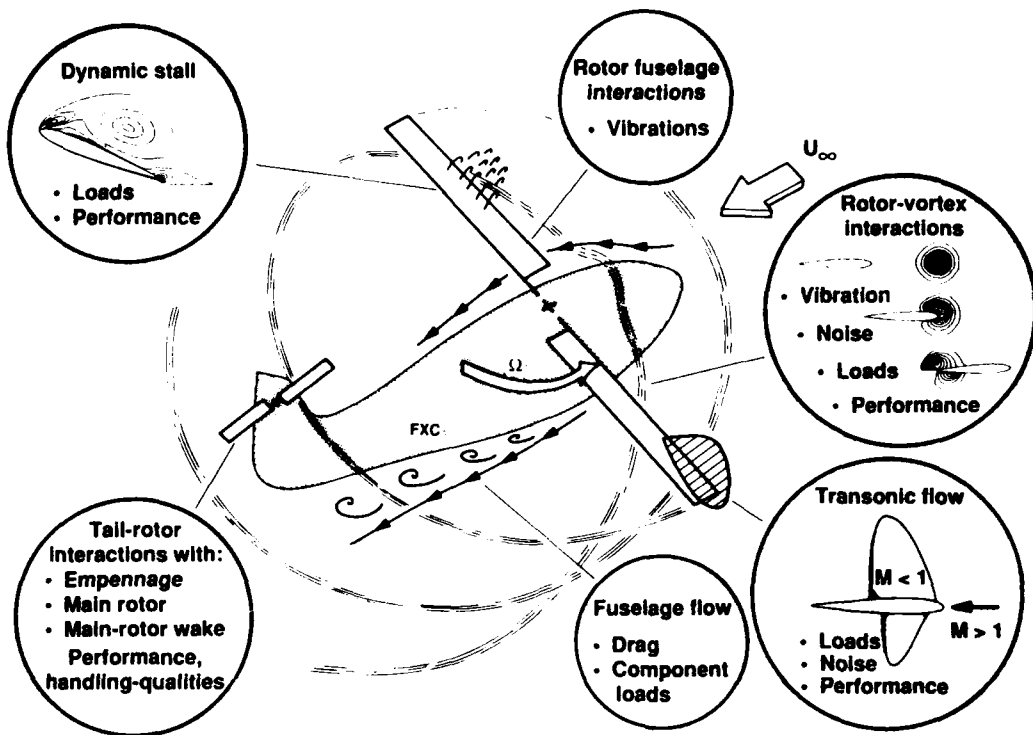


Fig. 1 Rotorcraft flow problems.

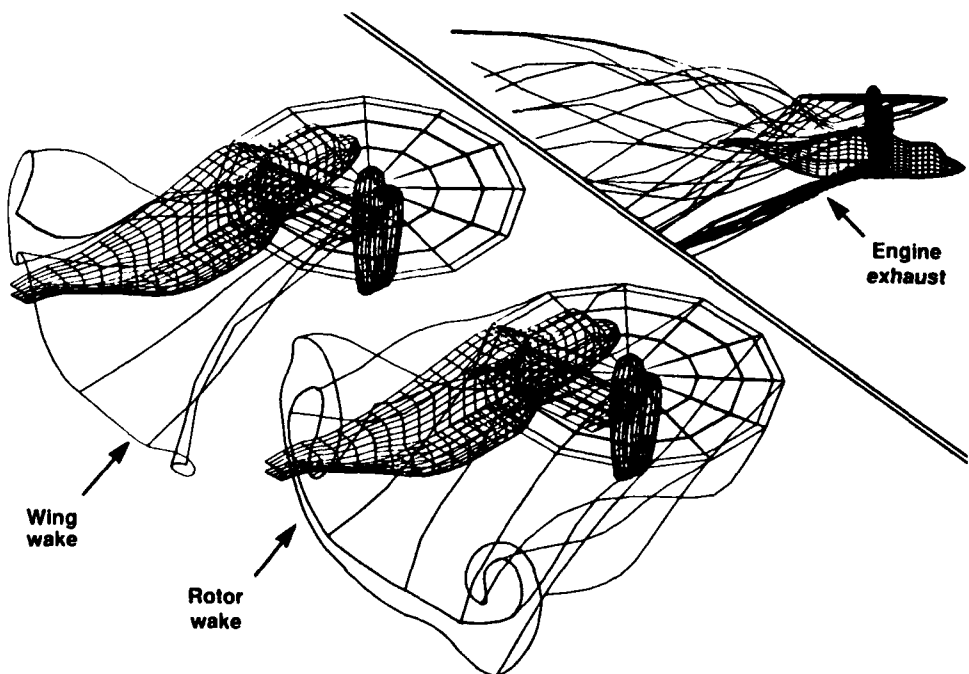


Fig. 2 Panel computation of a complex rotor/wake/fuselage flow using VSAERO. Details of the overall wake structure of a V-22 in a typical transition flight condition. Airspeed 45 knots, $\alpha = -1.5^\circ$, $C_T = 0.015$ [7].

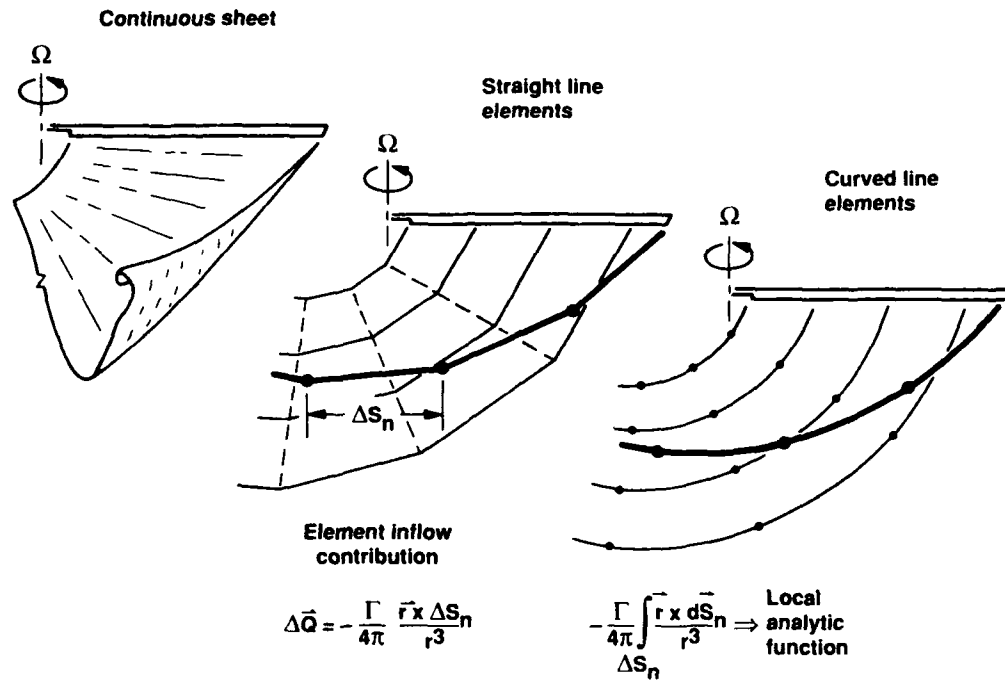


Fig. 3 Vortex lattice models of hovering rotor wakes.

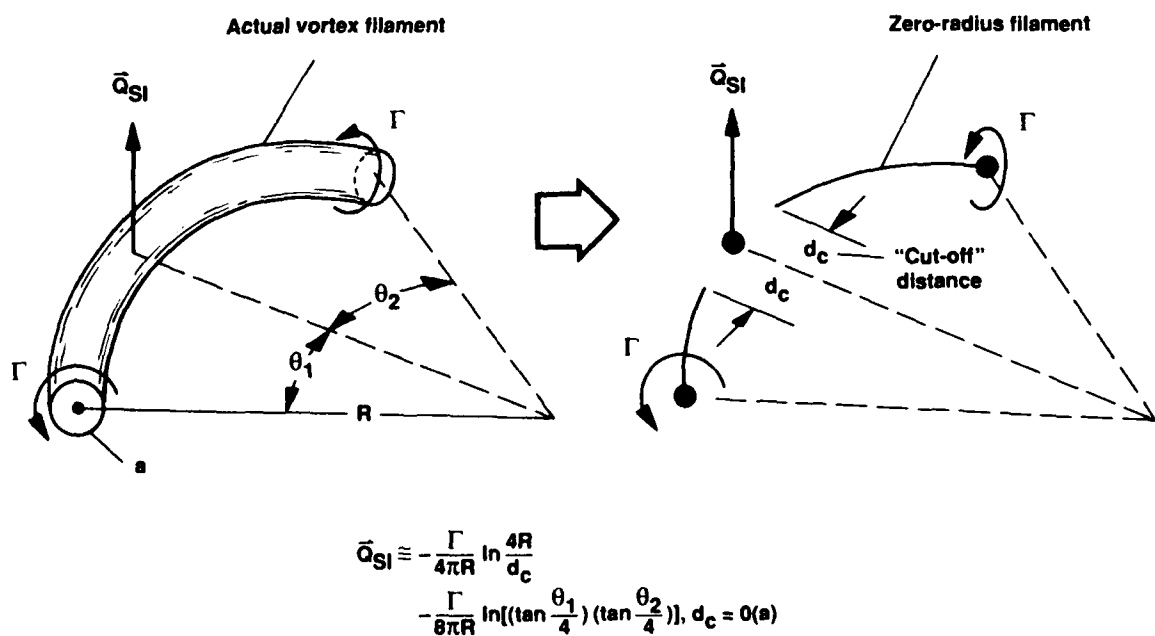


Fig. 4 A local model for self-induction of a vortex element.

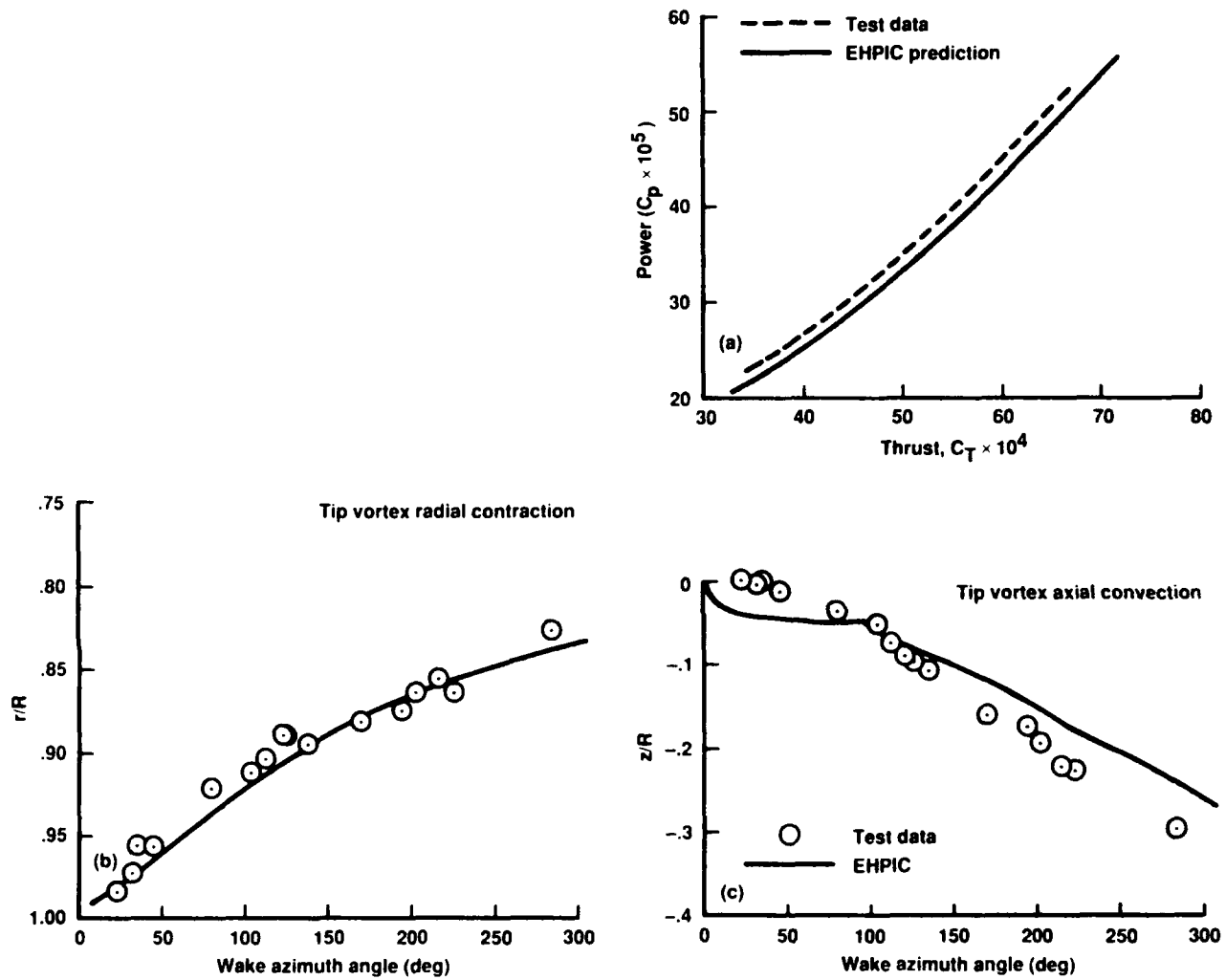


Fig. 5 The free-wake performance prediction of an S-76 rotor [17].

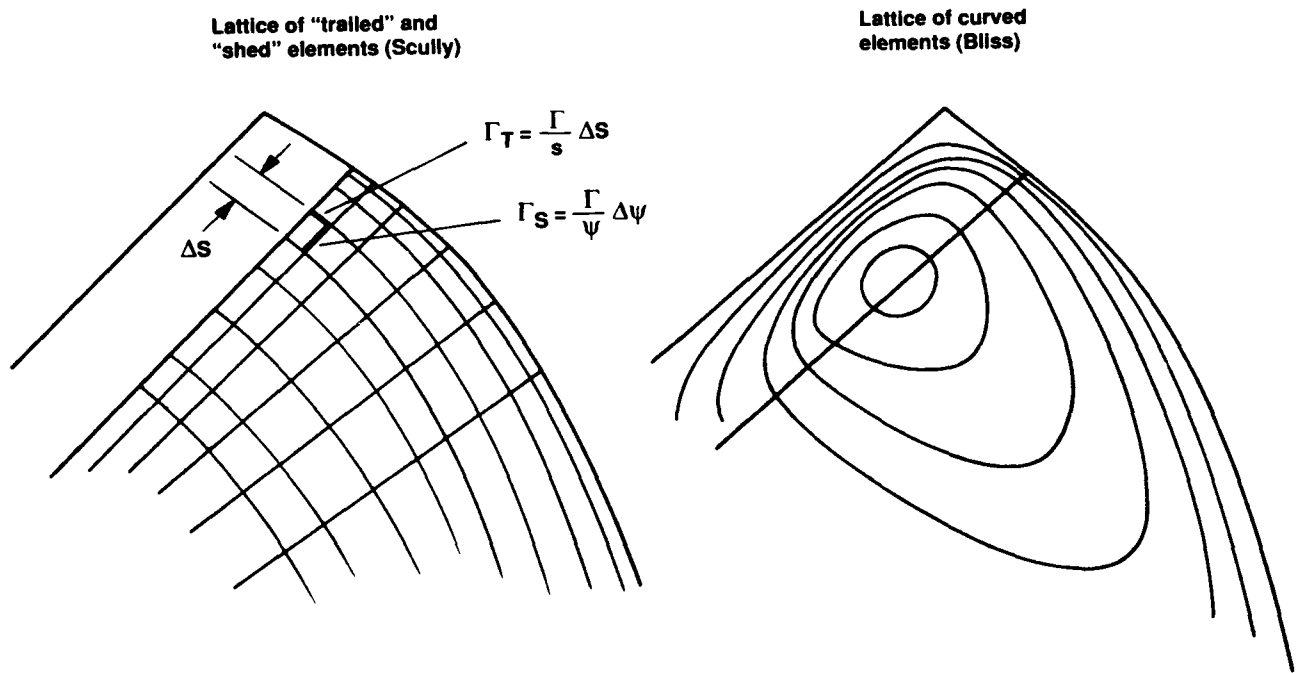


Fig. 6 Vortex lattice representations of advancing rotor wakes.

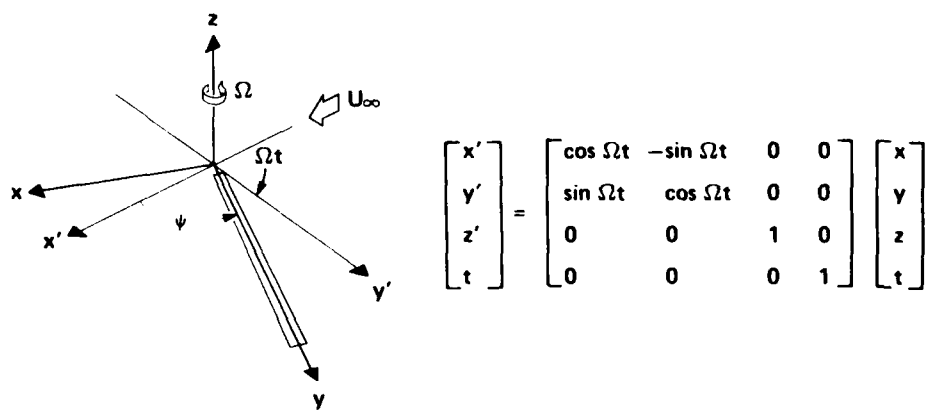


Fig. 7 The transformation from inertial to blade-fixed coordinates.

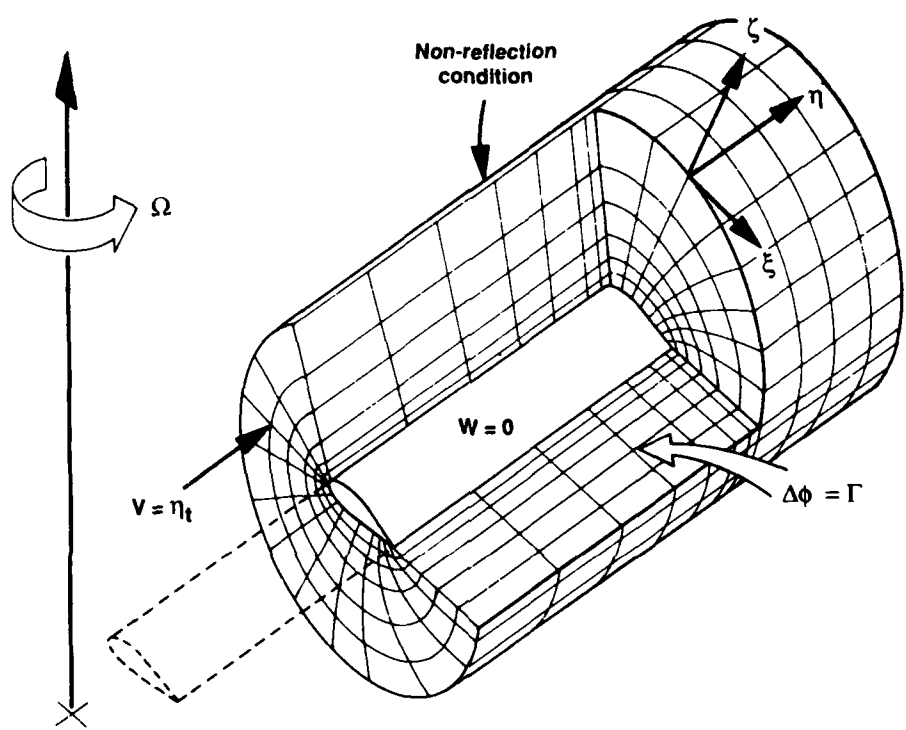
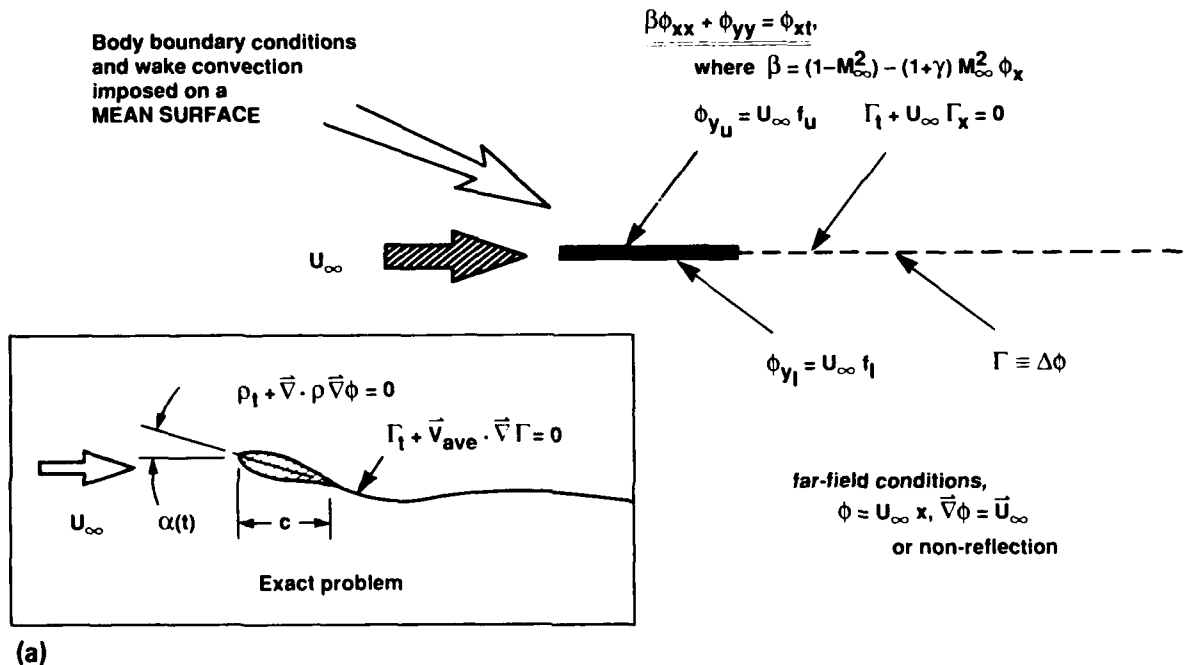
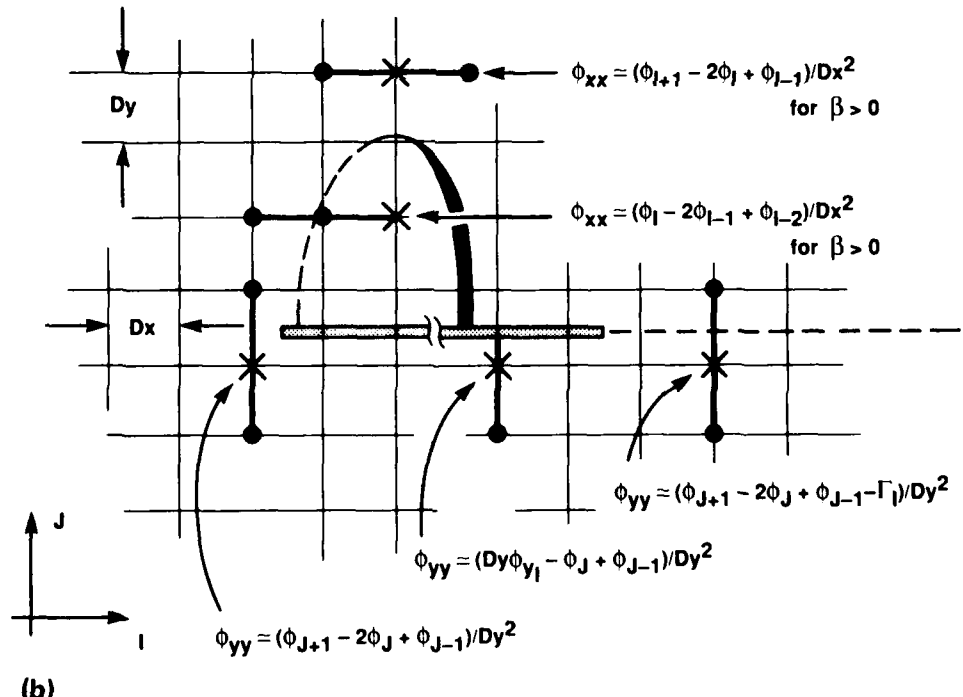


Fig. 8 Grid and boundary conditions for a local rotor-blade computation.



(a)



(b)

Fig. 9 A model problem. (a) Solving for the plunging-pitching motion of an airfoil using the low-frequency, transonic, small-perturbation equation. (b) Difference approximations required for the model problem.

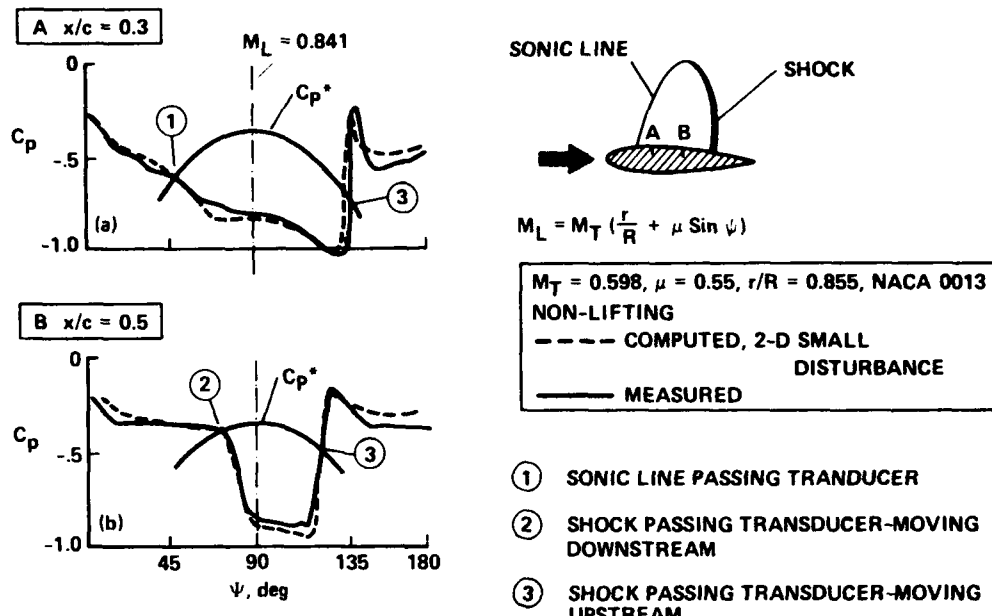


Fig. 10 The transonic flow on a rotor blade, measured and computed using the low-frequency transonic small-perturbation equation, showing the effect of transonic unsteadiness due to the azimuthally varying Mach number [33].

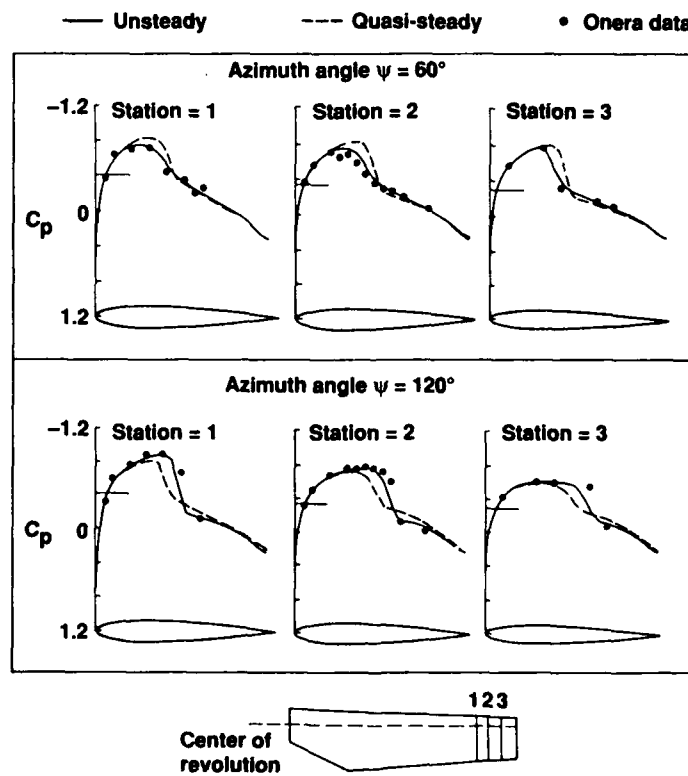


Fig. 11 A comparison of unsteady and quasi-steady, 3-D transonic rotor computations using the TFAR2 nonconservative, full-potential code [27].

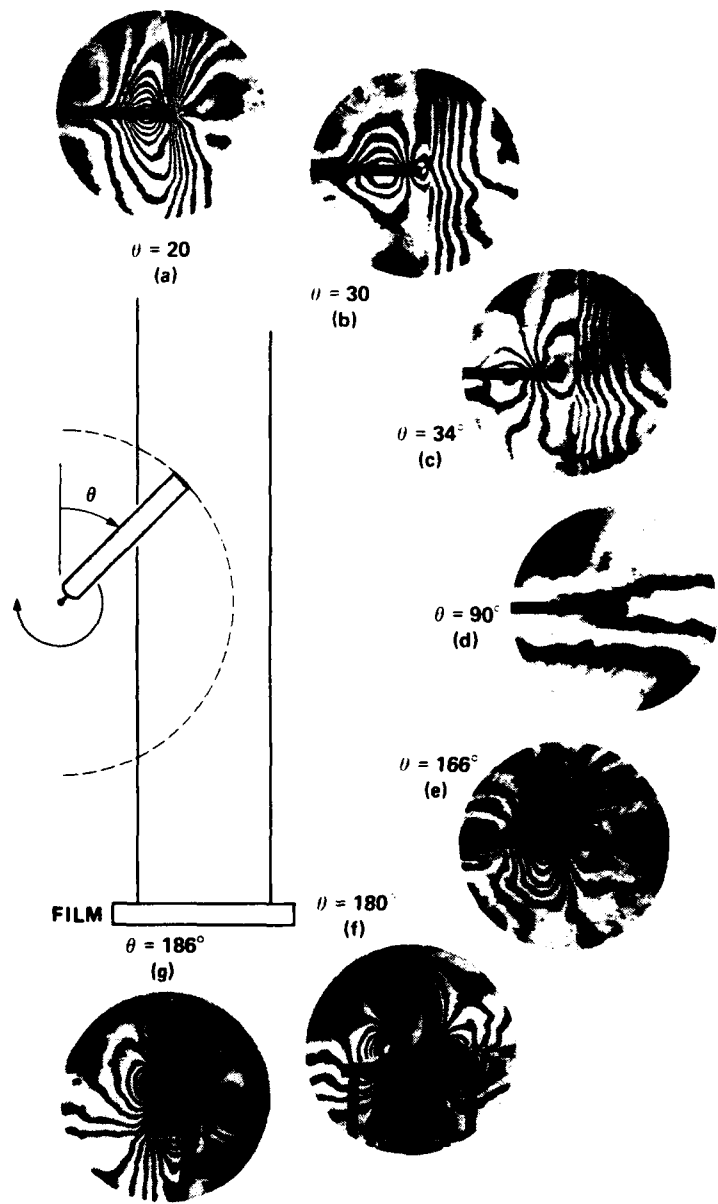


Fig. 12 A novel method for obtaining high-speed rotor flow-field data for code validation: interferograms of a transonic rotor at various azimuth angles [36].

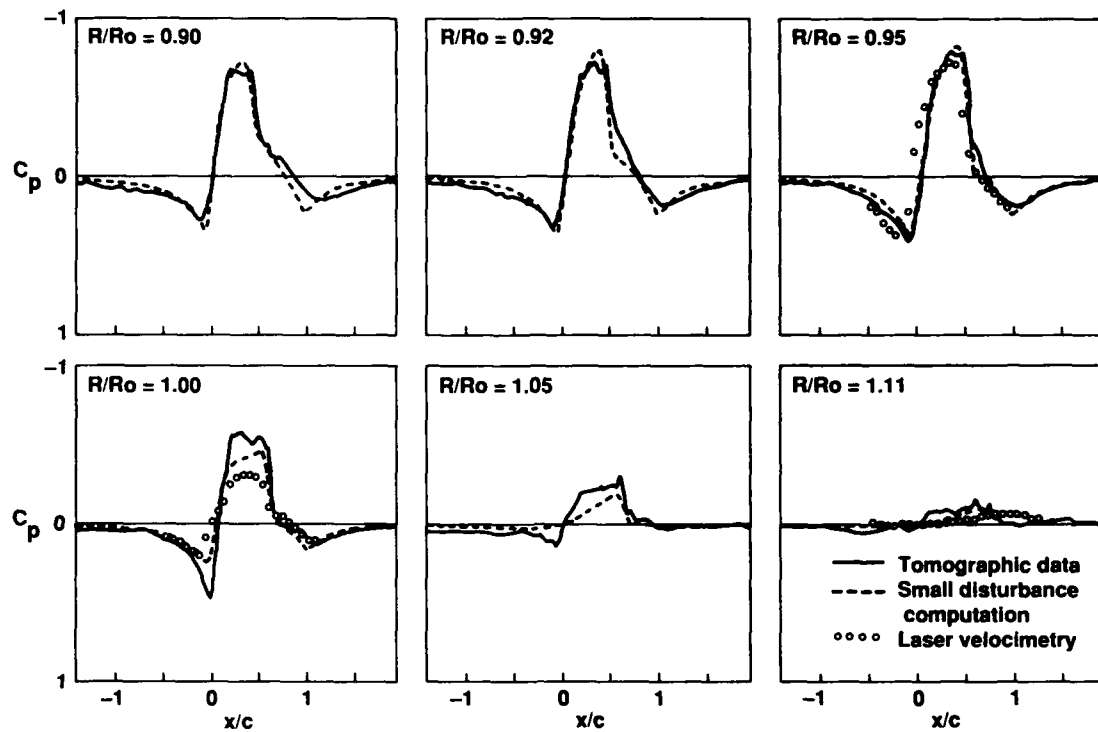


Fig. 13 A comparison of measured and computed near-surface pressure coefficients. Data obtained from tomographic reconstruction of interferograms [36].

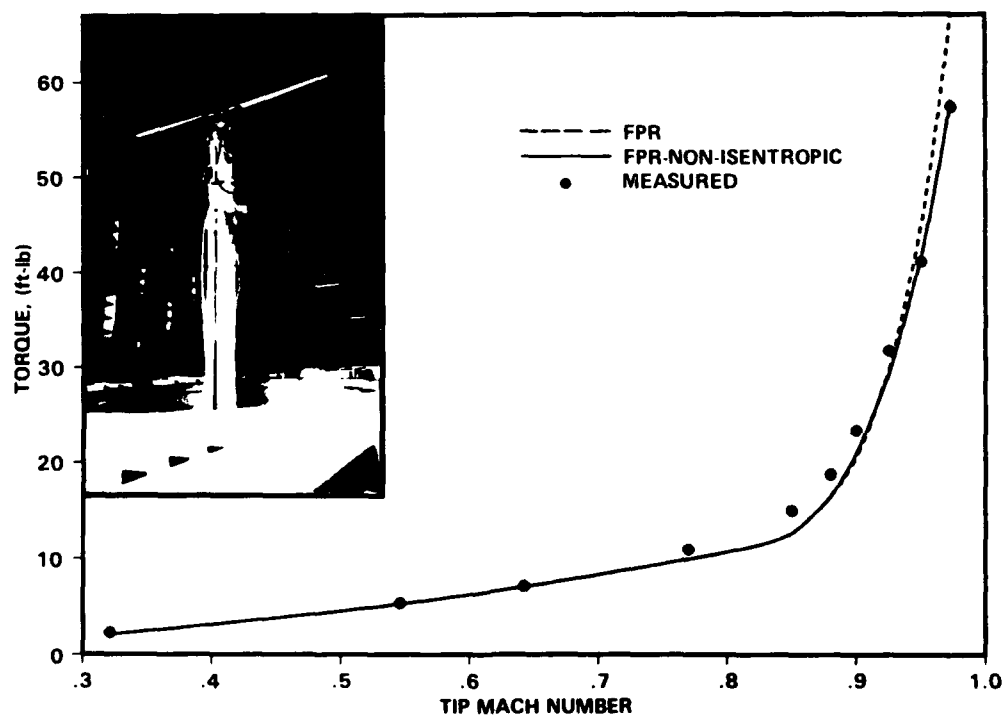


Fig. 14 Measured and computed torque for a nonlifting rotor.

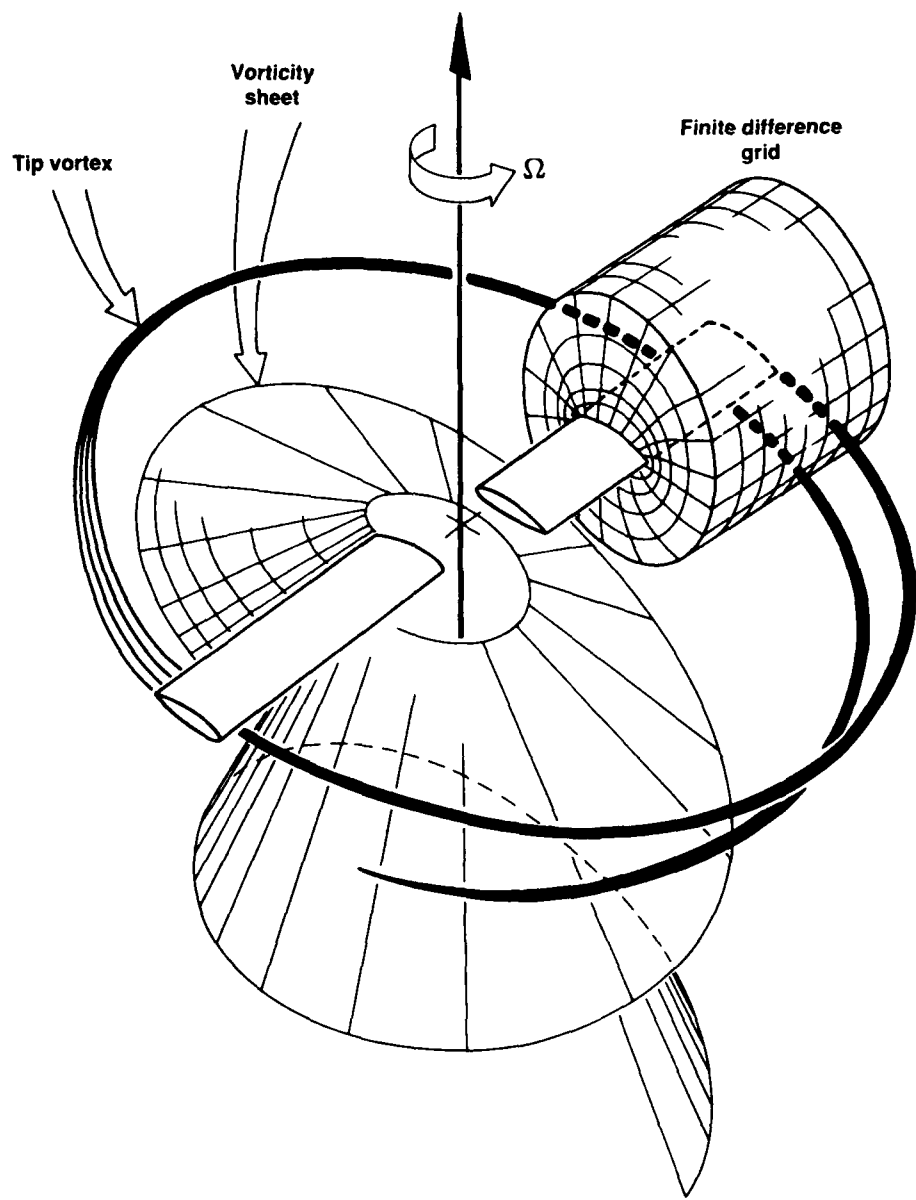


Fig. 15 A finite-difference model embedded in a global hover flow, showing the disparity between a typical blade-oriented grid and the total hovering flow field.

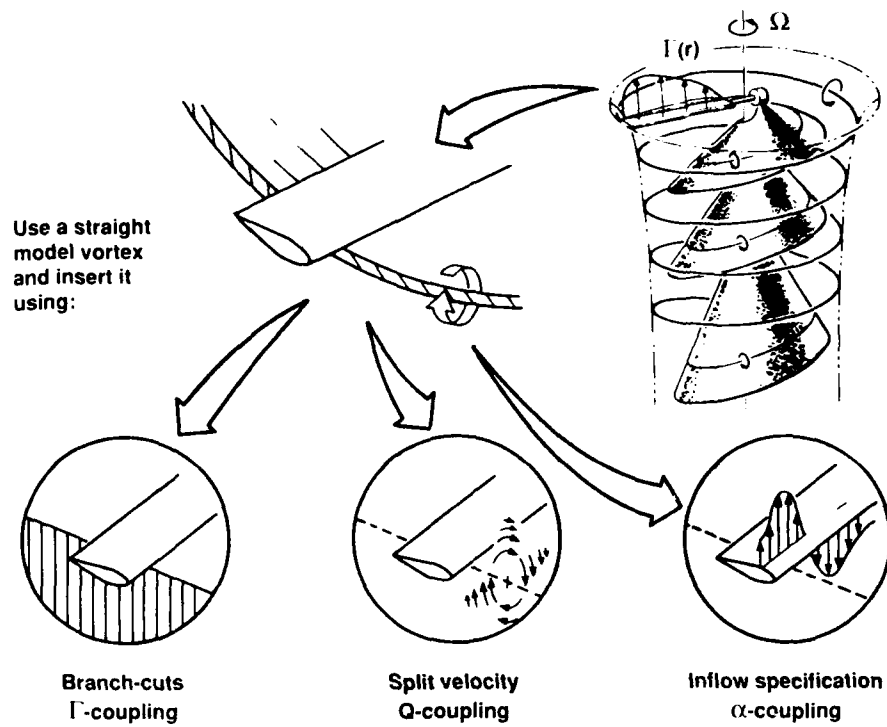


Fig. 16 Near-field blade/vortex modeling methods for use with hybrid methods.

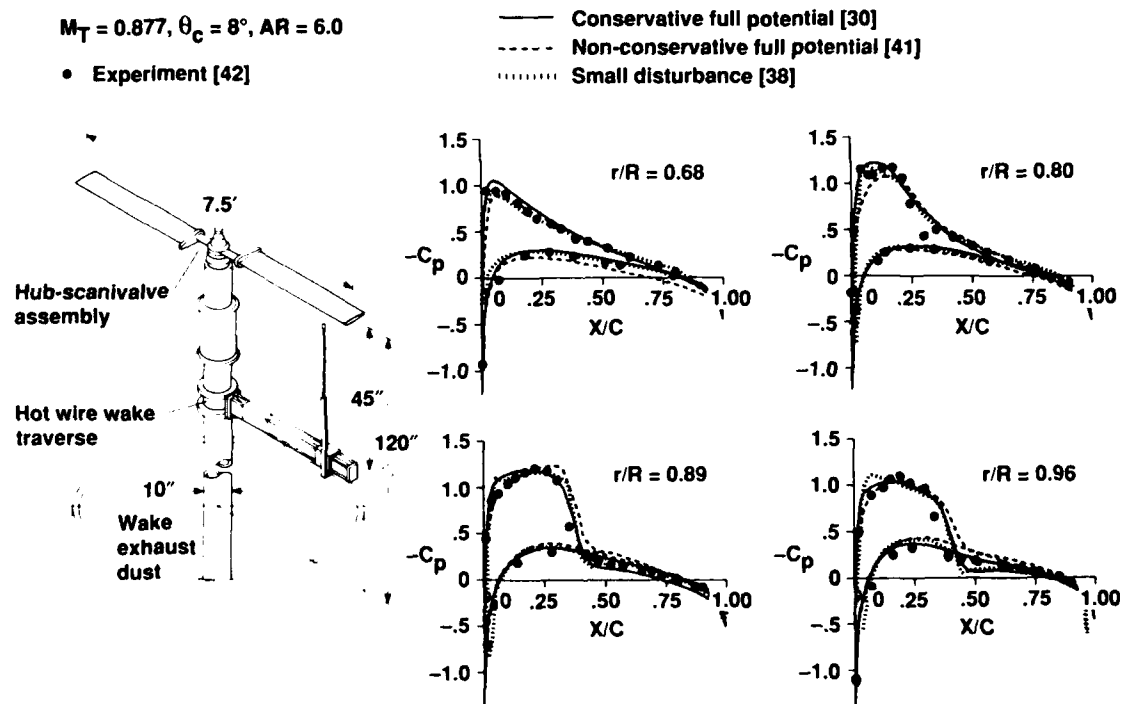


Fig. 17 Measured and computed flow on a hovering rotor—a comparison of various hybrid potential methods for predicting high-speed, hovering flows.

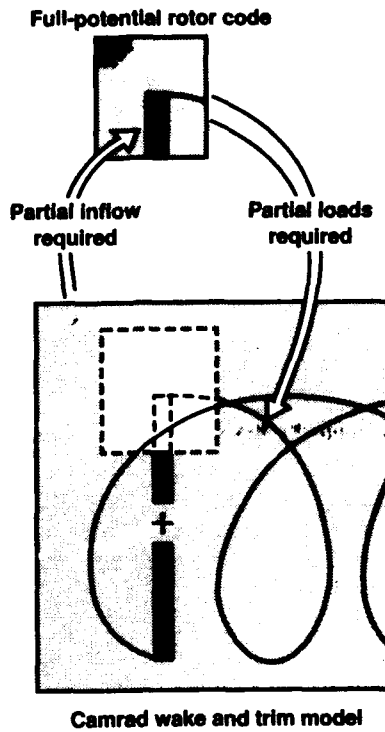


Fig. 18 A hybrid rotor flow prediction scheme for forward flight, using alpha coupling [43].

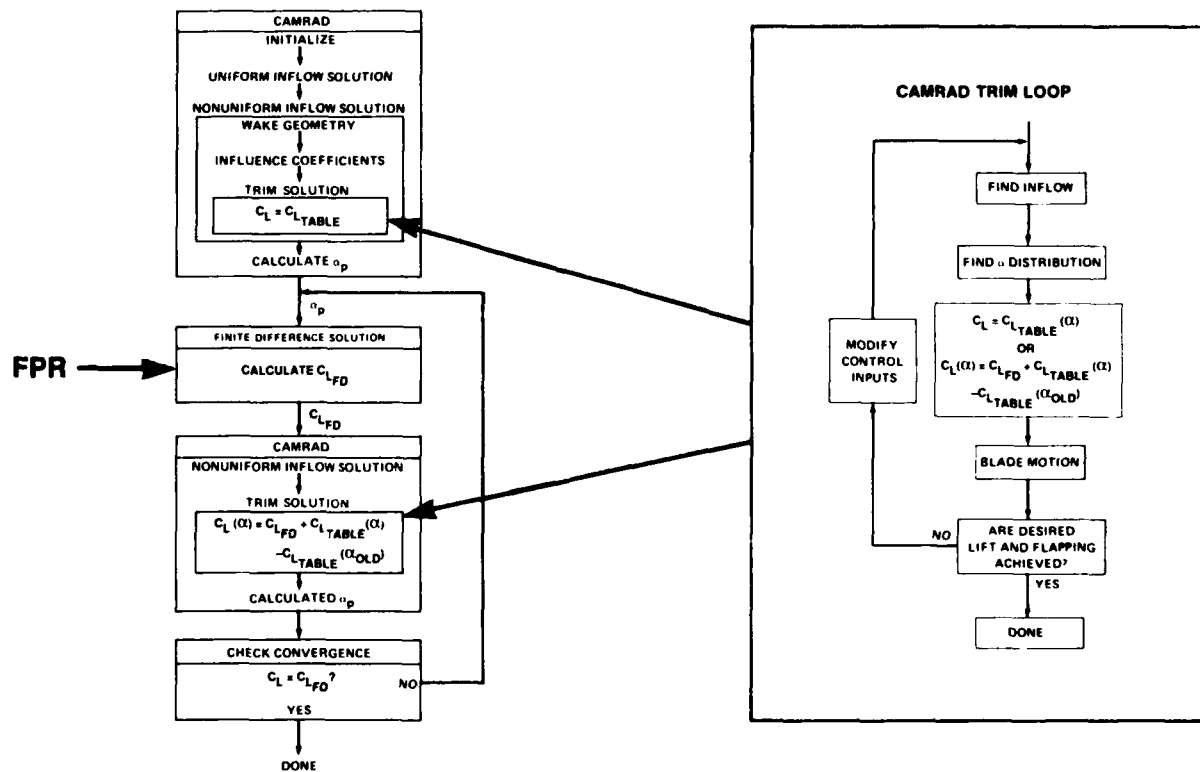


Fig. 19 A flow diagram for the coupled CAMRAD and FPR codes [43].

$M_T = 0.629, \mu = 0.388, \text{ FULL TRIM}$

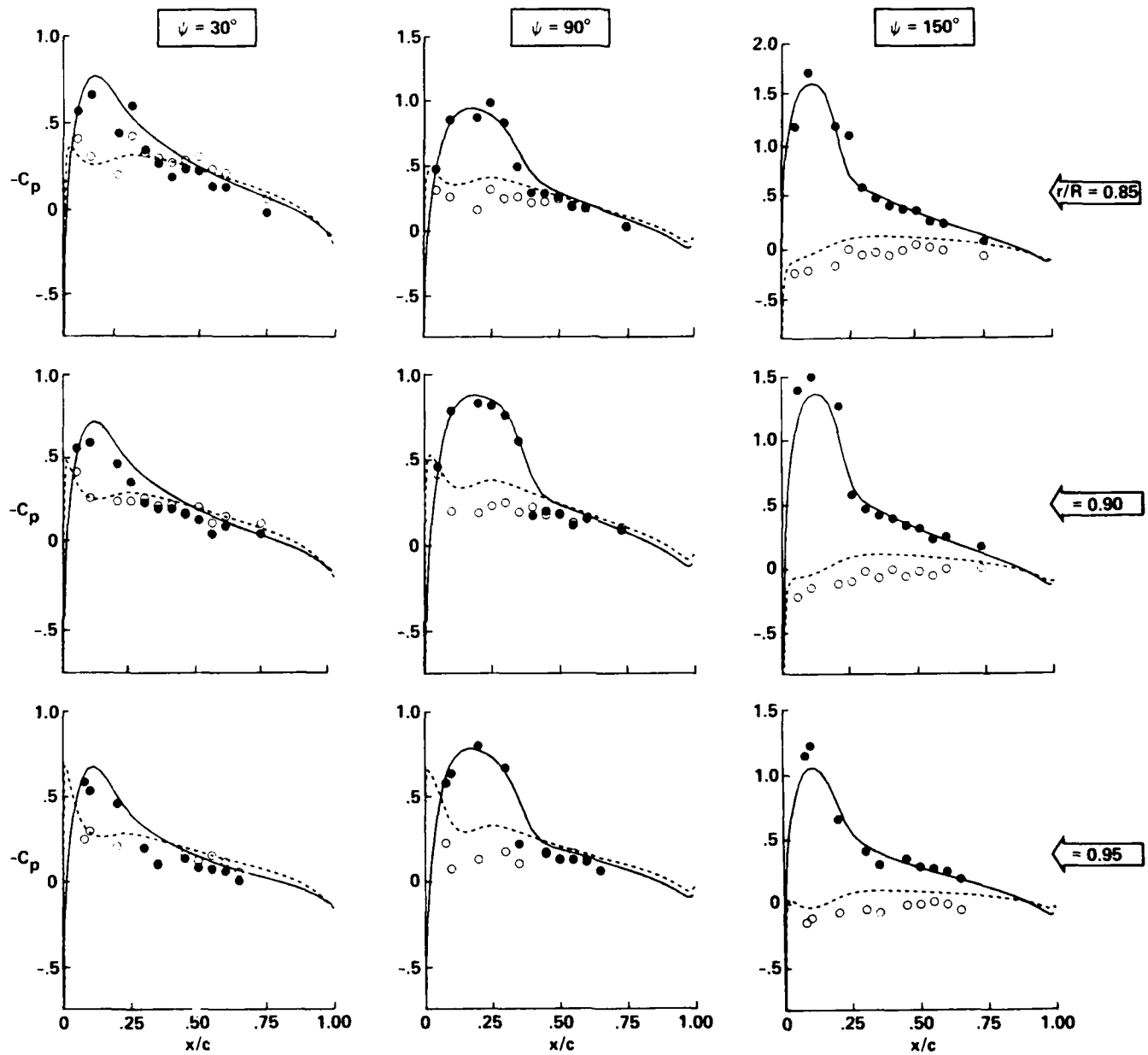


Fig. 20 A comparison of surface pressure data from the ONERA 3-blade model rotor with CAMRAD/FPR results [44].

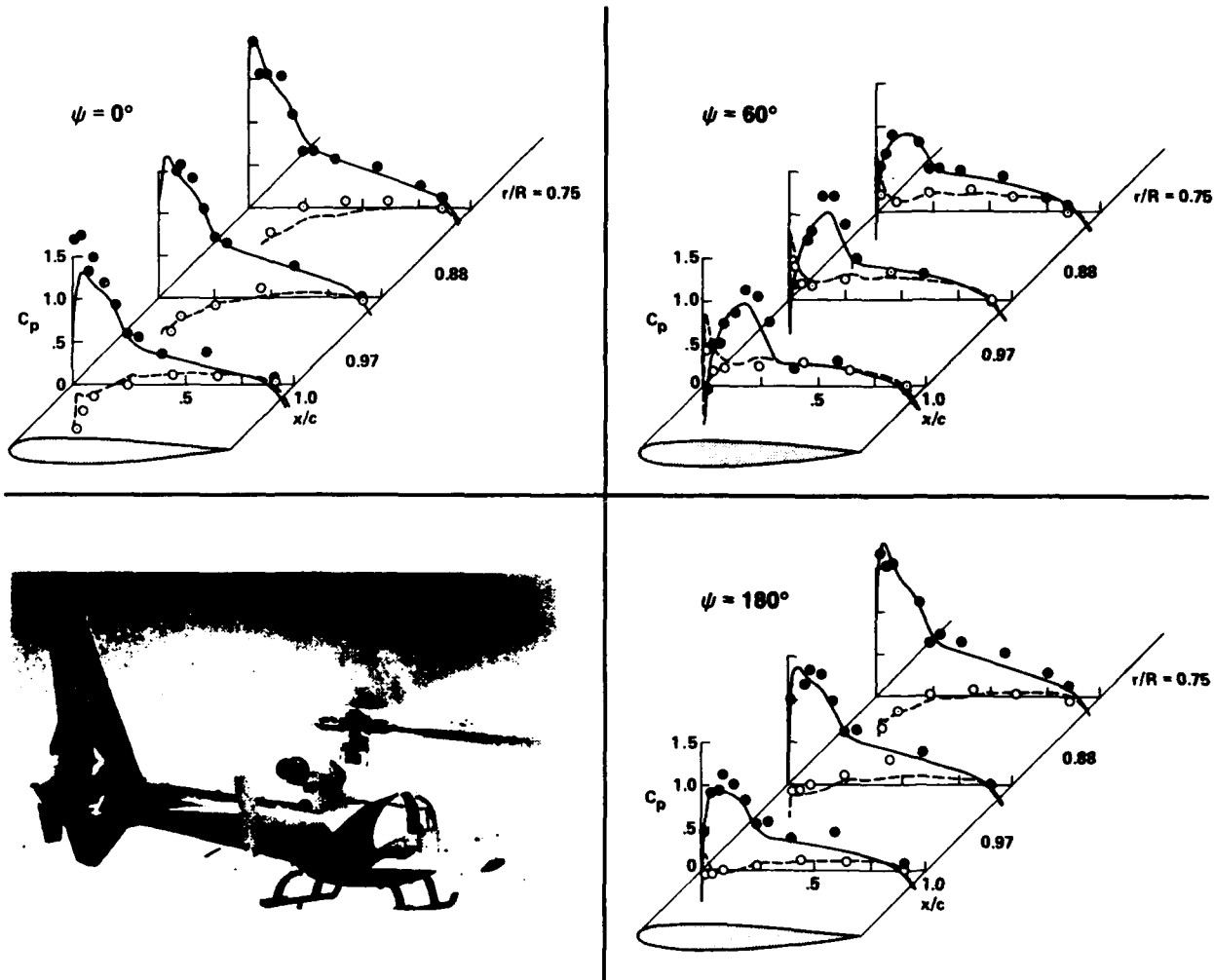


Fig. 21 A comparison of measured and computed surface pressures on an SA349 rotor using CAMRAD/FPR [45].

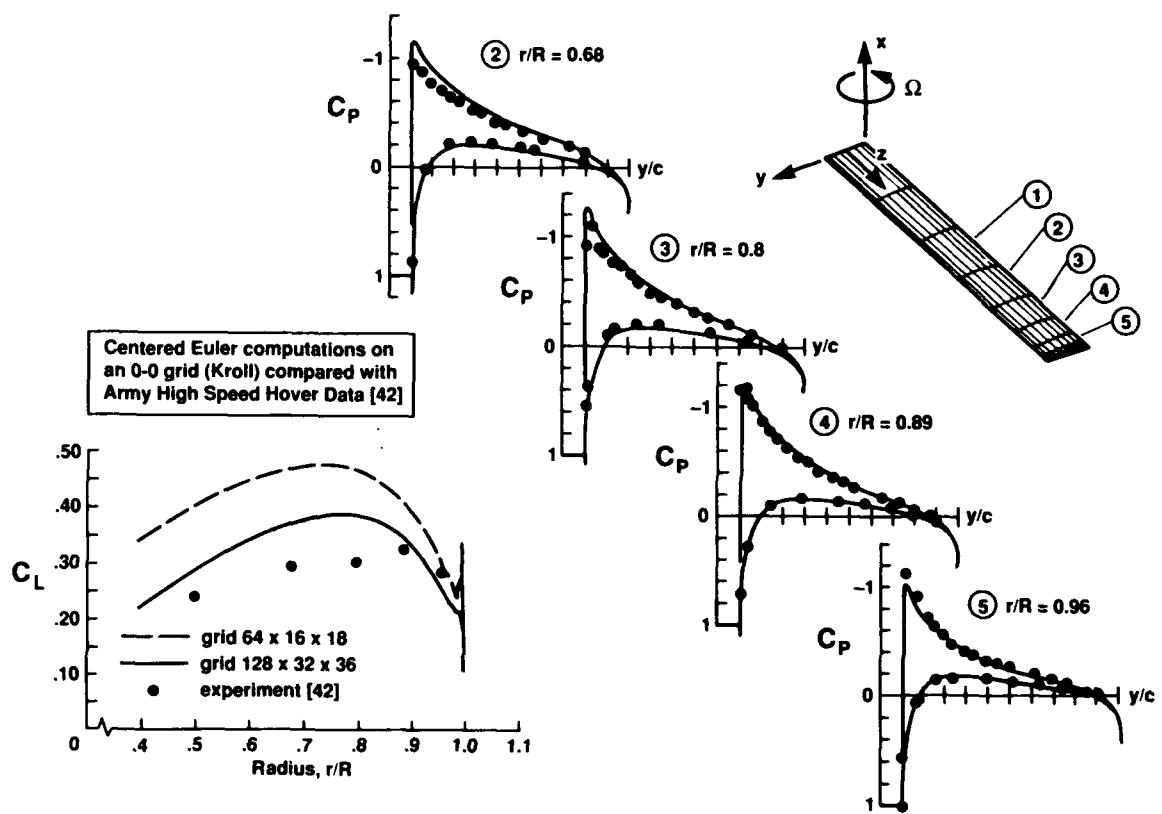


Fig. 22 A comparison of hover surface pressure data with results from a unified rotor/wake computation using a centered Euler scheme [51].

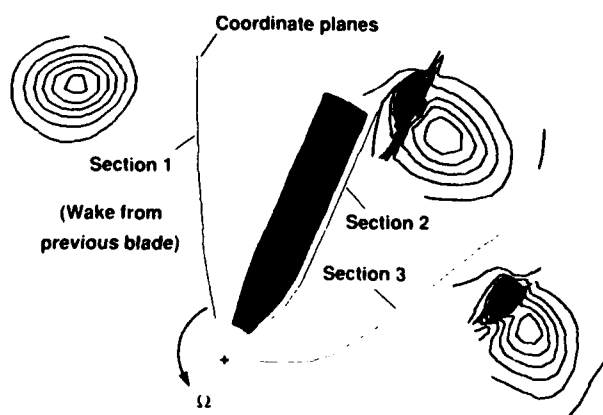


Fig. 23 The dissipation of vorticity in a unified rotor/wake computation using an upwind Euler scheme [53].

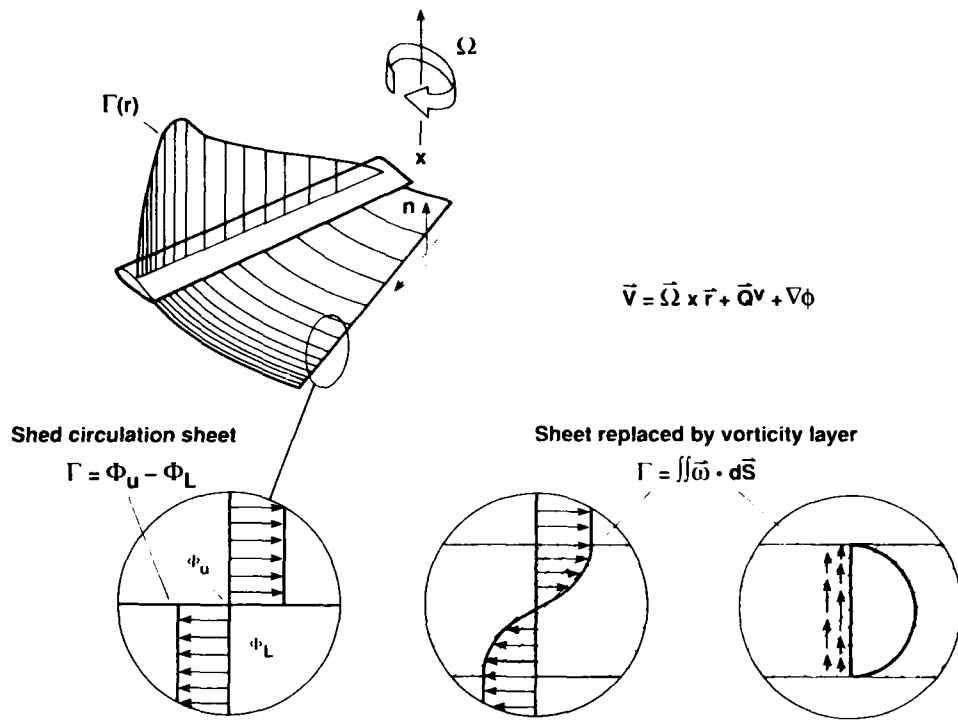


Fig. 24 Alternate models of the shed wake showing a wake reformulation that permits free circulation convection in a potential method [55].

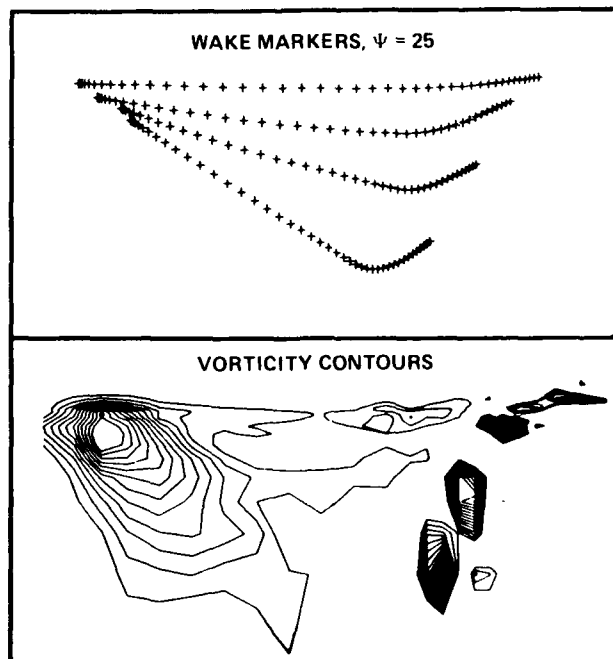


Fig. 25 A computed wake structure for a hovering rotor using the HELIX-I vorticity-convection, full-potential code [56].

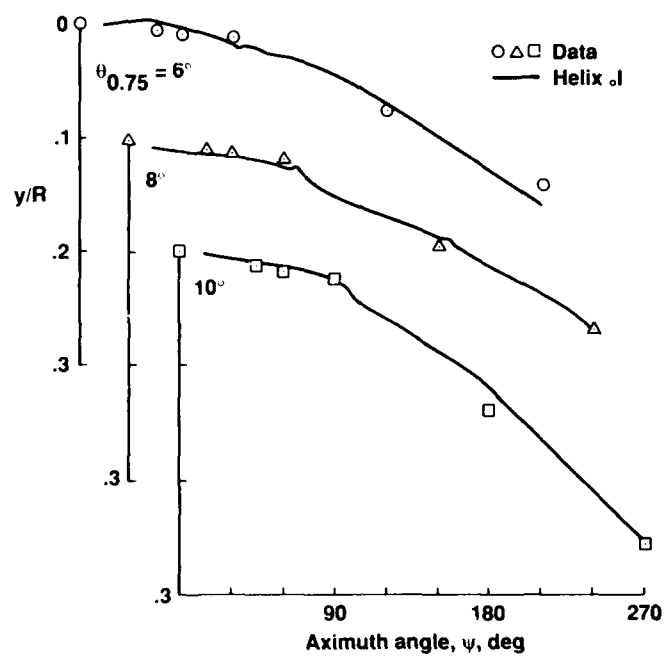


Fig. 26 A comparison of measured and computed axial convection of a tip vortex [56].

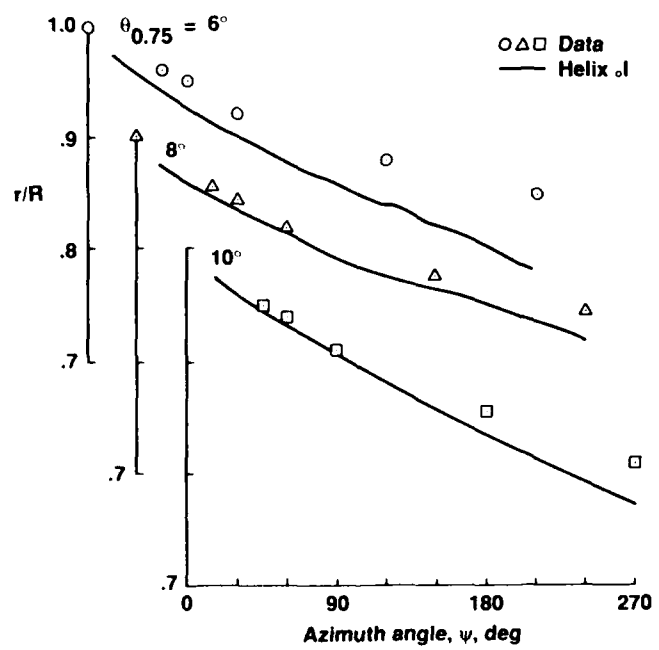


Fig. 27 A comparison of measured and computed radial convection of a tip vortex [56].

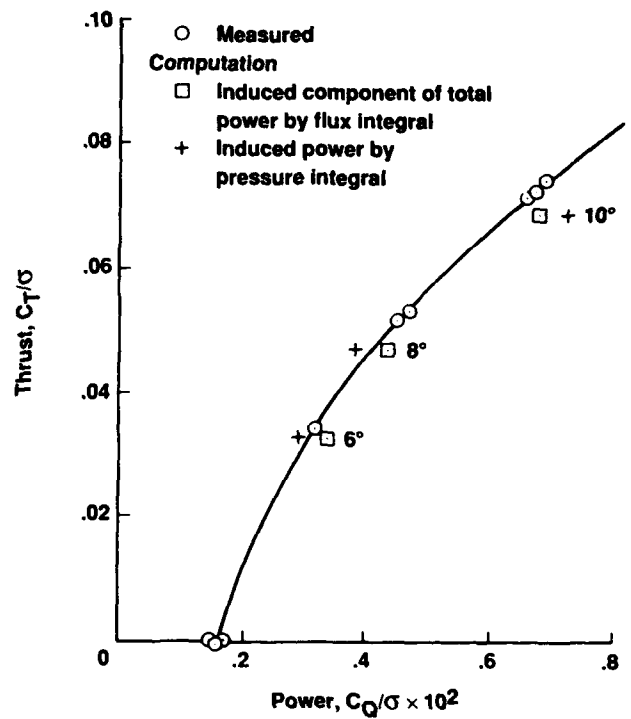


Fig. 28 A comparison of computed and measured rotor hover performance for a 4-blade rotor [56].

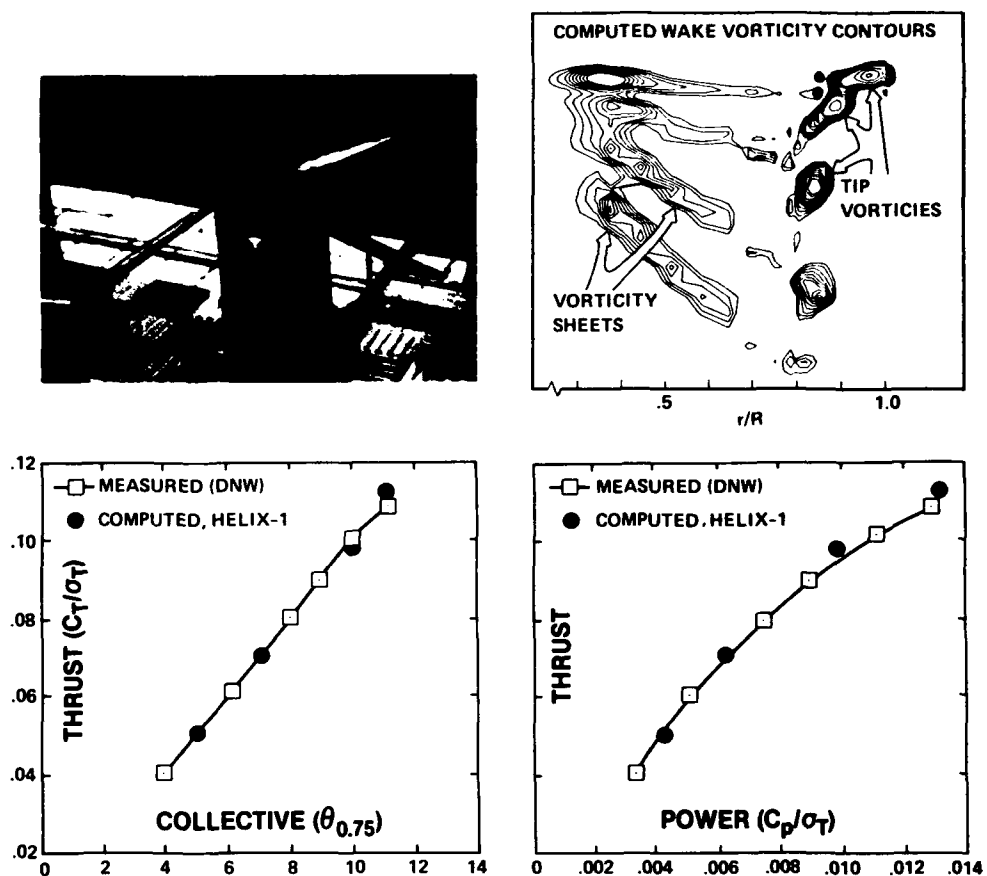


Fig. 29 A comparison of computed and measured rotor hover performance for the Boeing Model 360 rotor [58].

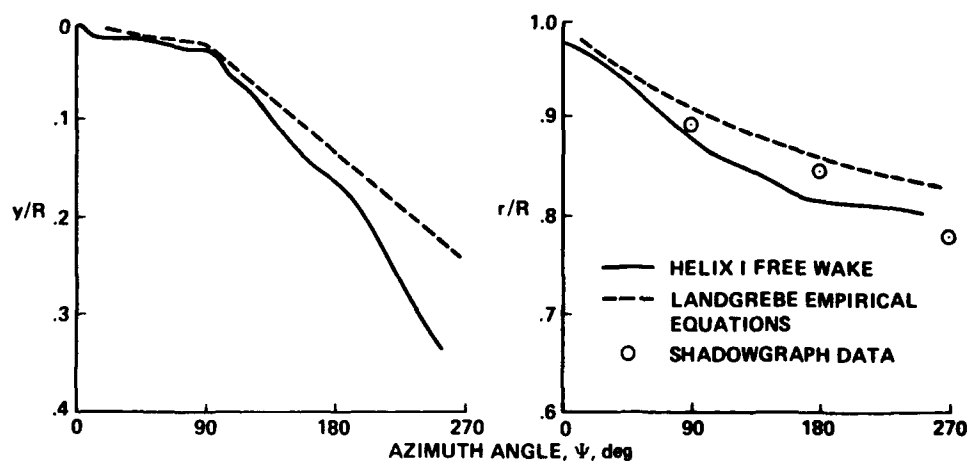


Fig. 30 The computed free convecting wake for the Boeing model 360 rotor [58].

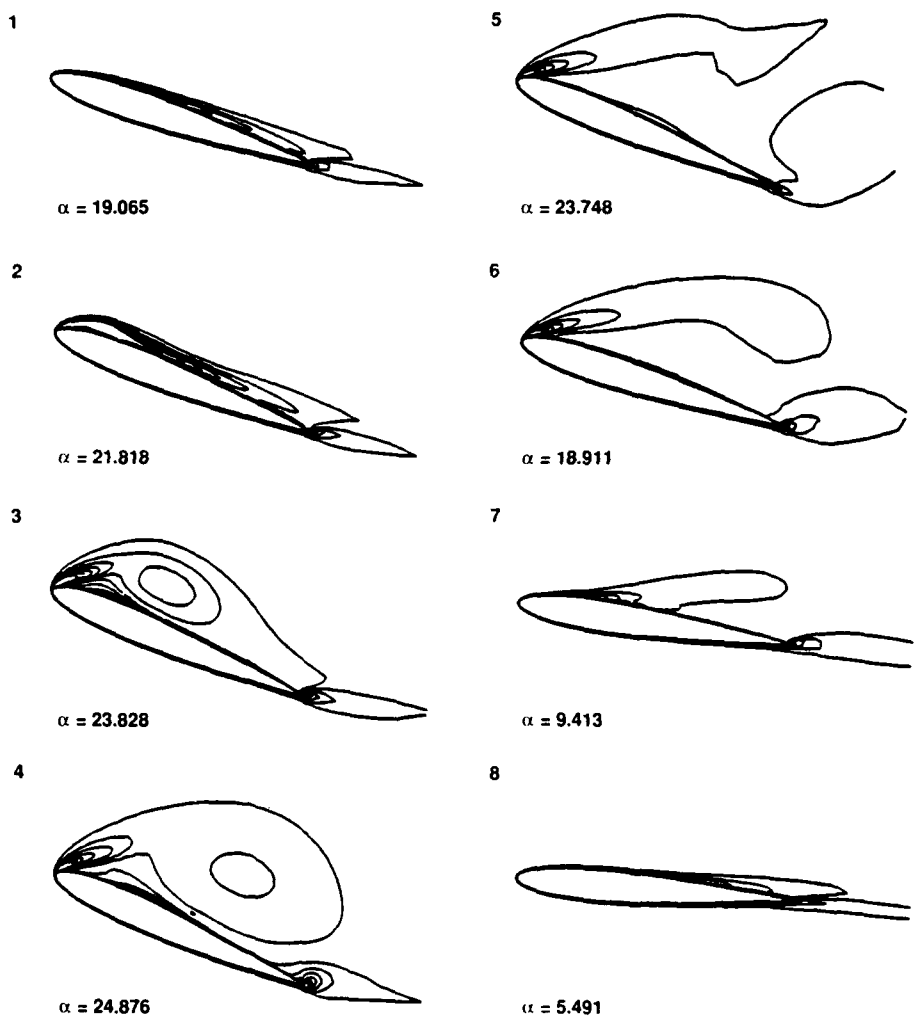


Fig. 31 Vorticity contours for a dynamic stall using an integral-differential scheme [62].

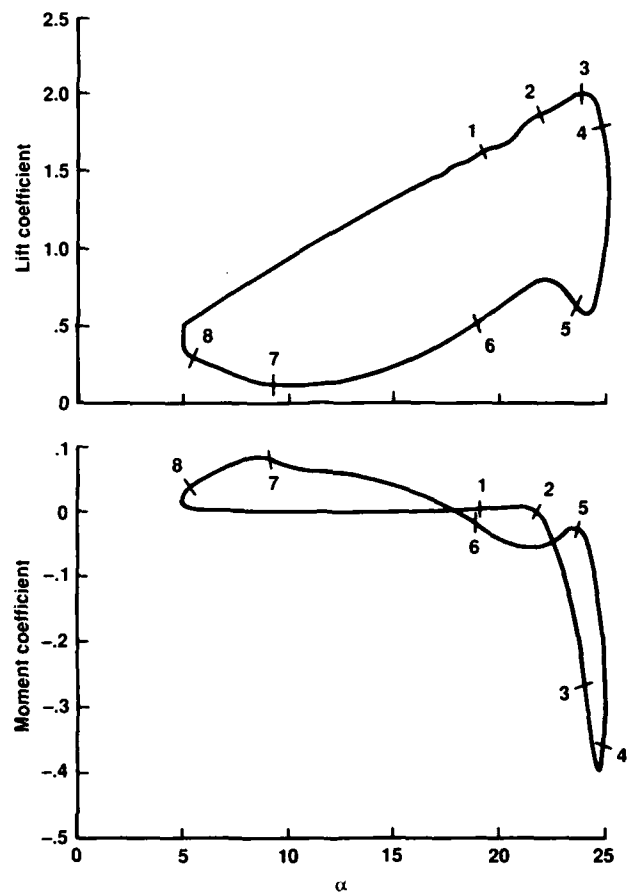


Fig. 32 Lift and moment variations for a dynamic stall using an integral-differential scheme [62].

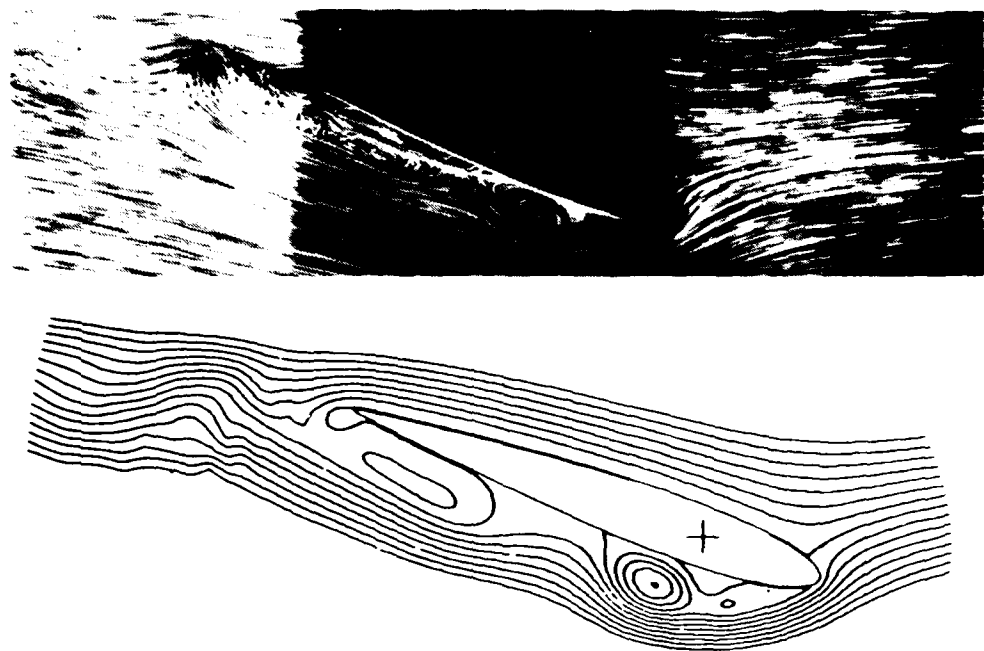


Fig. 33 Comparison of the results of Navier-Stokes computation with visualization of a dynamically stalling airfoil [63].

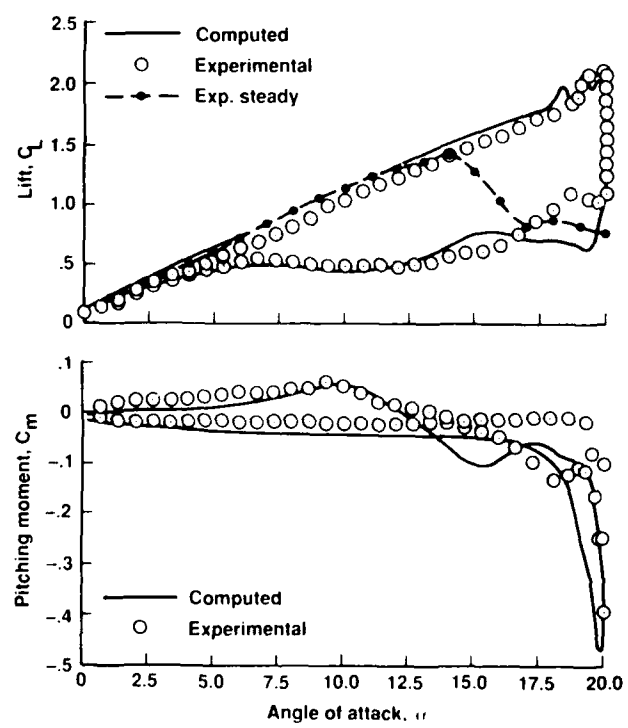


Fig. 34 Experimental and computed lift and moment for a dynamic stall [66].

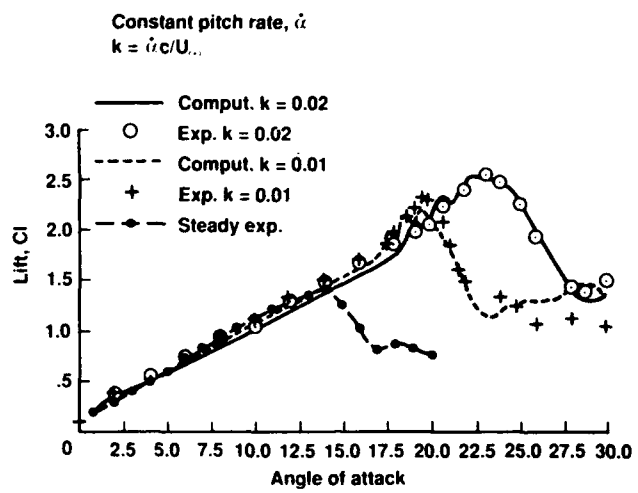


Fig. 35 The lift variation for a dynamically stalling airfoil with constant pitch rate: the effect of pitch rate [66].

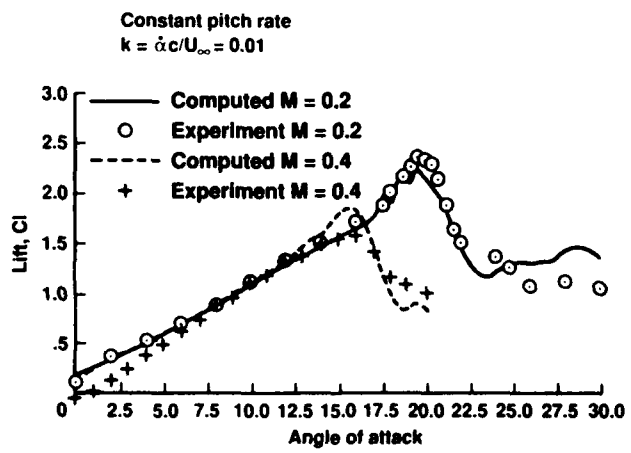


Fig. 36 The lift variation for a dynamically stalling airfoil with constant pitch rate: the effect of Mach number [66].

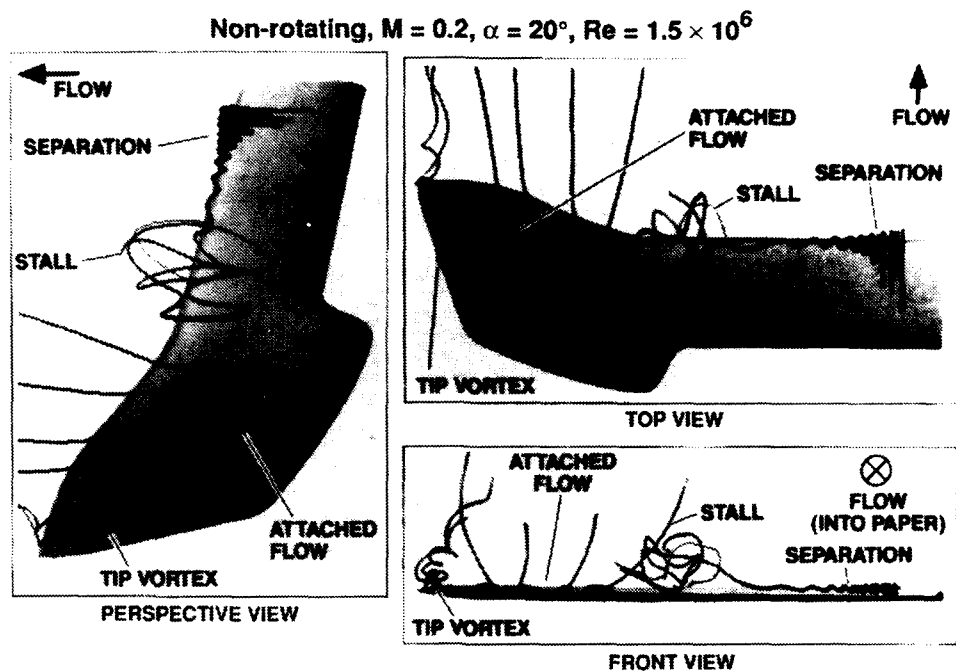


Fig. 37 A particle trajectory visualization of the steady stall of a nonrectangular rotor blade, computed using TNS [67].

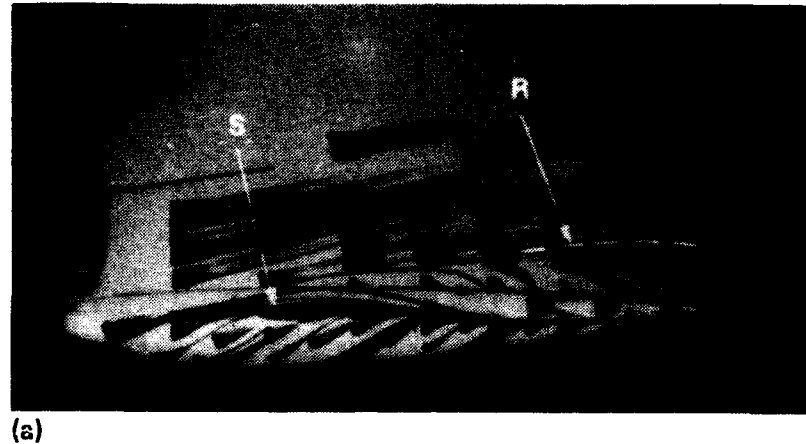


(a) Round tip

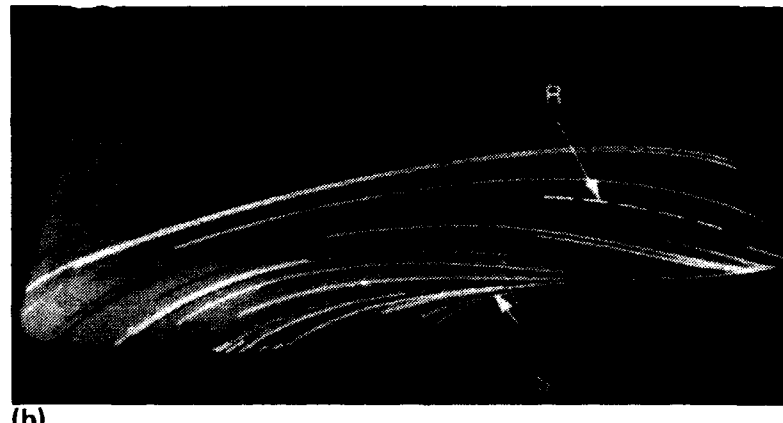


(b) Square tip

Fig. 38 The formation and liftoff of the tip vortex for a rectangular wing. $M_\infty = 0.17$, $\alpha = 11.8^\circ$, and $Re = 2 \times 10^6$ [70].



(a)



(b)

Fig. 39 Tip-vortex studies: a comparison of computed and experimental surface oil flow patterns. $M_\infty = 0.17$, $Re = 2 \times 10^6$ [70]. (a) Round tip-experiment. (b) Round tip-calculations.

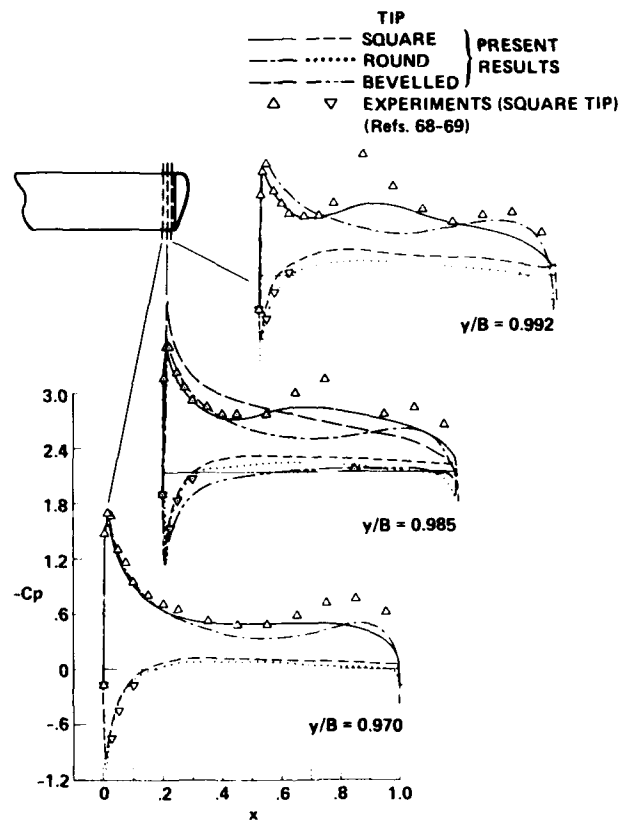


Fig. 40 Surface pressure distributions in the tip region of a rectangular wing with different tip caps. $M_\infty = 0.17$, $\alpha = 11.8^\circ$, and $Re = 2 \times 10^6$ [70].

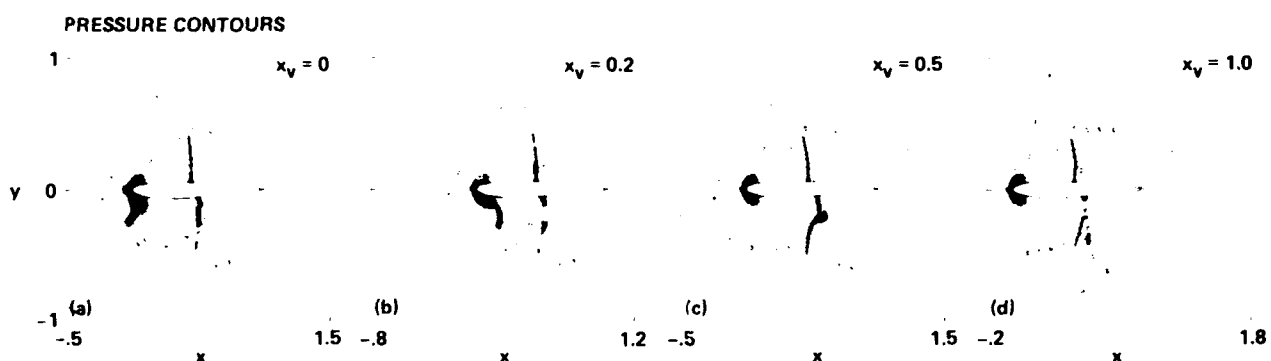
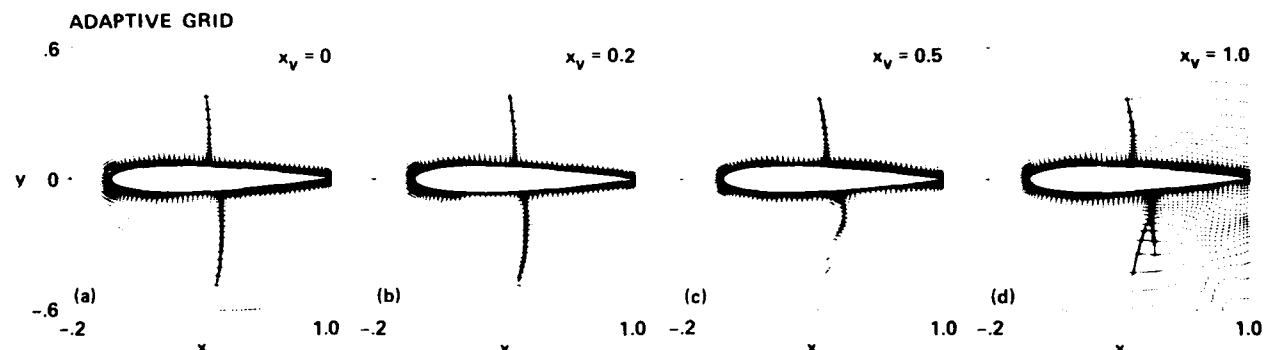
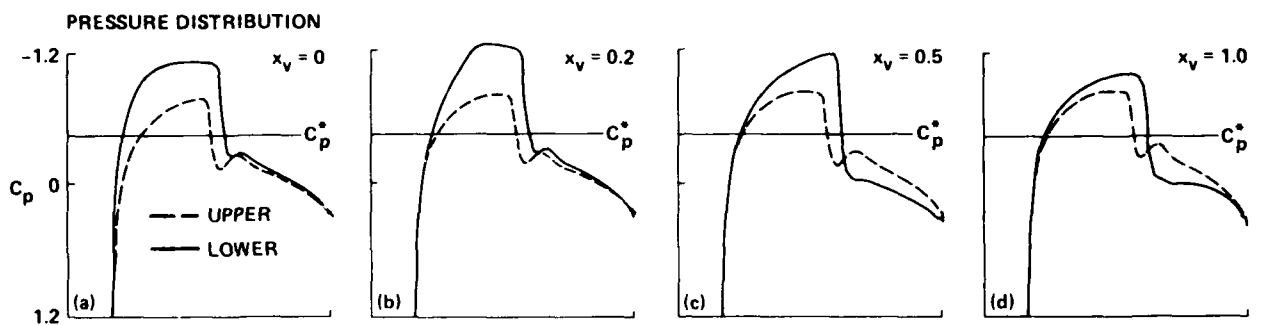


Fig. 41 Instantaneous surface-pressure distributions, adaptive grid, and pressure contours during an airfoil interaction with a convecting vortex. NACA0012, $M_\infty = 0.8$, $\alpha = 0^\circ$, $Re = 2 \times 10^6$, and closest approach distance = -0.26 chords [71].

- Zonal grid, with 3 zones
 - Each zone contains 13,000 to 20,000 grid points

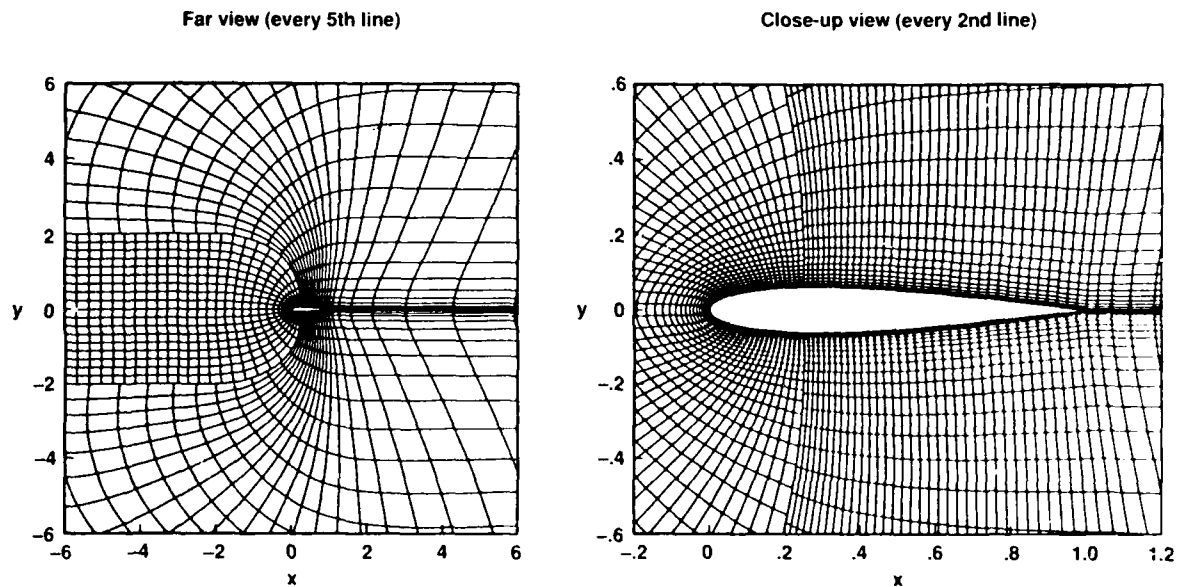


Fig. 42 An Euler/TNS grid for use in airfoil/vortex interaction studies [73].

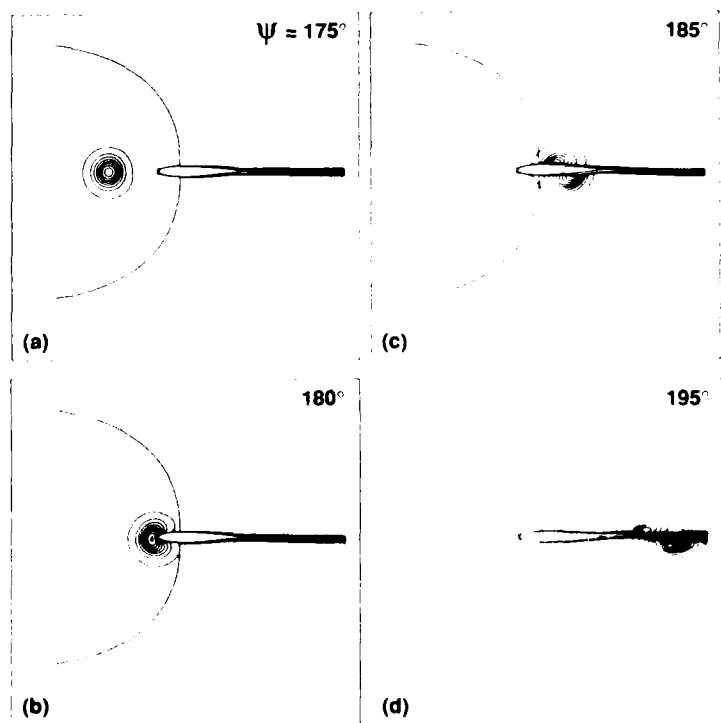


Fig. 43 Vorticity contours for a head-on blade/vortex interaction (BVI) computed using a high-order upwind TNS scheme. $M_\infty = 0.536$ [73].

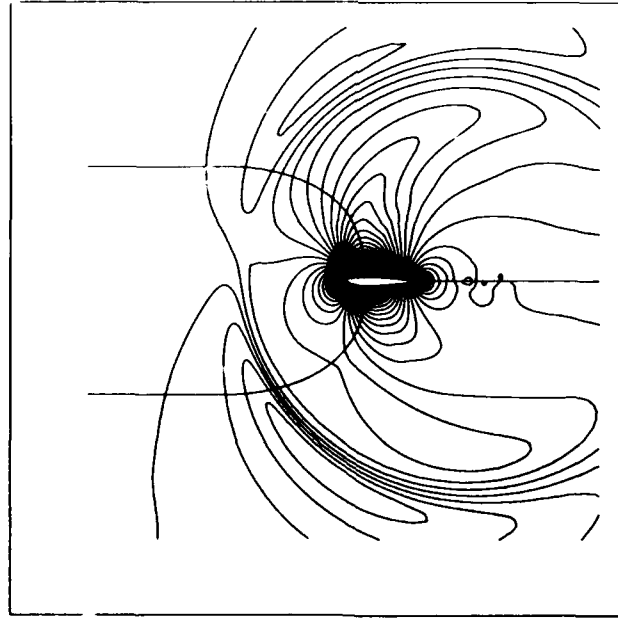
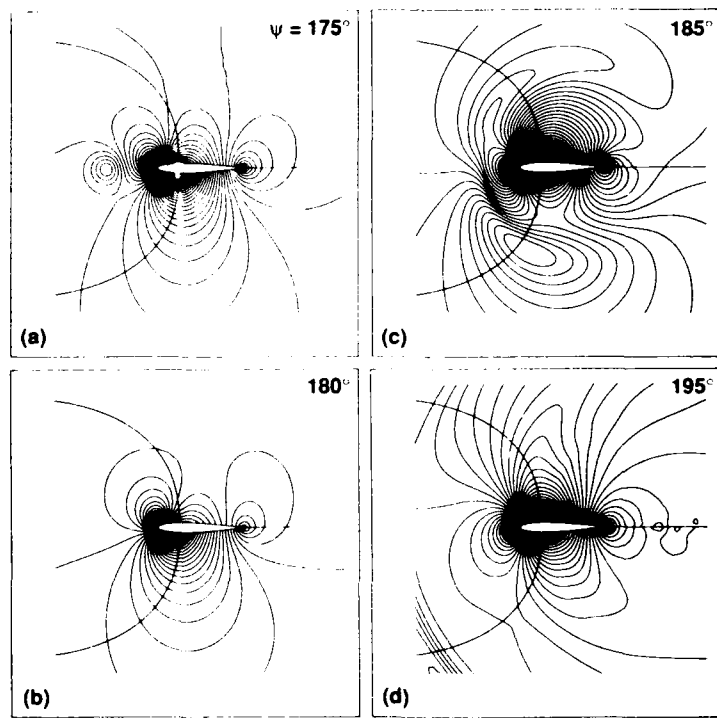


Fig. 44 Pressure contours for a head-on BVI, showing the propagation of an acoustic wave.
 $M_\infty = 0.536$ [73].

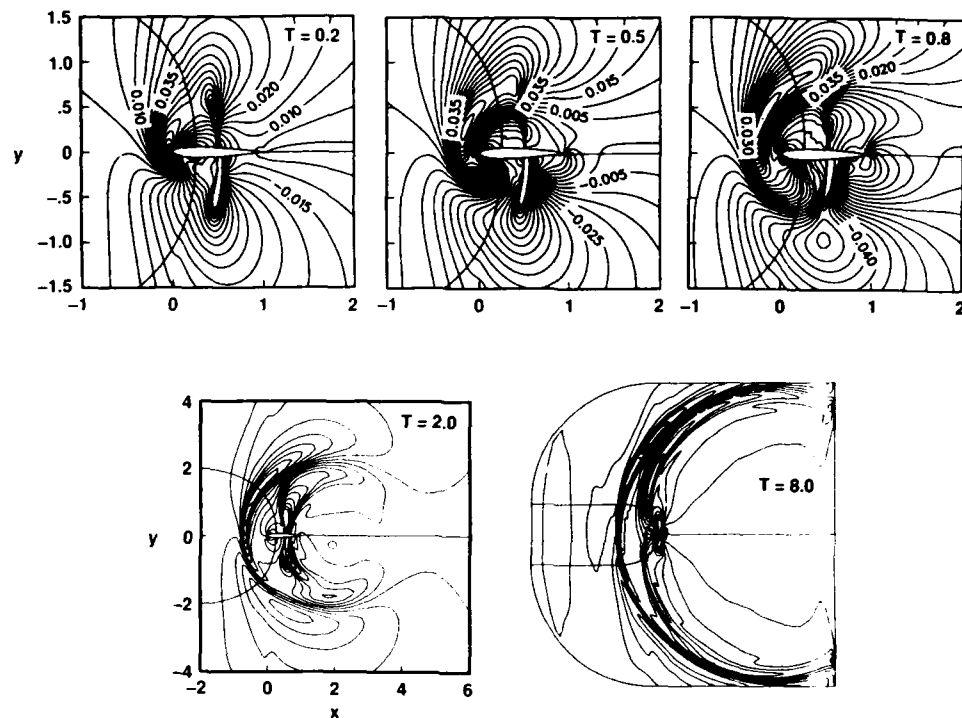


Fig. 45 Pressure contours for a supercritical BVI [74].

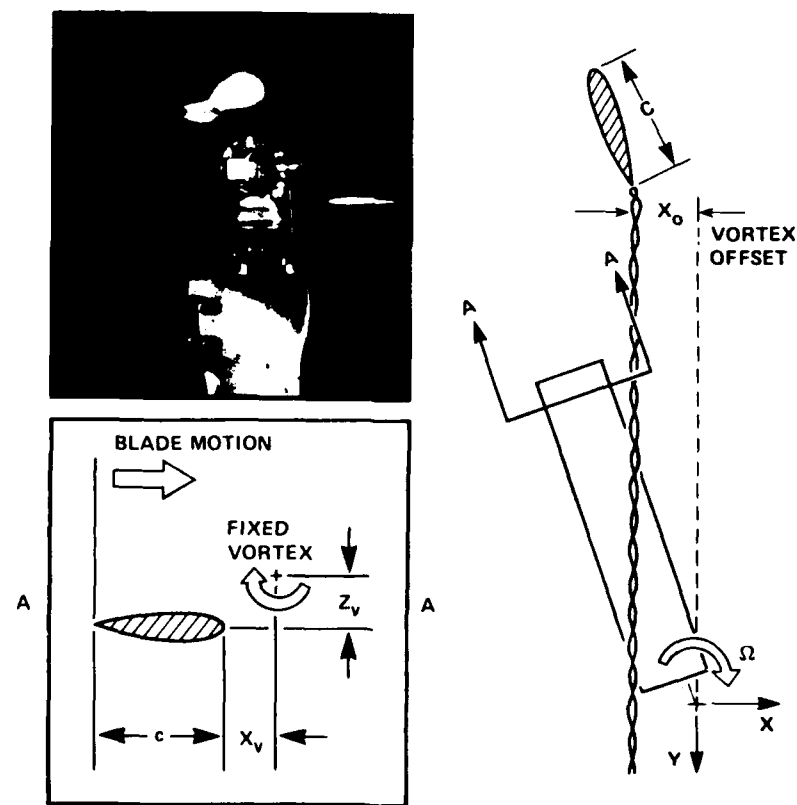


Fig. 46 A rotor BVI test setup for the acquisition of surface pressure data [75, 76].

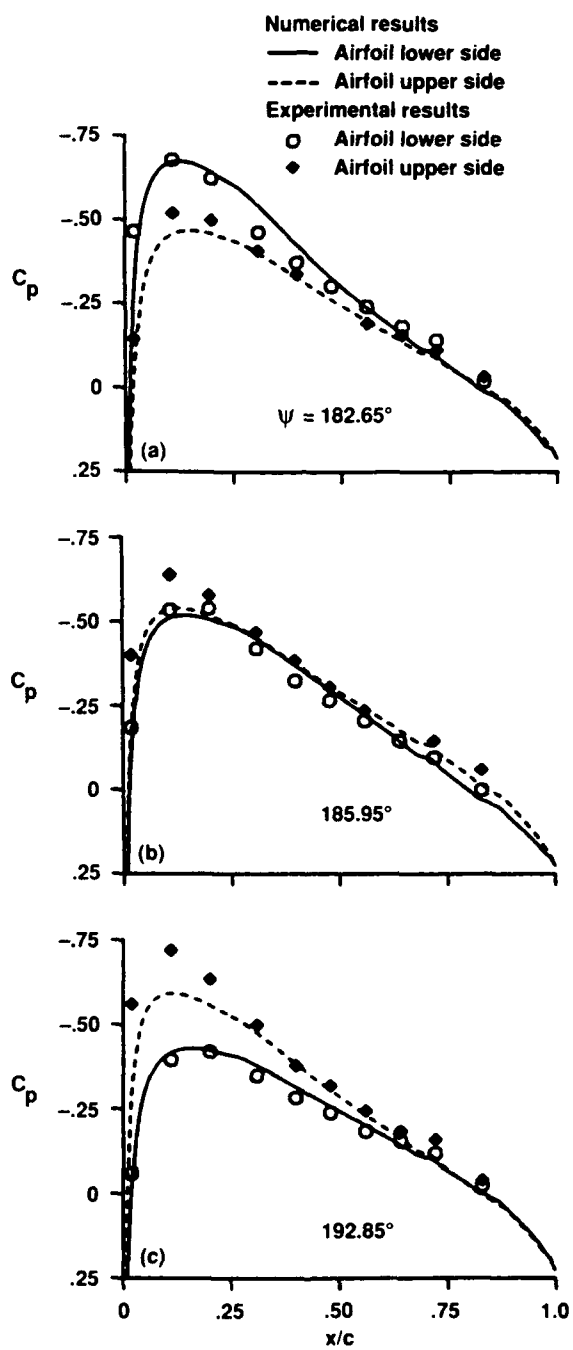


Fig. 47 A comparison of measured BVI surface pressures with computed results from a high-order upwind TNS scheme [73].

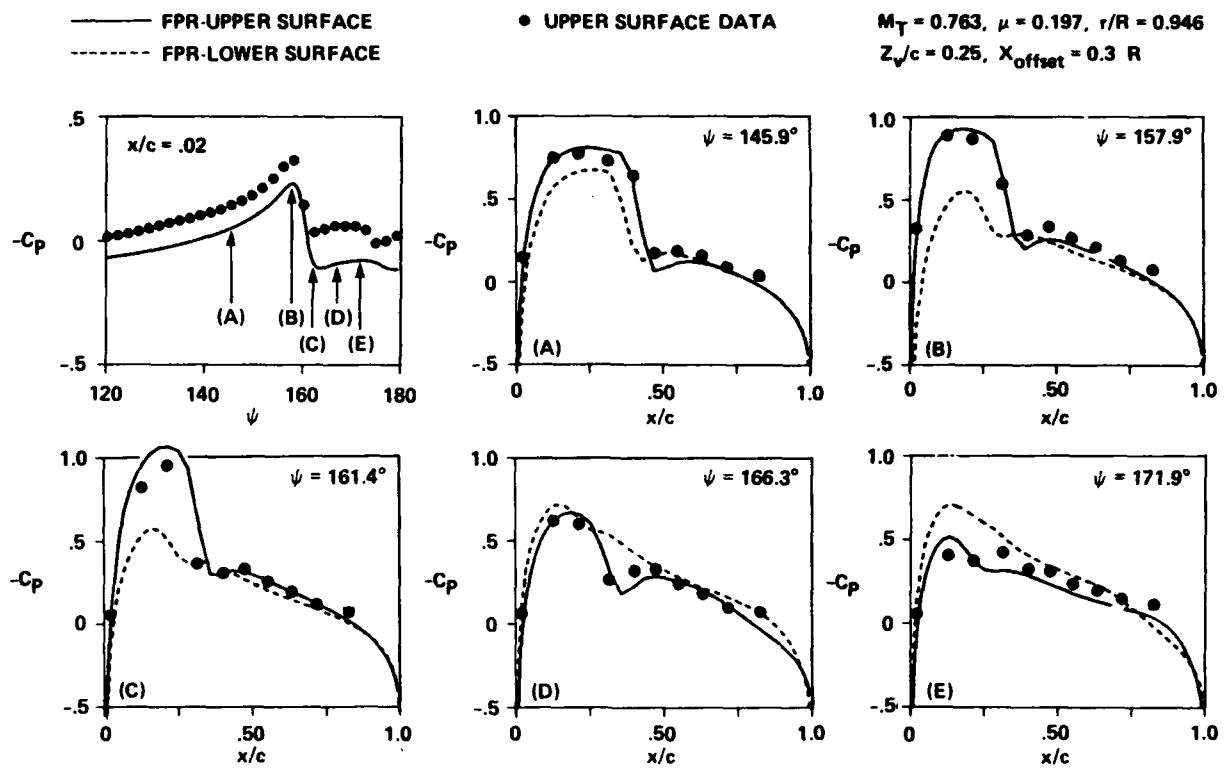


Fig. 48 A comparison of measured BVI surface pressures with 3-D, full-potential results for a supercritical oblique interaction [47].

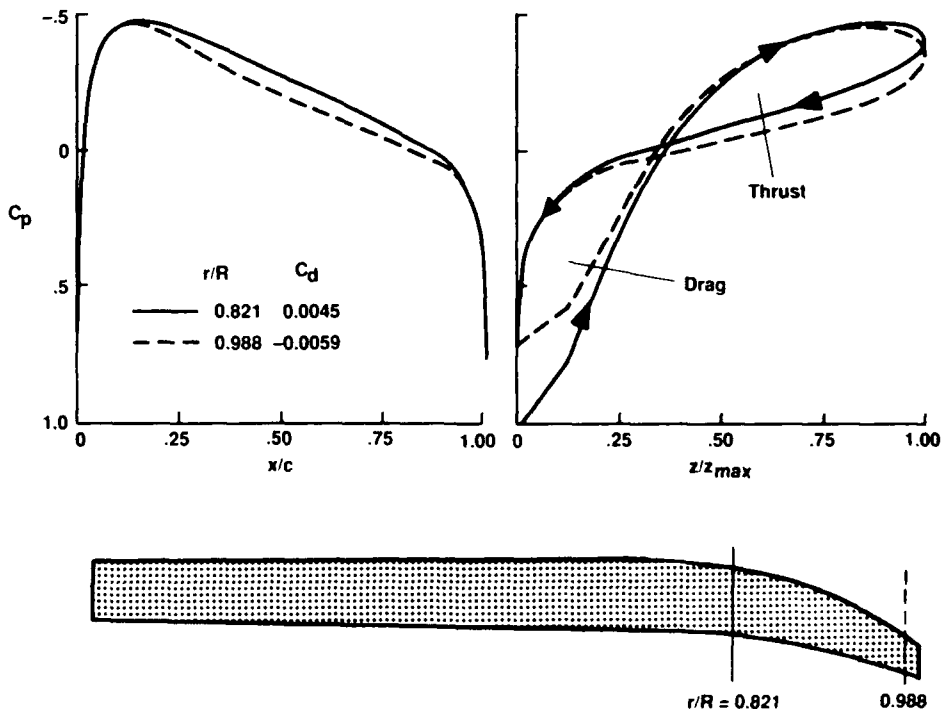


Fig. 49 Computed surface pressures for a swept rotor at two radii, showing the pressure-thickness plot for drag integration [81].

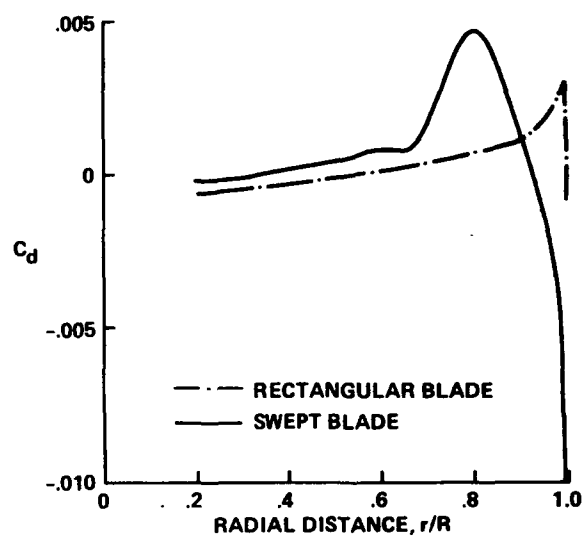


Fig. 50 The computed spanwise drag distribution for swept and rectangular blades [81].

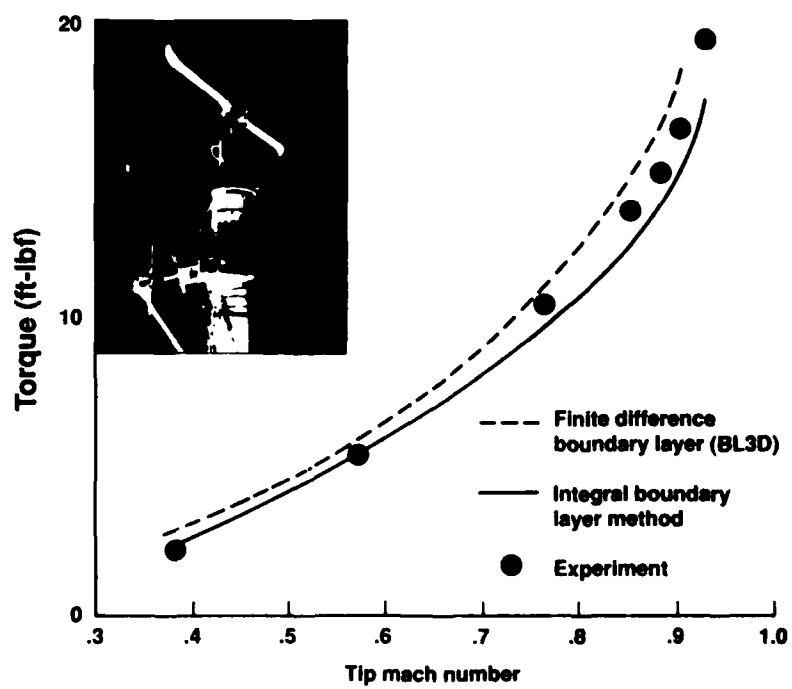


Fig. 51 Computed and measured torque for a swept-tip rotor in hover [81].

REPORT DOCUMENTATION PAGE

Form Approved
OMB No. 0704-0188

Public reporting burden for this collection of information is estimated to average 1 hour per response, including the time for reviewing instructions, searching existing data sources, gathering and maintaining the data needed, and completing and reviewing the collection of information. Send comments regarding this burden estimate or any other aspect of this collection of information, including suggestions for reducing this burden, to Washington Headquarters Services, Directorate for Information Operations and Reports, 1215 Jefferson Davis Highway, Suite 1204, Arlington, VA 22202-4302, and to the Office of Management and Budget, Paperwork Reduction Project (0704-0188), Washington, DC 20503.

1. AGENCY USE ONLY (Leave blank)	2. REPORT DATE	3. REPORT TYPE AND DATES COVERED
	March 1992	Technical Memorandum
4. TITLE AND SUBTITLE		5. FUNDING NUMBERS
The Application of CFD to Rotary Wing Flow Problems		505-61-51
6. AUTHOR(S)		
F. X. Caradonna		
7. PERFORMING ORGANIZATION NAME(S) AND ADDRESS(ES)		8. PERFORMING ORGANIZATION REPORT NUMBER
Ames Research Center, Moffett Field, CA 94035-1000 and Aeroflightdynamics Directorate, U.S. Army Aviation Systems Command, Ames Research Center, Moffett Field, CA 94035-1099		A-90110
9. SPONSORING/MONITORING AGENCY NAME(S) AND ADDRESS(ES)		10. SPONSORING/MONITORING AGENCY REPORT NUMBER
National Aeronautics and Space Administration Washington, D. C. 20546-0001 and U.S. Army Aviation Systems Command, St. Louis, MO 63120-1798		NASA TM-102803 USA AVSCOM TR-92-A-004
11. SUPPLEMENTARY NOTES		
Point of Contact: F. X. Caradonna, Ames Research Center, MS 215-1, Moffett Field, CA 94035-1000 (415) 604-5902 or FTS 464-5902		
This paper was originally prepared as lecture notes for an Agard course, "Aerodynamics of Rotorcraft."		
12a. DISTRIBUTION/AVAILABILITY STATEMENT		12b. DISTRIBUTION CODE
Unclassified-Unlimited Subject Category – 02		
13. ABSTRACT (Maximum 200 words)		
<p>This report is a review intended to serve as source and reference material for the CFD phase of a short course on rotorcraft aerodynamics. The review is mainly oriented toward engineering application methods. Therefore emphasis is placed on potential methods and their various types and uses. However, the application of viscous codes is also discussed. These methods are discussed in the context of the various rotorcraft-specific problems—including wake prediction, blade/vortex interactions, transonic problems, dynamic stall and other separation problems.</p> <p>The exposition includes a discussion of the various flow equations and the physical approximations, which they embody. Basic methods of solving these are presented—especially integral and difference approaches to the various potential equations. The treatment of total rotor/wake problems by hybrid difference/integral schemes are discussed. These include both hover flow and forward flight methods requiring a consideration of trim. Unified schemes, which solve an entire rotor/wake flow on a single grid, are also treated. One of these, a vorticity convecting full-potential approach, is capable of predicting complete hover performance polars. Many comparisons are made with data from flight and model tests, to demonstrate the efficacy of the different flow treatments. Finally, advanced flow topics, requiring full viscous solutions, are shown in order to demonstrate the future possibilities and opportunities for CFD as newer methods mature and become practical.</p>		
14. SUBJECT TERMS		15. NUMBER OF PAGES
Rotorcraft aerodynamics, Wakes, CFD, Transonic flows, Viscous flows		74
16. PRICE CODE		A04
17. SECURITY CLASSIFICATION OF REPORT	18. SECURITY CLASSIFICATION OF THIS PAGE	19. SECURITY CLASSIFICATION OF ABSTRACT
Unclassified	Unclassified	
20. LIMITATION OF ABSTRACT		